

IPSL/ONERA

Annual Report

Climaviation 2024-2025

Agreement number 2021-39 relating to the « Aviation & Climate » project



Financé
par



Financé par
l'Union européenne
NextGenerationEU

The Climaviation team

21/05/2025

Final version

TABLE OF CONTENTS

EXECUTIVE SUMMARY	2
1. AXIS 1: CONTRAILS	5
1.1. WP 1.1: Microphysical mechanisms of particle and ice formation	5
1.2. WP 1.2: Modelling of contrail formation (near field)	8
1.3. WP 1.3: Influence of aircraft configuration	14
1.4. WP 1.4: Evolution of contrails at intermediate scales	18
1.5. WP 1.5: Evolution of contrails on climatic scales	23
1.6. WP 1.6: Detailed study of the radiative impact of contrails	28
2. AXIS 2: ATMOSPHERIC CHEMISTRY	38
2.1. WP 2.1: Effective NO _x emission index	38
2.2. WP 2.2: Improvement of LMDZ-INCA	40
2.3. WP 2.3: Impact of NO _x emissions on ozone and oxidising capacity	41
2.4. WP 2.4: Impact of NO _x emissions on methane	45
3. AXIS 3: IMPACT OF AEROSOLS ON NATURAL CLOUDS.....	46
3.1. WP 3.1: Competition with background aerosols.....	46
3.2. WP 3.2: Aerosol transport from aviation	46
3.3. WP 3.3: Cloud response to aerosol-cloud interactions	49
4. AXIS 4: OBSERVATION.....	53
4.1. WP 4.1: Use of existing data.....	53
4.2. WP 4.3: Model evaluation for contrail prediction.....	58
5. AXIS 5: CLIMATE IMPACTS OF AVIATION	61
5.1. WP 5.1: Traffic and emission scenarios.....	61
5.2. WP 5.2: Integration of all non-CO ₂ effects in the climate model	67
5.3. WP 5.3: Estimation of climate impacts	67
5.4. WP 5.4: Development of OSCAR-Aviation	67
6. AXIS 6: OPTIMISATION STRATEGIES.....	70
6.1. WP 6.1: Assessment and relevance of climate change metrics for aviation	70
6.2. WP 6.2: Climate impact of the fleet estimated by OSCAR	70
6.3. WP 6.3: Quality and relevance of numerical weather prediction for contrail forecasting.....	70
6.4. WP 6.4: Study of optimisation strategies	70
7. REFERENCES	73

EXECUTIVE SUMMARY

The Climaviation research project focuses on the non-CO₂ effects of aviation. The project is a partnership between climate research, represented by the Institut Pierre Simon Laplace (IPSL) and its stakeholders, and especially Sorbonne Université and the CNRS, and aeronautical research, represented by the French Aerospace Lab ONERA. The project is funded by the Direction Générale de l'Aviation Civile (DGAC) for the period 2021-2026. It will enter its last year in June 2025.

The project is structured around 6 axes of research, and has three main objectives:

- To reduce uncertainties in the radiative forcing exerted by contrails and contrail cirrus (Axis 1), aviation NO_x emissions (Axis 2) and the interactions between aviation aerosols and clouds (Axis 3). Improved process understanding is facilitated by modelling at different scales, combined with the exploitation of existing observations and the acquisition of new observations (Axis 4).
- To quantify the radiative forcing of the current fleet, design scenarios of future aircraft traffic and technological changes, and quantify the radiative forcing associated with those scenarios (Axis 5).
- To evaluate strategies to minimise the total climate impact of aviation including by looking for compromises between CO₂ and non-CO₂ effects, for both individual flights and a fleet (Axis 6).

This report summarises activities that took place from April 2024 to March 2025. Most work packages have been active in the fourth year of the project, with some of the main objectives of Climaviation being fulfilled, as summarised below. Climaviation has published 19 peer-reviewed papers so far. Thirty-six individual researchers contributed to this Annual Report, evenly split between IPSL and ONERA. Contributions come from permanent researchers at IPSL and ONERA, and postdoctoral researchers, research engineers, PhD students, and interns working specifically on the project.

Axis 1 Contrails

Climaviation research on contrails seeks to test the hypothesis that the conditions of formation and early evolution of contrails influence their climate impact. To do so, a hierarchy of models is being built, with increasing seamlessness, to simulate the formation and evolution of contrails from particle nucleation in the engine exhaust plumes to climate scales.

Over the past year, the ability of ONERA to simulate contrails in a consistent way has improved, with simulations of the near field providing improved initial conditions to intermediate field models which have simulated up to 8 minutes of contrail lifetime. At IPSL, a parametrisation of ice supersaturated regions and linear persistent contrails is now available for the first time in the LMDZ climate model, with the ability to use, in due course, a contrail initialisation informed by ONERA's work on the intermediate field. The LMDZ parametrisation will soon provide new estimates of contrail cirrus effective radiative forcing and efficacy.

In parallel, ONERA's radiative transfer models have been improved and tested to better quantify the uncertainty due to radiation calculations, which is substantial. Work at IPSL suggests that three-dimensional radiative effects, caused by the interaction of radiation with the sides of contrails, remain important even after integration over flight trajectories. The dependence of those 3D effects on contrail properties, including orientation with respect to the Sun, is complex but could perhaps be parametrised.

Axis 2 Atmospheric Chemistry

Activities focused on completing the move to a new version of the LMDZ-INCA model, with a much finer vertical resolution and improved representation of key processes in ozone and methane chemistry and aerosol physics, including NO_x emissions by lightning and a new assessment of the importance of wet scavenging for

gaseous and aerosol species. The new model version is currently being used to quantify the level of non-linearity of the ozone response to aviation NO_x emissions.

In parallel, work has started on accounting for chemistry in the aircraft plume before dilution in a climate model grid-cell, using the pycontrails implementation of CoCiP to calculate the temporal evolution of the contrail cross section of actual flights.

Finally, the analysis of the ACACIA multi-model ensemble has been finalised with calculations of the ozone, methane, and aerosol radiative forcing for the participating models.

Axis 3 Impact of aerosols on natural clouds

Previous work on the interaction between aviation aerosols and cirrus clouds relied on the assumption that the response of cirrus ice water path to ice crystal number perturbations can be separated from the preceding response of ice crystal number to aerosol perturbations. However, it was found that the representation of aerosols in the MONC large eddy simulation model was not good enough to test this assumption. Over the past year, model developments have improved the representation of the competition between aviation soot and ambient aerosols. The vertical and horizontal resolution of the model have also been increased.

Comparison to cases published in the literature show encouraging indications that the improved model can simulate the competition between homogeneous and heterogeneous nucleation that arises from the addition of aviation soot. Once that is confirmed, aerosol perturbations will be applied to different cirrus clouds to quantify the sensitivity of their ice water path to those perturbations.

In parallel, work on the dependence of long-range transport of aviation aerosols on the representation of wet scavenging in the LMDZ climate model has made great progress. Technical developments are complete, and results suggest that, surprisingly, the choice of scavenging parametrisation has a strong impact on aviation perturbations in the upper troposphere/lower stratosphere, despite precipitations being rare in this region. Different scavenging parametrisations affect the size of the impact of cruise emissions on surface air quality, which is more uncertain than previously thought.

Axis 4 Observations

Over the past year, there has been promising progress in our capacity to evaluate contrail formation and evolution models with ground-based and satellite observations.

The morphological algorithm developed over the past years to detect contrails in images of the ground-based hemispheric camera has been applied to the image database over the period 2019-present. The time series of daily contrail counts should provide statistics of contrail outbreaks. Deep learning algorithms are now being trained with encouraging results to go beyond the capabilities of the morphological algorithm.

Three good contrail case studies have been identified at the SIRTa observatory. The IPRAL lidar, the ground-based hemispheric camera, Trappes radiosonde measurements, and pyranometer measurements are used to document the atmospheric conditions in which the observed contrails formed, to estimate their optical depth, and to quantify their effect on short and longwave radiation.

In parallel, comparisons between the contrail energy forcing simulated by the Contrail Cirrus Prediction model (CoCiP) and estimates based on geostationary satellite retrievals have been made on two contrail outbreaks. There are instances of good match between the model- and satellite-based estimates, but also interesting differences that suggest that both CoCiP and the satellite-based analysis have limitations that can be better identified thanks to such comparison exercises.

Axes 5 and 6 Climate impacts of aviation and optimization strategies

A new four-dimensional inventory of aviation emissions is being developed by applying the ONERA's ATMLab onto the Flightradar24 flight trajectory database. In parallel, the methodology for producing scenarios of future emissions is being refined.

The development of a first version of OSCAR Aviation, a reduced-complexity climate model with improved representation of aviation emissions, is almost complete. Applying the model on various SSP scenarios of future aviation emissions suggests that the increase in surface temperatures attributable to aviation could be 2.4 times larger in 2050 than it is now. Applying the model on a simplified and very optimistic contrail avoidance scenario, where contrail avoidance successfully reduces contrail effective radiative forcing by up to 50% without additional fuel consumption, suggests that contrail evidence cannot revert the increasing trend in surface temperature warming from aviation, but could offset some of the impact of the market growth in 2100.

Finally, a new flight trajectory optimiser called FlightOptima has been developed. It minimises fuel costs and climate impact based on weather conditions and estimates of contrail energy forcing from CoCiP. Using this tool with different CO₂-equivalence metrics suggests that although the detail of the optimal route depends on the choice of metric, all metrics lead to a strong potential for decreasing the climate impact of flights with relatively small increases in fuel consumption.

1. AXIS 1: CONTRAILS

The objective of this axis of research is to study the formation, ageing and characteristics of contrails, and their possible evolution into induced cirrus clouds. For each of these phases, the aims are to improve the understanding and modelling of the various mechanisms involved in the evolution of the contrail and influencing its radiative properties on the climate scale.

1.1. WP 1.1: Microphysical mechanisms of particle and ice formation

Work package 1.1 is devoted to the analysis of the mechanisms of formation of the ice crystals that form contrails. The objective is in particular to identify the respective influence of the various mechanisms which can intervene depending on the chemical composition of the fuels used.

Contributors: Nicolas Bonne, Etienne Terrenoire, and Ismael Ortega (ONERA)

Last year evaporation rates have been calculated for different kind of particles which may form behind a hydrogen (H₂) engine. The most promising scenario involved particles formed by nitric acid and negatively charged nitric oxide. This year, these evaporation rates have been used to derive nucleation rates using the ACDC model (Atmospheric Cluster Dynamics Code; Olenius, 2021) for different plume composition. ACDC is a kinetic model that simulates the dynamics of molecular cluster and nanoparticle populations by generating and solving the cluster birth-death equations for given ambient conditions, yielding the time evolution of cluster concentrations and formation. The initial aerosol particles (1-2 nm in diameter) are characterized by steady-state formation rate.

The composition of an Aircraft plume depends on the type of fuel burned. Four different types of fuels are tested for this task: Classical Jet A-1 kerosene, a 50/50 blend between Jet A-1 and a biofuel, a 100 % biofuel and hydrogen (H₂) (Table 1-1).

Table 1-1 Input description of the four test cases

Fuel type	Molecule/Charge ⁽¹⁾	Particle number	Particle diameter (nm)
100% Jet A-1	H ₂ SO ₄ /bisulfate and HNO ₃ /nitrate	C in plume ⁽³⁾	54
50% Jet A-1/50% biofuel	H ₂ SO ₄ ² /bisulfate and HNO ₃ /nitrate ⁽²⁾	C in plume ⁽³⁾	54
100% biofuel	HNO ₃ /nitrate	C in plume ⁽³⁾	43.2
Hydrogen (H ₂)	HNO ₃ /nitrate	600 ⁽⁴⁾	30 ⁽⁴⁾

¹ Plume's chemical composition is a 50/50 mixing between gas and the corresponding ion

² –50 % compared to the Jet A-1 case

³ Concentration of nvPM as modelled in the plume (EIsoot is 1×10^{15})

⁴ background soot only (as mentioned in Bier et al., 2023)

⁵ |C| mean particle number concentration

The gas concentration for H_2SO_4 , HNO_3 and the number of nvPM as well as the temperature are based on the means of different CFD simulations of engine plumes using the CHARME solver from CEDRE (Refloch et al., 2011) coupled to the Karcher et al. (2015) atmospheric chemistry scheme. Hence, the plume chemical evolution is modelled with high fidelity with spatial resolution of a few centimeters and a time step of a few milliseconds. For 100% Jet A-1 and 50% Jet A-1/50% biofuel, the contribution from both H_2SO_4 and HNO_3 species have been calculated while for the 100% biofuel and H_2 cases only NO_x emissions are considered therefore only the HNO_3 contribution is quantified.

Figure 1-1 shows the influence of the temperature of the plume on the nucleation rate J for the four studied cases. For all cases, the nucleation process is only significant at 308 K and is between 10^5 and 10^6 $\#/\text{cm}^3/\text{s}$. A small rate is also modelled for the 50/50 biofuel case at 258 K (1.3×10^1 $\#/\text{cm}^3/\text{s}$).

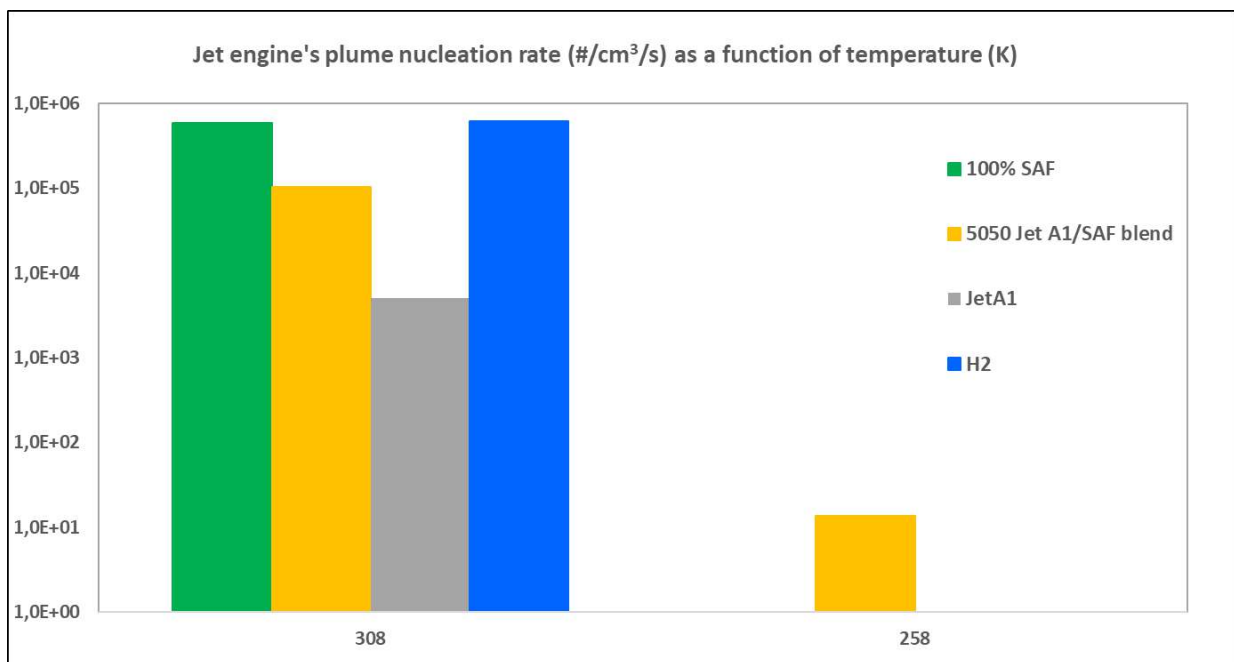


Figure 1-1: Nucleation rate in the jet engine plume, in $\#/\text{cm}^3/\text{s}$, as a function of temperature (in K) for four different fuel compositions.

To explain the nucleation rate tendency, Figure 1-2 shows the evolution of the concentration of the two main precursors H_2SO_4 and HNO_3 for the four cases. Plume concentration for both species peaks just after the engine exit before decreasing strongly due to nucleation processes that consume the gas phase of the two species. For HNO_3 , the concentration decreases strongly just after the emission to reach a constant value around 245 K up to 224 K. For H_2SO_4 , a strong decrease is also observed after the engine exit but the rate of decrease stays rather constant until 228 K for the Jet A-1 case and until the jet temperature reaches the ambient temperature in the 50/50 biofuel case. The evolution of the concentrations of the precursors seems to indicate that the nucleation process is quasi-instantaneous and takes place just after the engine exit for the HNO_3 precursor. For H_2SO_4 , the nucleation takes place over a longer period although after 258 K, the nucleation rate can be considered as negligible to contribute significantly to the formation of ice particle in the plume.

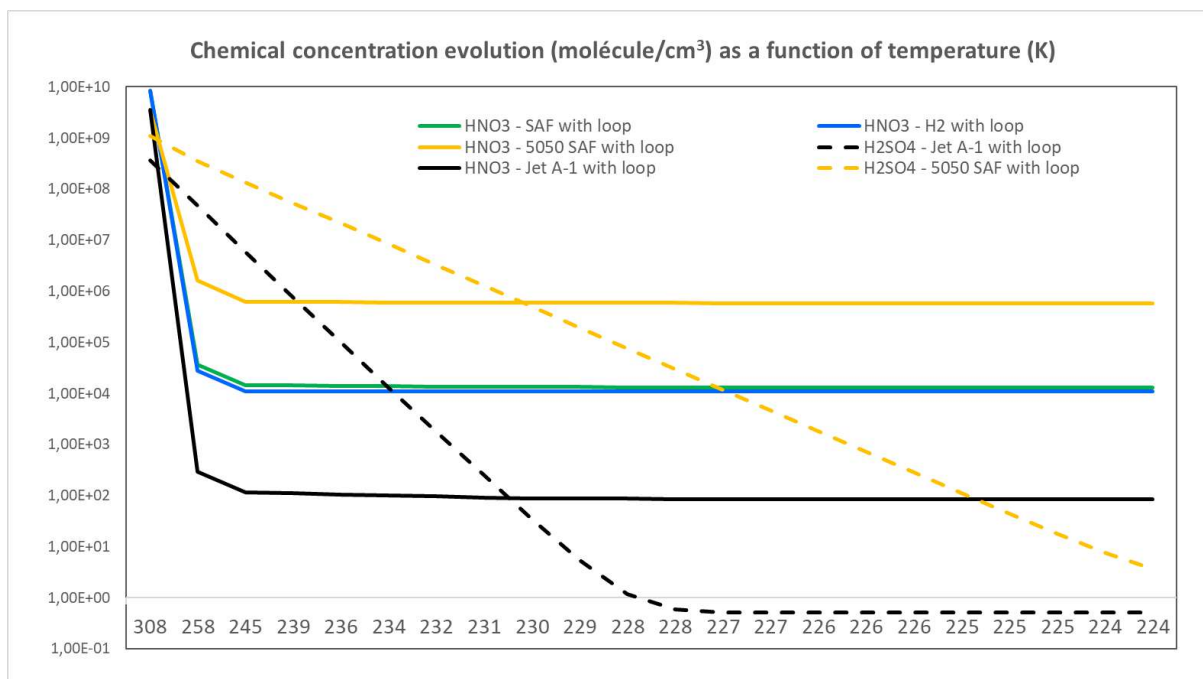


Figure 1-2: Evolution of chemical concentrations of HNO₃ and H₂SO₄ in the jet engine plume, in #/cm³/s, as a function of temperature (in K) for four different fuel compositions.

Then a 1D code has been developed to simulate the contrail formation. In this code, the small cluster appears according to the nucleation rate. Water can condense around these particles using k-Köhler theory assuming a 0.5 coefficient for nitric acid. The particles can coagulate and freeze. A sensitivity analysis on NO_x emissions, at ambient temperature and ambient relative humidity, has been made. Figure 1-3 shows a sensitivity analysis on nitric acid mass fraction at engine exit. The results are compared to the number of ambient particles trapped into the jet for different ambient particles concentrations.

At first liquid nitric acid particles form. Then the number of liquid particles by metre of flight increase. When the plume is cold enough, the water that has condensed on the nitric acid cluster can freeze and these liquid particles are replaced by ice crystals. At the end only ice crystals remain. One can see that the number of ice crystals strongly depends on the initial nitric acid mass fraction.

Another way to form contrail without soot would be condensation of water around ambient particles which have been trapped in the plume. To evaluate the maximum ice crystal number that may be reached in this scenario, we vary the number of ambient particles trapped in the plume. The results show that the nitric acid scenario dominates contrail formation compared to the scenario based on ambient particles. A sensitivity analysis on the fraction of charged/neutral molecules will be made next year to evaluate if this scenario remains relevant when fewer charged molecules are formed.

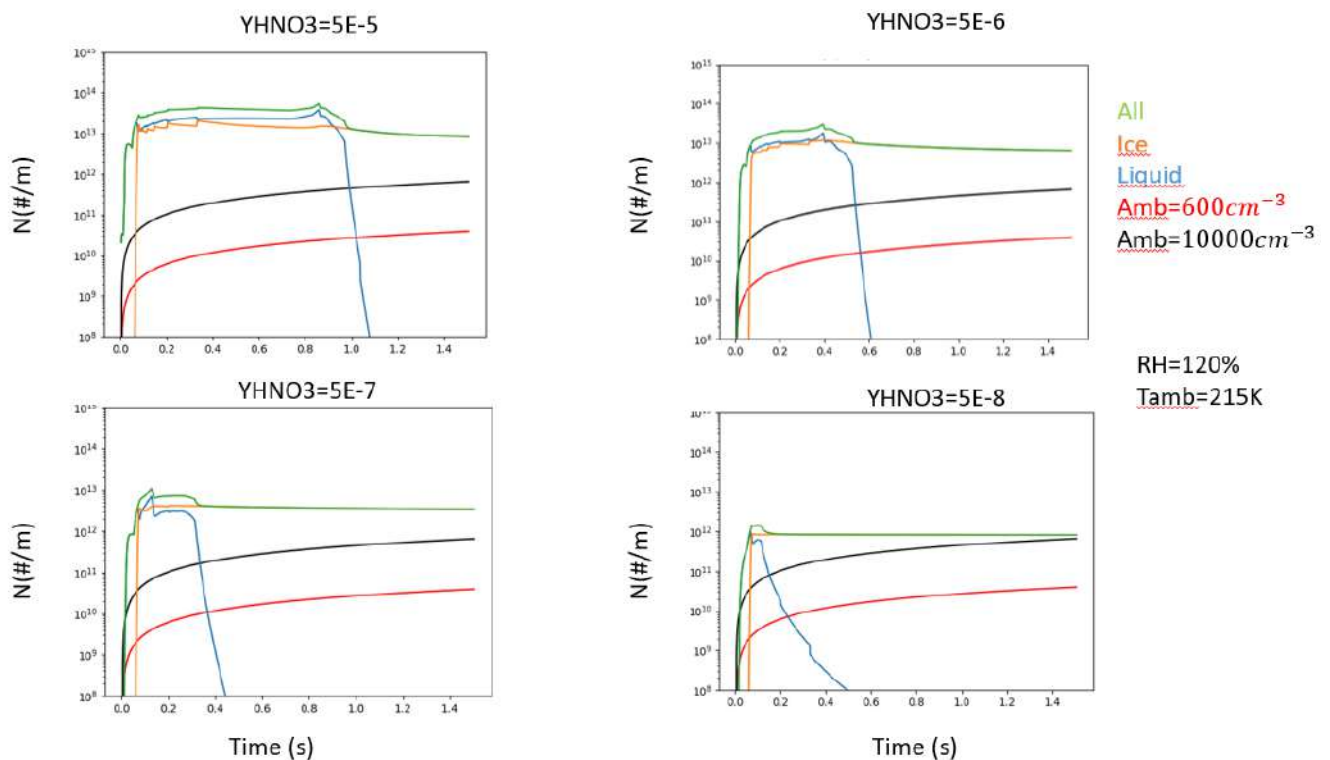


Figure 1-3: Sensitivity analysis of hydrogen contrail formation on nitric acid mass fraction (Y_{HNO_3} , dimensionless) at engine exit. The y-axis shows the number of particles per flown metre, for ice crystals (in orange), liquid droplets (blue), and ambient aerosols entrained in the jet as it dilutes.

1.2. WP 1.2: Modelling of contrail formation (near field)

The objective of work package 1.2 is to improve the modelling integrated into ONERA's CEDRE code and to calibrate the code and the numerical approaches (turbulence models, meshing) used to simulate the mixing of the engine jet and its interaction with the aircraft wake on experimental results. A specific wind tunnel test has been performed to acquire experimental data.

1.2.1. Jet/vortex interaction experiments

Contributors: Vincent Brion, Marie Couliou, Léo Clauss (ONERA) and several others at ONERA and Laboratoire de Mécanique des Fluides de Lille

In 2024, an experiment dedicated to the investigation of the mixing of the jet exhaust by the wake of an aircraft was carried out at the boundary layer wind tunnel in LMFL Centrale Lille laboratory. The setup comprised a generic wing and jet model parameterized by the lateral position of the jets about the span, considering a symmetrical configuration corresponding to straight, level flight, and keeping flow velocity, lift and thrust constant. The objectives of the experiment are to evaluate the mixing of the jet by the wing wake depending on the jet position b_j , due to the jet/wake interaction and to generate a database for the validation of Computational Fluid Dynamics (CFD) solvers. A picture of the test setup in the wind tunnel is shown in Figure 1-4 (left). The wind tunnel features a rectangular test section of width 2 m, height 1.5 m and length 20 m, and generates a flow of 9 m/s on the model. The wing of span $b = 0.5$ m and chord $c = 0.125$ m is adjusted with an angle of attack of 9 degrees and the jets are fed by compressed air whose mass flow rate can be controlled. Angle of attack and jet flow are tuned to mimic the ratio of lift to thrust forces typical of cruising flight. The Reynolds number (chord based) of the experiment is about 80 000. The test section offers an

exploration distance of the wake of the model aircraft of 10 m, which represents 20 wingspans of exploration length, and corresponds to about 4 seconds of the wake developing time of a cruising aircraft of span 50 m. The wake is characterized by Particle Image Velocimetry (PIV) at several transverse planes downstream of the model. This provides the three components of the velocity field in two-dimensional planes perpendicular to the upstream flow. In addition, images of transverse cuts of the jet exhausts are taken by the same PIV cameras when only the jets are seeded with olive oils droplets. This technique allows to track the jet exhaust along the axial direction. The PIV velocity fields together with the jet exhaust transverse maps make up the experimental database which is now available for the validation of the numerical simulations. These will be accomplished with the ONERA CEDRE solver in task T1.2.3 (see section 1.2.2).

The main results obtained from the analysis of the experimental database are now briefly described. First the validity of the experimental setup has been appraised by checking that the lift generated by the wing is unchanged when the jets are localized differently. The evolution of the ratio of the lift coefficient for a given jet position over the lift coefficient for a wing without jet ($C_L/C_{L,no\ jet}$) is shown in Figure 1-4 (right) showing that the lift is close to the one of the no jet configuration whatever the jet position over the span (b_j/b).

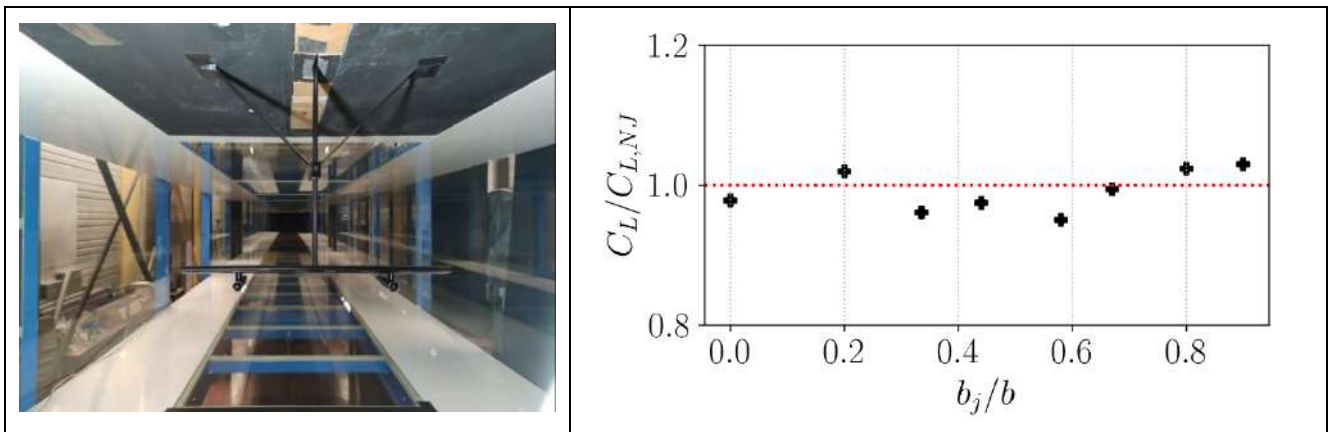


Figure 1-4: Experiment. (left) Test setup of the jet / vortex interaction study in the boundary layer wind tunnel at LMFL Lille Laboratory. (right) Evolution of the lift of the wing as a function of the lateral position of the jets

Next, Figure 1-5 (left) shows the axial velocity case when the jets are 80 % of wingspan apart (i.e $b_j/b = 0.8$) at the several downstream PIV measurement planes. The figure highlights the main structures of the wake flow, namely the two-dimensional wake of the wing shed at the trailing edge, the tip vortex that rolls up as the flow progresses downstream, the wake of the mast, and the wake at the junction between the mast and the wing, which features a separated flow area. Additionally, the jet flow stands out from the rest by exhibiting a positive axial velocity relative to the freestream. Figure 1-5 (left) interestingly shows that the roll-up of the wake fully completes within the exploration length available in the wind tunnel (note that the 20 m of the entire test section could not be used because of nascent interferences of the wake with the bottom wall beyond 10 m). This leaves the tip vortex as the only flow structure present in the last measurement planes. As can be observed, during this evolution, the tip vortex has moved down by almost a chord length and localises slightly inward about the wing tip.

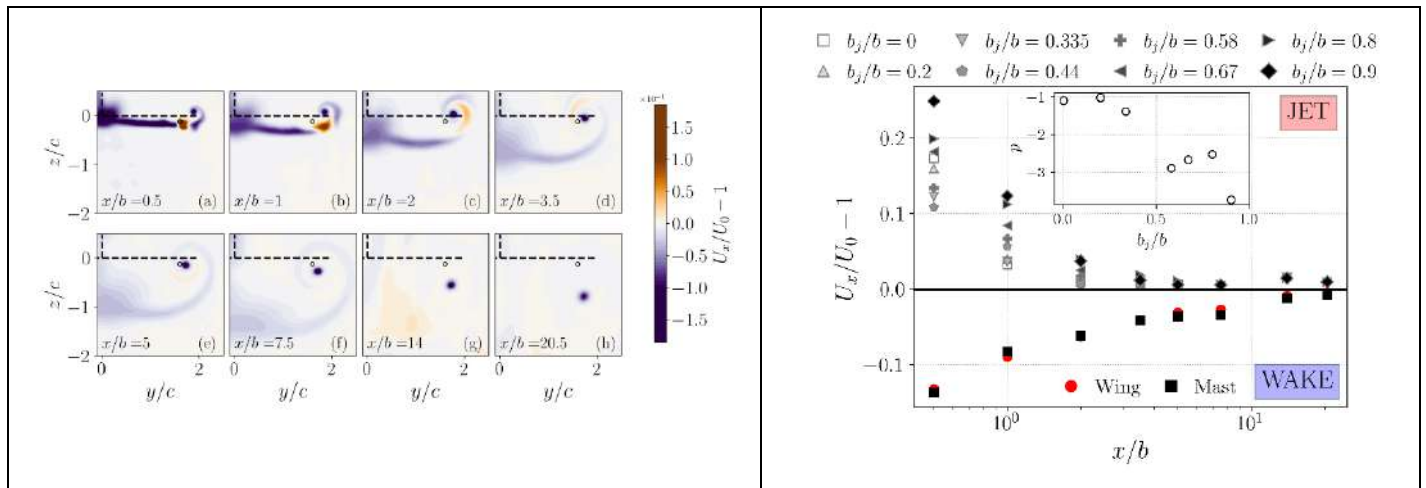


Figure 1-5: Analysis of the PIV data. (left) Plot of the axial flow velocity in the various transverse planes for $b_j/b = 0.8$. (right) Axial evolution of quantities representing the jet and wake, for the different jet configurations

Figure 1-5 (right) quantifies the axial evolution of the wake and jet axial velocities. It shows that for all jet spacings the wake and jet disappear within 20 wingspans. The decrease of the jet axial velocity is compared to an exponential law of factor p . The inset in Figure 1-5 (right) shows the evolution of p as a function of the jet spacing. It is found that when the jet is far from the tip, p is 1, which is expected for an isolated turbulent jet. As the jets are placed closer to the wing tip, hence to the tip vortex, p takes larger absolute values, indicating a more rapid velocity decrease. Thus, this shows that the proximity of the tip vortex mixes the jet more rapidly compared to the isolated jet case. Figure 1-5 (right) shows that the maximum jet velocity at the first measurement plane varies with the jet spacing. While not expected the reason for this is currently analysed. Eventually Figure 1-6 shows images of the jet exhaust at several downstream transverse planes for a selection of jet spacings. The jets are seeded with olive oil which plays the role of a passive tracer. The grayscale level is proportional to the concentration in passive tracer. The images shown in Figure 1-6 are post-processed using a threshold to exclude the noise in the images and isolate the jet exhaust. The rolling-up of the jet by the tip vortex can be visualized, and two distinct dynamics are revealed. When the jet is far enough from the tip, the jet undergoes a spiral about the tip vortex, while when it is close enough, the spiral finally gets into the vortex core. This observation is limited by the exploration length available. It may happen that the jet attains the vortex core at larger downstream distances than those reachable in the present study. Overall, the experimental study indicates a sensitivity of the jet plume spatial distribution on dilution on the jet position in span.

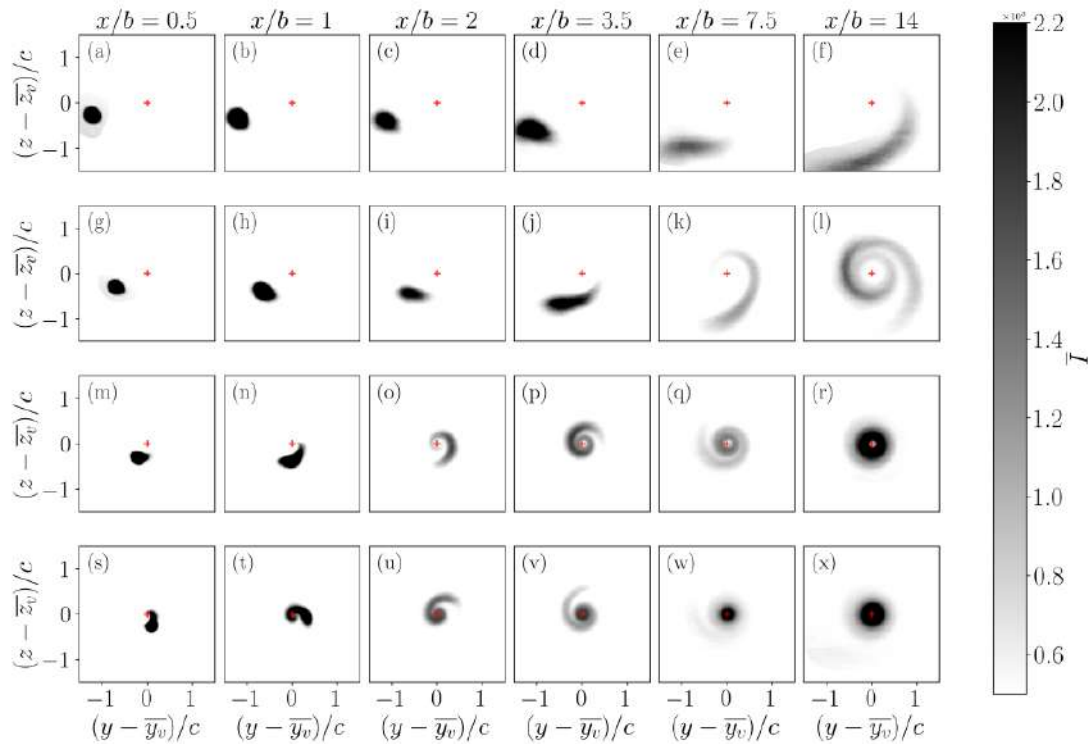


Figure 1-6: Visualization of the evolution of the jet exhaust in selected downstream planes and jet spacings. The plots show the intensity of the laser light scattered by the jet exhaust seeded with olive oil droplets.

1.2.2. Evaluation of RANS turbulence models in the CEDRE software with experimental data

Contributor: Fabien Gand (ONERA)

The objective of this task is to use the experimental database acquired in T1.2.1 to evaluate the RANS turbulence modelling and simulation methodology which is used in other tasks of WP1 to predict contrails formations downstream of full aircraft configurations with the CEDRE software.

As a first step, an unstructured mesh was generated manually for the experimental configuration with the jet/wingtip location $b_j/b = 0.8$ as illustrated in Figure 1-7. This mesh contains approximately 50×10^6 cells. The complete geometry of the model used for the wind tunnel tests in T1.2.2 is taken into account, including the nozzle pylon and the wing strut.

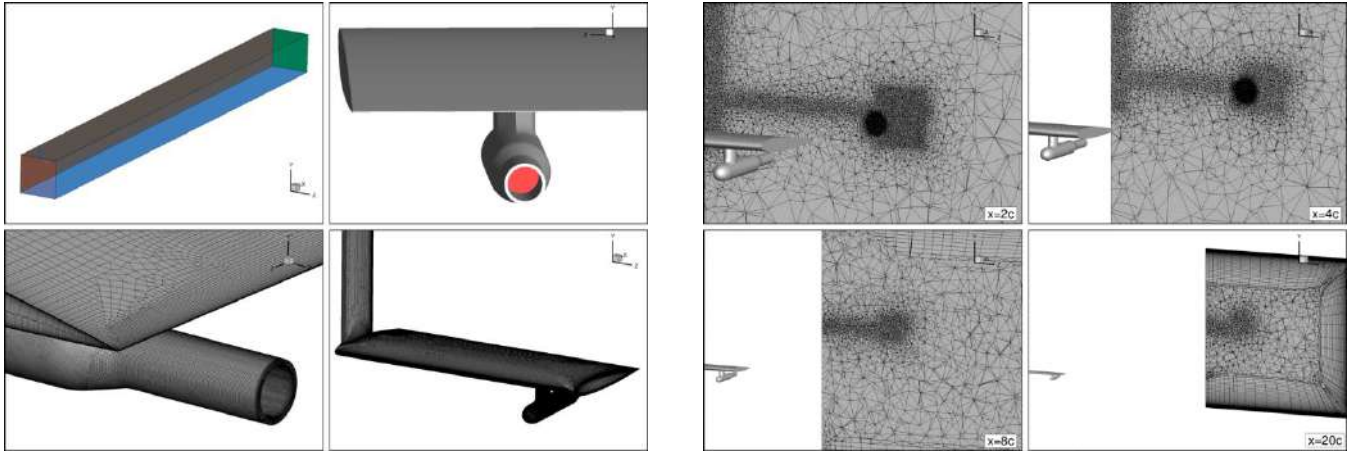


Figure 1-7: Computational domain and mesh visualizations

The experimental flow conditions simulated correspond to a freestream velocity of $U_\infty = 9 \text{ m/s}$ ($Re_c = 8 \times 10^4$) and the jet exit velocity is $\sim 19 \text{ m/s}$. Three standard turbulence models were considered in the first stage of this task: Spalart-Allmaras, Spalart-Allmaras with QCR2000 correction, and $k-\omega$ Menter SST.

As a preliminary verification of the simulation setup, Figure 1-8 presents the simulated jet exit velocity profiles compared with experimental measurements. This validates the boundary conditions used in the simulations.

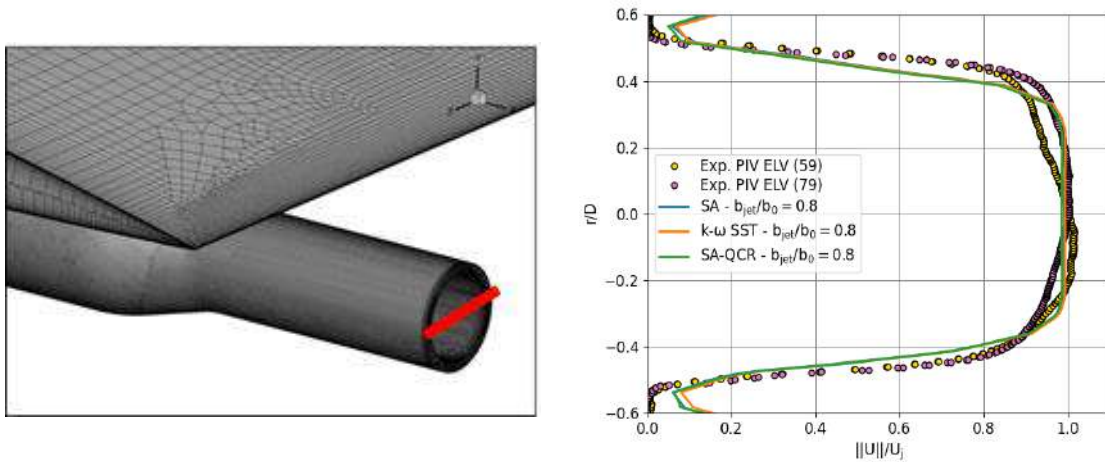


Figure 1-8: Velocity profiles at the jet nozzle exit

The simulated flow along the wing is depicted in Figure 1-9 for the CEDRE simulation with the SA-QCR2000 model. The other models considered provided a similar solution. Two separated areas can be observed: the corner separation, which was also observed in the experimental data, and a separation in the central part of the wing, which is not consistent with wind-tunnel data and is therefore considered to be an anomaly of the simulation. The extent of this separation in the central part of the wing is further illustrated in the right-hand side of Figure 1-9.

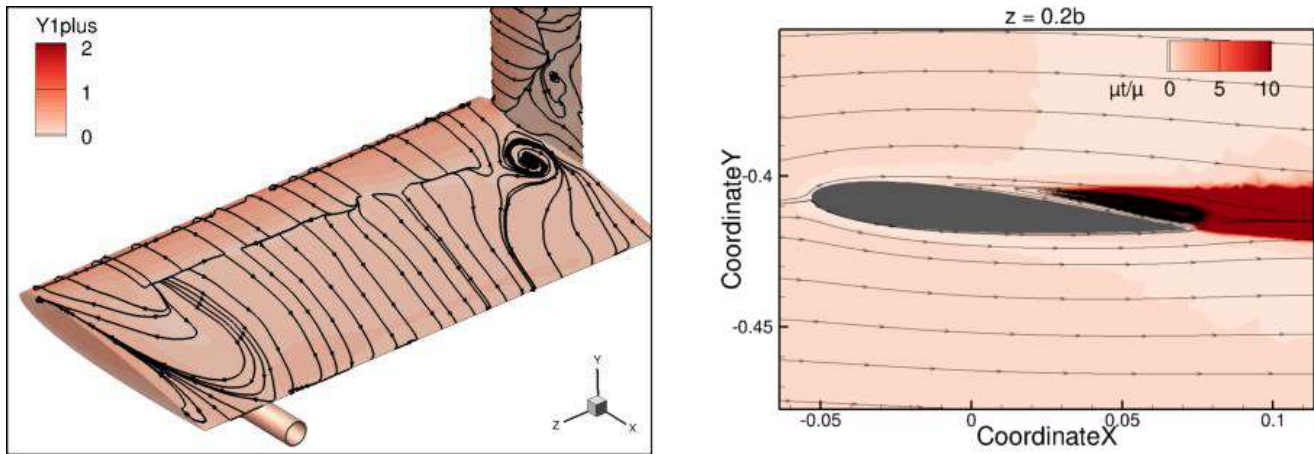


Figure 1-9: Visualisation of skin friction lines (left) and streamtraces in the transverse plane $z = 0.2b$ (right). CEDRE SA-QCR2000 simulation

To investigate the origin of the unexpected flow separation on the central part of the wing, the same simulation with the same mesh and same turbulence model was carried out with the elsA CFD software (also developed at ONERA), which is commonly used for aerodynamic design. The results depicted in Figure 1-10 appear more consistent with the experimental observations regarding the flow over the wing. This result shows that the flow separation on the wing obtained with the CEDRE simulations may be attributed to a bad choice of numerical parameters and will be corrected in the forthcoming weeks.

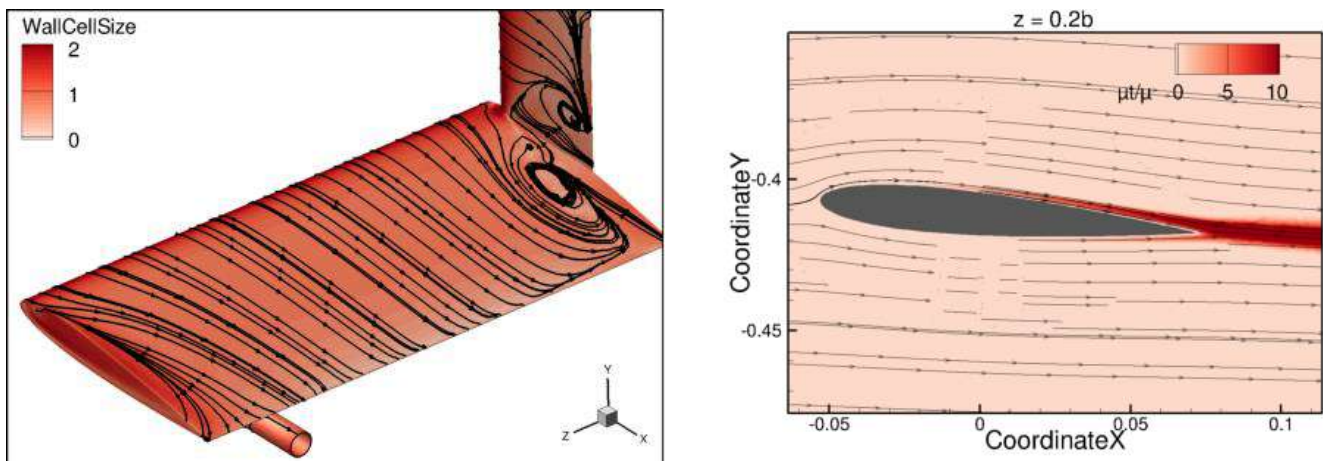


Figure 1-10. Visualization of skin friction lines (left) and streamtraces in the transverse plane $z = 0.2b$ (right). elsA SA-QCR2000 simulation

Finally, some preliminary comparisons of velocity contours in the wake close to the wing are presented in Figure 1-11. These visualizations confirm that the flow separation in the central part of the wing on the CEDRE simulation is not expected, and the fair agreement between the elsA simulation and the experimental data indicates that the issue with the CEDRE simulation cannot be attributed to the mesh nor to the turbulence model.

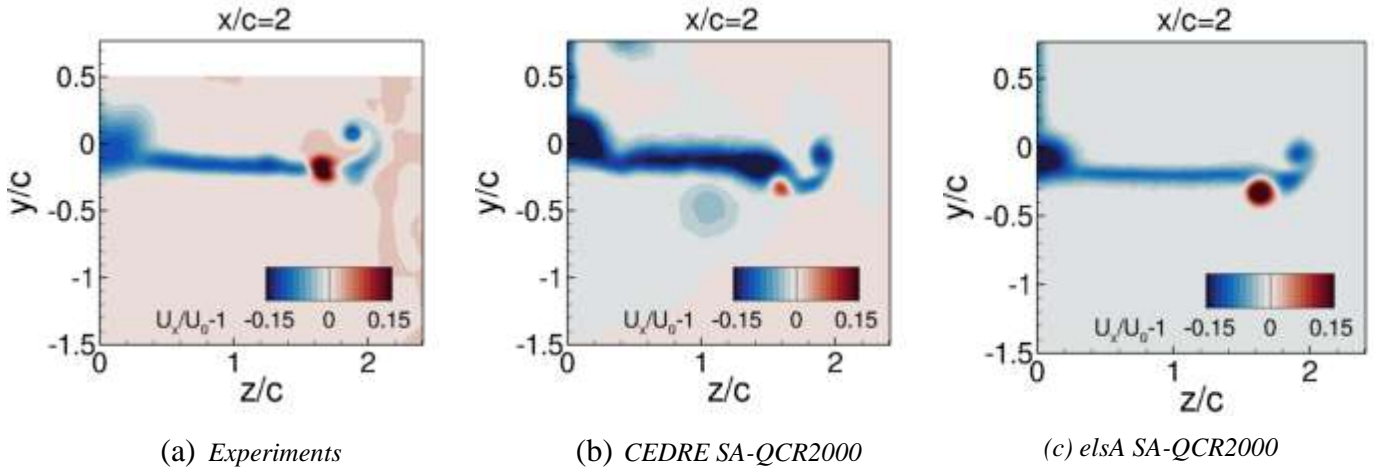


Figure 1-11: Velocity contours in the wake at 2 chords downstream of the wing trailing edge

The completion of this task for the remainder of the Climaviation project will therefore consist in a thorough review of the numerical parameters used for the CEDRE simulation, which should lead to a first set of exploitable simulation results to be assessed using the experimental data. A second set of simulations will be run using the mesh adaptation procedure currently used for the contrail simulations of complete aircraft with the CEDRE software to provide a quantitative assessment of this methodology and its combination with various turbulence models.

1.3. WP 1.3: Influence of aircraft configuration

Contributors: Rémy Annunziata and Nicolas Bonne (ONERA)

A recent paper, Saulgeot et al. (2023), presented in the Climaviation 2022-2023 report, highlights the impact of engine positioning on the optical properties of contrails under various atmospheric stratifications. However, this study is limited to a two-dimensional framework, initialized in the vortex regime, and does not account for the jet regime, its associated phenomena, or aircraft geometry, key factors in the early stages of contrail formation. To address these limitations, we investigate the influence of engine position on contrails using a realistic aircraft geometry, focusing on the near-field region, which includes the jet, vortex, and dissipation regimes over a five-minute contrail lifespan.

Reynolds-Averaged Navier-Stokes (RANS) simulations are performed for the jet regime (up to 5 seconds after effluent ejection from the engine) coupled with a mesh adaptation technique, while the vortex and dissipation regimes will be simulated using Large Eddy Simulation (LES) to accurately capture all vortex instabilities. The RANS-to-LES transition will follow the method developed by Bouhafid et al. (2024) (WP 1.4). Regarding microphysical processes, a Eulerian approach developed at ONERA by Khou et al. (2015) will be employed. This model considers only water vapour and soot emissions at the engine exit. Soot particles are modelled using a transport equation and treated as passive tracers within the flow. Condensation is initiated on soot particles once they become supersaturated with respect to liquid water, with condensation and evaporation accounted for through a source term. The numerical simulations will be conducted on the Common Research Model (CRM), representative of a B777. Given the high computational cost, three configurations will be examined (Figure 1-12): the first at $d_{j/b} = 0.34$, representative of a B777 or an A320 engine; the second at $d_{j/b} = 0.60$, corresponding to the outboard engine of a B747; and finally, an academic configuration at $d_{j/b} = 0.80$, aligning the jet with the wingtip vortex, which was found to be optimal in the previous 2D study.

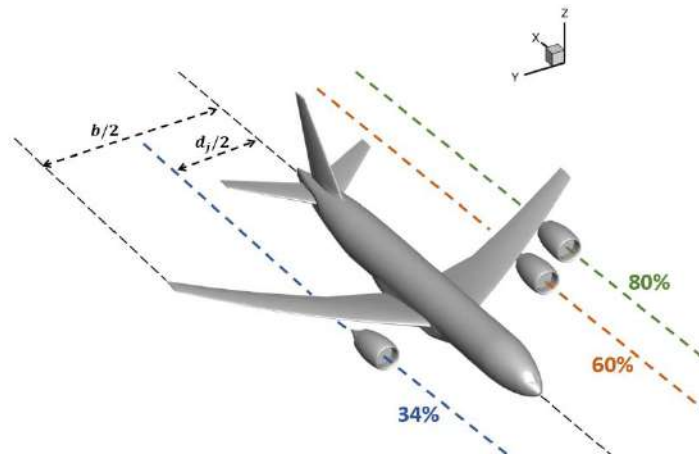


Figure 1-12: Engine positions considered in this study

The condensation trails obtained from the simulations are presented in Figure 1-13. These contrails are visualized using the iso-surface of ice water content (IWC). It can be observed that each induced contrail is highly dependent on the aerodynamic wake of the respective configuration. For the 34 % configuration, the condensation trail gradually stretches around the wingtip vortex. In the 60 % configuration, the contrail spreads into the wingtip vortex, resulting in a two-part structure: one segment associated with the jet and the other with the vortex. The 80 % configuration exhibits a similar behaviour, with one part linked to the jet and another merging into the interaction between two vortices, the wingtip vortex and a vortex generated by flow separation on the CRM wing, caused by the modified nacelle position. This flow separation also appears in the 60 % configuration but does not significantly impact the interaction between the jet and the wingtip vortex.

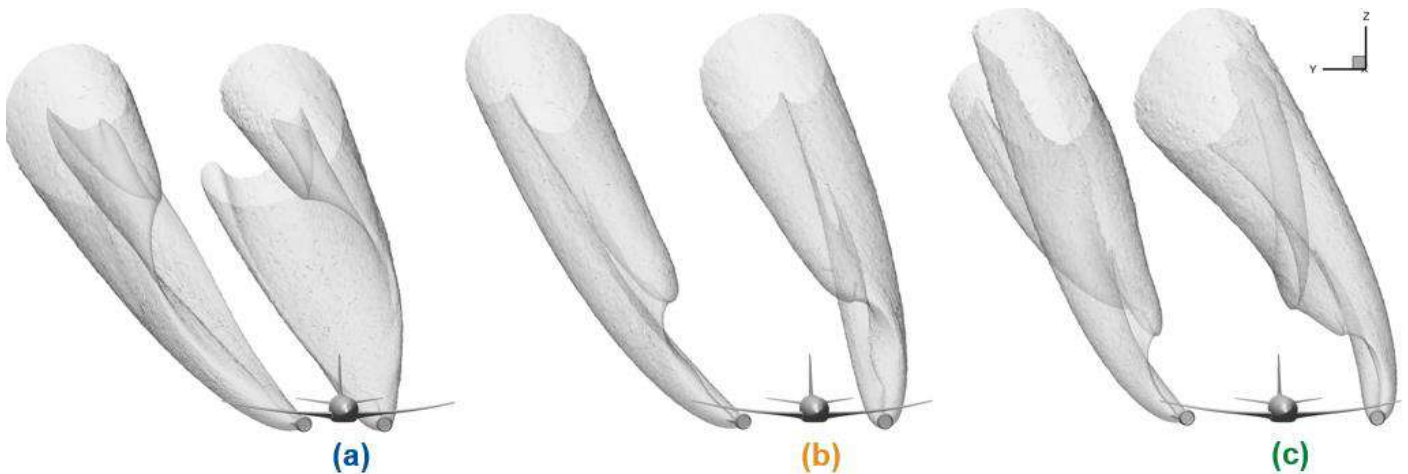


Figure 1-13: Iso-surface of $IWC = 1 * 10^{-6} \text{mg/m}^3$ for each case: (a) 34%; (b) 60%; and (c) 80%

These differences in how contrails form and the conditions they experience directly impact their average properties, as shown in Figure 1-14. Notably, variations between cases can be observed in the mean particle radius r_p and ice water content at the domain end. These differences can be attributed to the dilution occurring in the near-field region, 8 wingspans behind the aircraft. Due to the proximity of the jet to the wingtip vortex, the 80% and 60% configurations undergo the highest dilution. This increased dilution results in a more rapid cooling of the jets, leading to stronger local supersaturation with respect to both ice and liquid water. Consequently, condensation initiates earlier and more intensively in these cases compared to the 34% configuration, leading to larger ice particle radii and higher ice water content. This trend persists until the end

of the computational domain, despite a subsequent inversion in the dilution, as the contrail evolves within an ambient atmosphere that remains supersaturated with respect to ice ($RH_{i,\infty} = 110\%$).

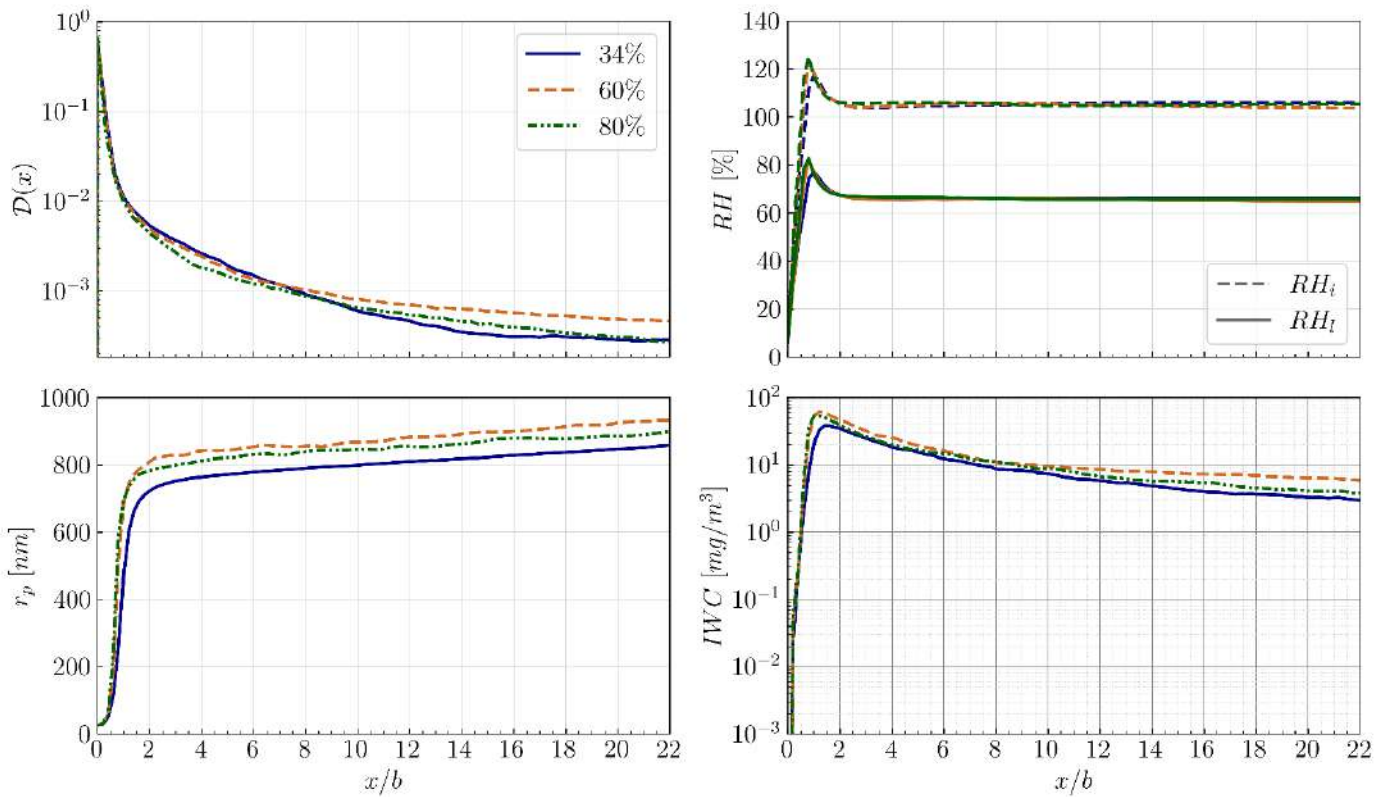


Figure 1-14: Average properties of contrails in each case as a function of distance behind the aircraft: dilution rate D (top left), relative humidity with respect to ice RH_i (dashed) and liquid water RH_l (solid) (top right), mean ice particle radius r_p (bottom left), and ice water content IWC (bottom right)

Given the differences observed in the jet regime, it is relevant to analyse the evolution of these contrails over a longer timescale in the vortex and dissipation regimes. As previously stated, LES simulations are initialised from a slice of the RANS flow field at a distance of $x/b = 18$ behind the aircraft for each case. To bridge the gap from RANS to LES, both jet and atmospheric turbulence are introduced. Additionally, atmospheric stratification is incorporated into the simulations, with a Brunt-Väisälä frequency of $N_{BV} = 0.012 \text{ s}^{-1}$ representing a moderately stratified atmosphere. The LES results are presented in Figure 1-15 after 2 minutes of simulation and at the end of the simulation (5 minutes). The ice water content (IWC) iso-surface is visualized similarly to the RANS simulations, along with the Q-criterion iso-surface coloured by the x-component of vorticity, allowing for an assessment of the aerodynamic evolution of the wake.

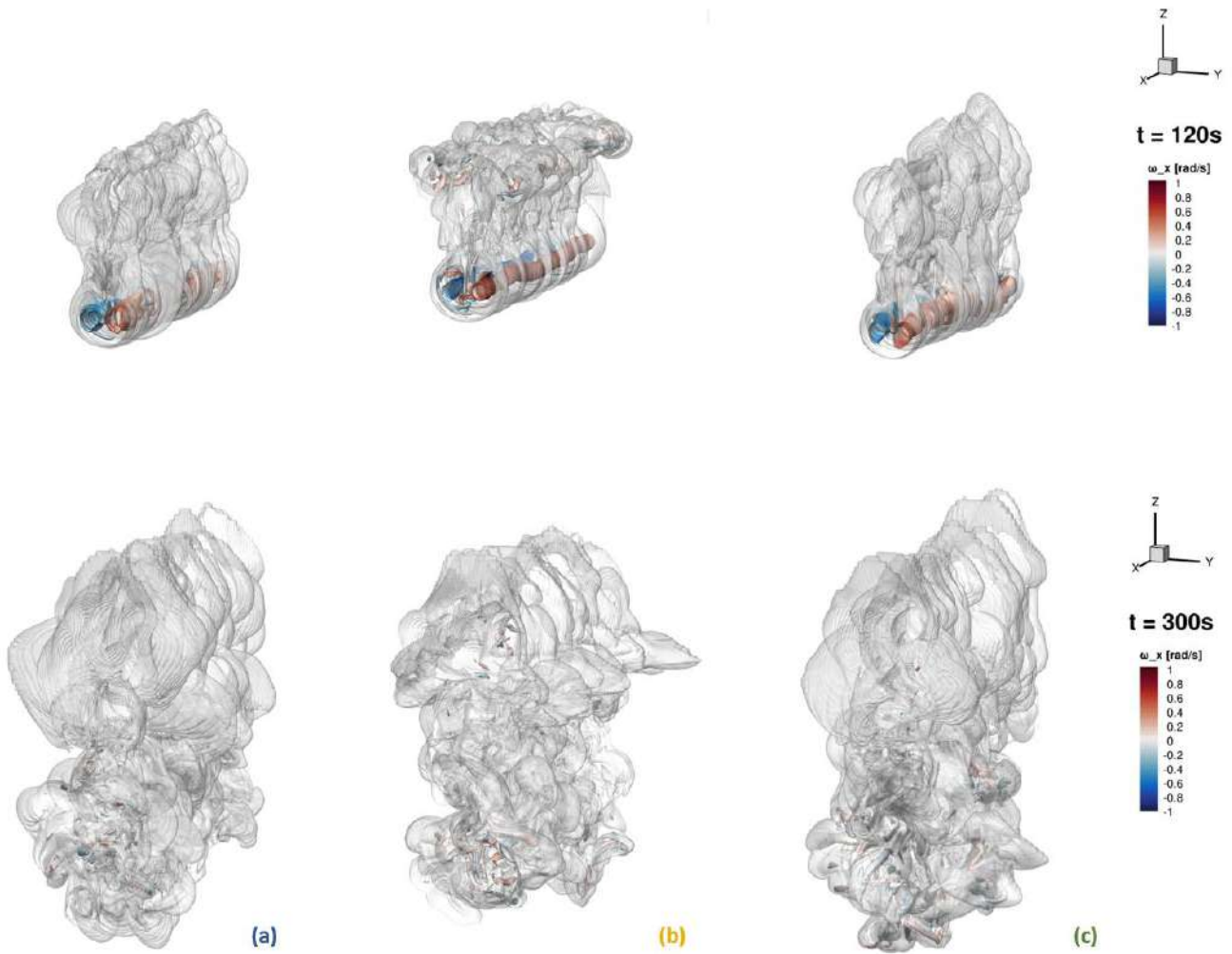


Figure 1-15: Iso-surface of ice water content (IWC) and Q -criterion iso-surface coloured by the x -component of vorticity at 2 minutes (top) and 5 minutes (bottom) of simulation

As with the RANS simulations, the evolution of condensation trails in LES strongly depends on the aerodynamic wake dynamics, which vary slightly across configurations. These differences once again impact the average properties, shown in Figure 1-16, including the induced contrail altitude Δz_c , mean ice crystal radius r_p , total ice mass m_i , and optical thickness τ_p .

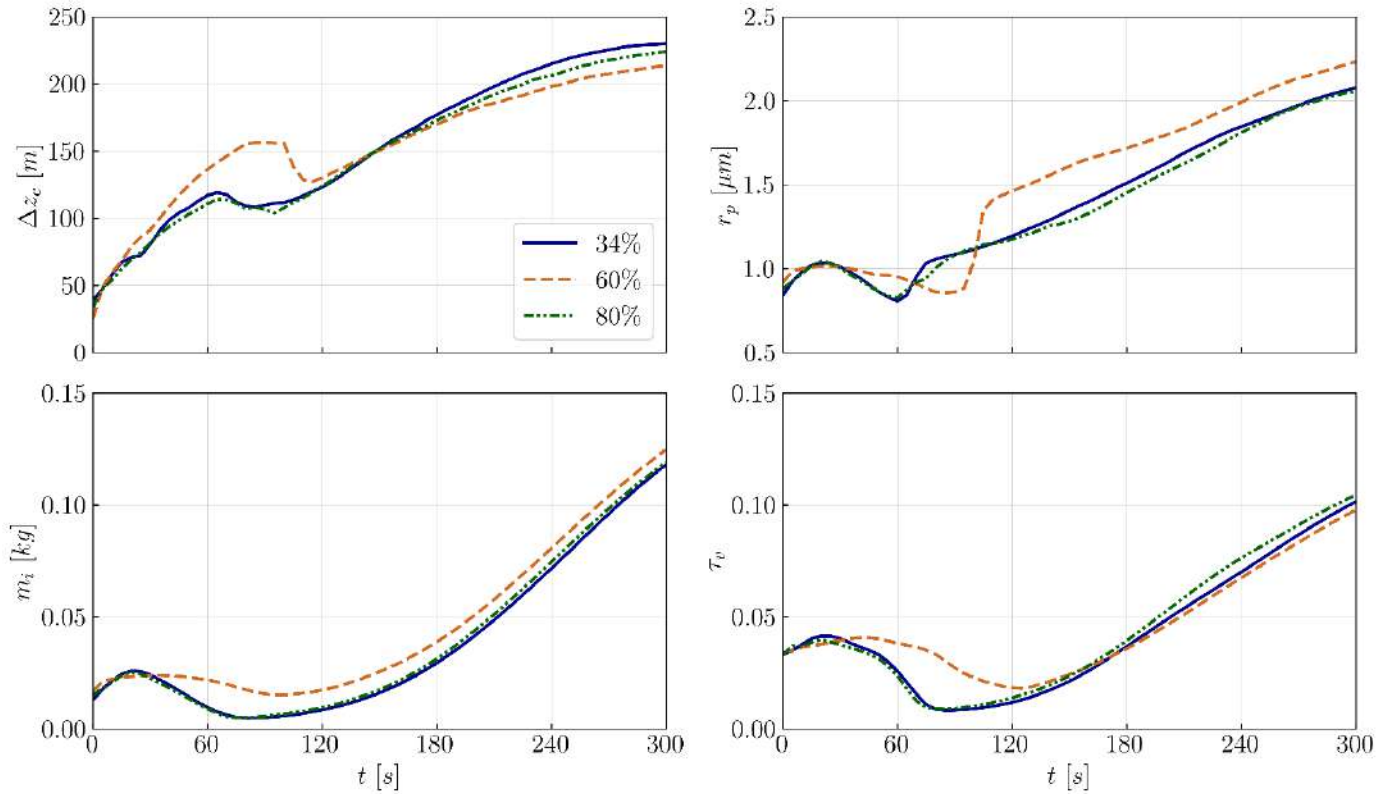


Figure 1-16: Average properties of condensation trails in each case as a function of time: induced contrail altitude Δz_c (top left), mean ice crystal radius r_p (top right), total ice mass m_i (bottom left), and optical thickness τ_v . (bottom right)

Overall, the average properties of each contrail tend to converge towards the end of the computational domain. As a result, the contrails exhibit similar total ice content and optical thickness at the end of the simulation. The most notable differences appear in the 60 % configuration, where additional vortex structures help retain a greater fraction of ice crystals at cruising altitude compared to the other cases. These crystals do not undergo melting due to adiabatic compression, as they are not entrained within the wingtip vortex pair. However, these detached vortices dissipate after 2 minutes of simulation, after which the contrail evolution aligns with the other cases. This uniformity in contrail properties was anticipated. With a moderate stratification, i.e. inverse Froude number at 0.3, no significant differences were expected between cases, as previously shown in the 2D study. This result is now confirmed while considering the jet regime and over a longer simulation time. Further simulations with stronger atmospheric stratification, predicted by the 2D study to produce more distinct differences, are currently in progress to assess whether these expected variations will indeed emerge. Finally, this study raises questions about the microphysical model, which remains overly simplistic. Future improvements could include a more detailed representation (soot polydispersion, a Lagrangian approach, etc) among other refinements.

1.4. WP 1.4: Evolution of contrails at intermediate scales

The first objective of work package 1.4 is to set up a simulation methodology for the intermediate scales that cannot be calculated with the spatial and stationary simulation approaches (Reynolds Averaged Navier-Stokes, RANS) used for the near field immediately downstream of the aircraft. One will need to identify the characteristics of the contrails, beyond their initial formation phase and the disappearance of the disturbance generated by the aircraft, which will make it possible to define the parameterizations of the properties of the contrails in the climate models. A second objective is to interface with the near-field RANS simulations to

consider all the physics of the jet regime in the calculation of the development of contrails at intermediate scales. This is to better understand the influence of the near-field and the aircraft configuration on the large-scale properties of the contrail, an influence that remains poorly understood.

1.4.1. Interface between the near field (jet regime) and the intermediate field

Contributors: Younes Bouhafid and Nicolas Bonne (ONERA)

Last year, the methodology to initialize a phase vortex LES based on a former RANS jet phase simulation was presented. This approach has been compared to the usual approach using analytical initialization using Lamb Oseen vortices. These results have been shown only from an aerodynamic point of view. It has been observed a much more turbulent secondary wake suggesting the possibility to have a larger contrail using the RANS approach than using the analytical one. This year, the microphysical process using the model from Khou et al. (2015) have been included in both RANS and LES to have a conclusion on contrail properties. For simplicity, only the LES results are shown in this report.

As last year LES computation has been made either using a former RANS simulation or using a two Lamb Oseen analytical initialization. Since the RANS field include also two more vortices coming from the tailplane, a third initialization strategy has been tested using four Lamb Oseen analytical vortices. Their properties have been fixed based on the vortices obtained by the RANS simulation. A scheme of these three different kinds of initialization is shown in Figure 1-17.

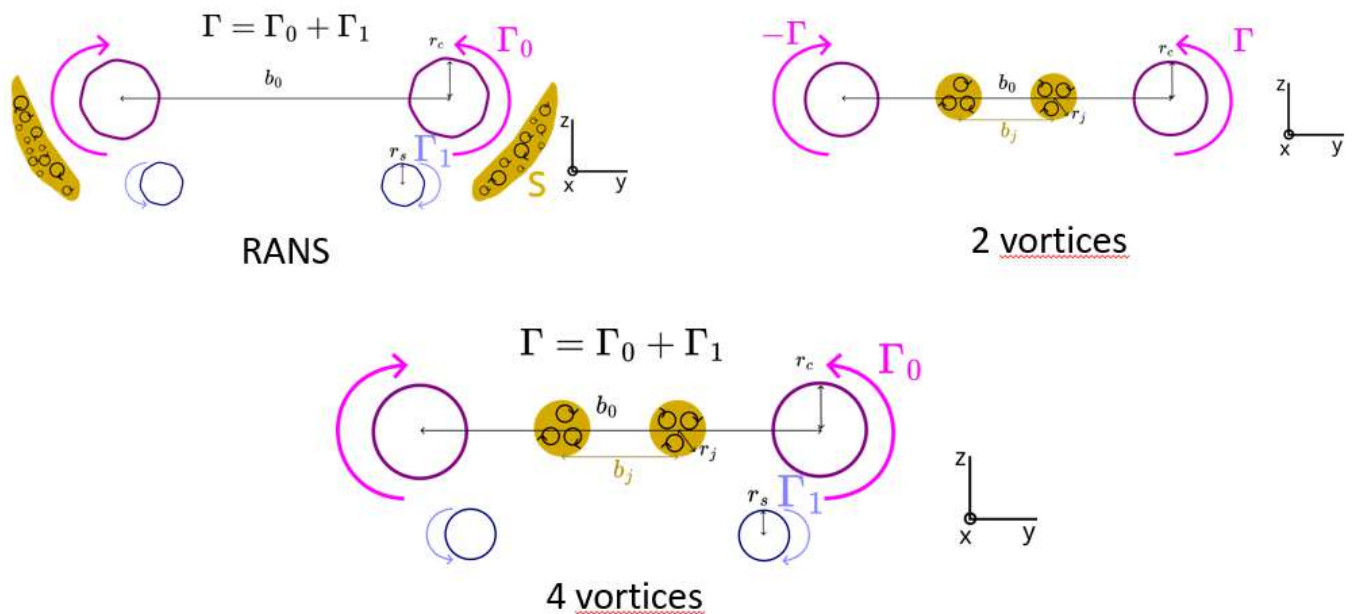


Figure 1-17: Summary of the three initialization strategies

The height and width and surface evolutions of the three different contrail initialisations can be seen in Figure 1-18. While the contrail height evolution is in good agreement between the RANS and the 4 vortices cases, some differences are visible with the 2 vortices cases. The main differences appear in their width, the 2-vortex case having a much smaller width than the two other cases. This is because the secondary wake is much more turbulent in a 4-vortex case than in the 2-vortex case. This difference between 2 and 4 vortex behaviour can be explained by short wave instabilities present in a 4-vortex system as shown in Fabre &

Jacquín (2002). This kind of system has a most amplified short-wave instability in addition of the usual crow instability. This leads to force smaller structures in the fluid creating more turbulence.

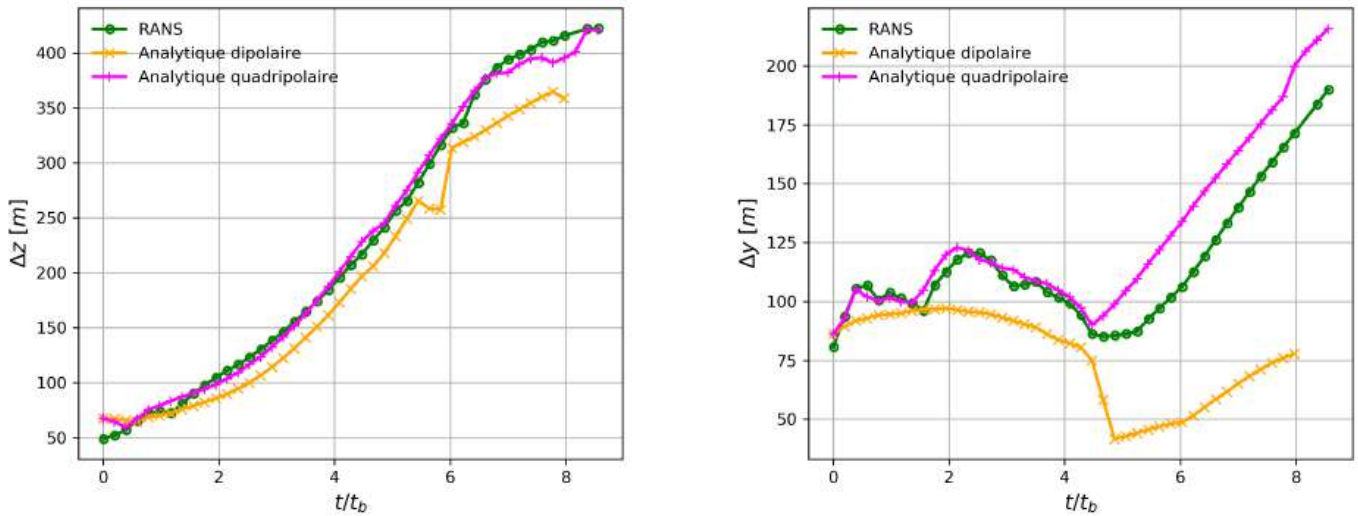


Figure 1-18: (Left) contrail height time evolution for RANS initialization (green), 2 vortices (yellow) and 4 vortices (purple). (Right) contrail width time evolution

Comparing the RANS initialization with the 4-vortex analytical initialisation, differences remain. Since Section 1.3 has shown that some differences can remain when moving the engines of the aircraft, it is possible that these differences can be explained by the difference in terms of ice crystal position at the initialization time of the LES calculation.

1.4.2. Simulation of contrail aging using a numerical weather model

Contributors: Aurélie Bouchard and Magalie Buguet (ONERA)

Previous studies have been done on the contrail simulation during the vortex phase with the mesoscale numerical weather code, Méso-NH in an idealized approach, applying a Lamb Oseen model for the contrail initialization (see 2nd and 3rd Climaviation Annual Reports). To follow a more realistic approach, contrail simulation across the dissipation regime has been run using Méso-NH with a realistic atmosphere.

Thus, a real study case has been defined based on contrails detected using satellite data in Wang et al. (2024). The date of the 23rd of June 2020 in the morning at 9h UTC has been chosen for the study, focusing on the south of Brittany (France). To do this simulation of a realistic meteorological situation, the output of the ERA5 reanalysis has been used as boundary conditions for the Méso-NH code. Firstly, map of high cloud cover and relative humidity versus ice have been plotted at 250 hPa (near the flight altitude and consequently, contrail formation altitude). Results are presented on Figure 1-19. Rectangles on Panel (a) indicate the geographical area of the Méso-NH simulation. Pictures highlight that Méso-NH domains are in an area with the presence of high cloud cover and a relative humidity with respect to ice over 100 %. This information is favourable with possible development of contrails. Finally, it is important to mention a north-eastward horizontal wind in the domain at 250 hPa, which will affect the trajectory of the contrail.

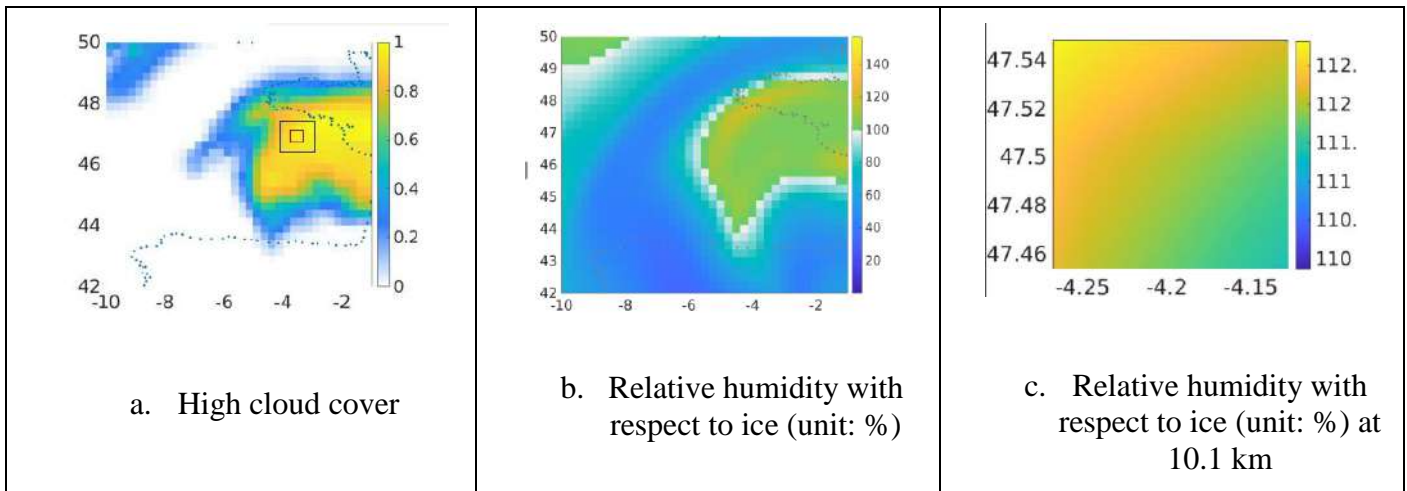


Figure 1-19: Map of (a) high cloud cover and (b) relative humidity with respect to ice (on the middle) at 250 hPa, the 06/23/2020 at 9h UTC, in ERA5. On x-axis, the longitude and on y-axis, the latitude.

This information illustrates the background field of the Méso-NH simulation. To simulate the evolution of contrail, two kinds of initialization are added to the background field.

The first one is the use of the Lamb Oseen model adapted for a CRM by Vassberg et al. (2008) and based with the modelling of four vortices associated to tail vortex and wings vortex. Positions and vortex characteristics have been extracted from Ghedhaifi et al. (2019) and Bouhafid et al. (2024). The four vortices are injected in an idealized and stratified atmosphere as in previous Climaviation Annual Reports (2nd version in 2022 and 3rd in 2024). The geographical domain for this idealized simulation is $200 \text{ m} \times 270 \text{ m} \times 540 \text{ m}$ respectively in x, y, z dimension, with a spatial resolution, respectively of $4 \text{ m} \times 1 \text{ m} \times 1 \text{ m}$. Results obtained at 300s are plotted on the left-hand side of Figure 1-20.

The second one is extracted from a CEDRE simulation of a contrail based on a realistic approach of the jet regime. Results at 300s are presented on the right-hand side of Figure 1-20.

Each of both kinds of initialisation are injected in the inner domain of the Méso-NH code by spatial interpolation and between 10 and 11 km in vertical, to be consistent with flight altitude. For this simulation, the vertical grid of Méso-NH (extended from the ground to 12 km) has been stretched in this specific vertical area. The grid nesting principle is used for this case with a spatial resolution of 4 m for the inner domain and 12 m for the outer domain. Domain extensions are 1.2 km and 3.6 km, respectively. Once the initialisation done, the model runs until 200 s of contrail lifetime.

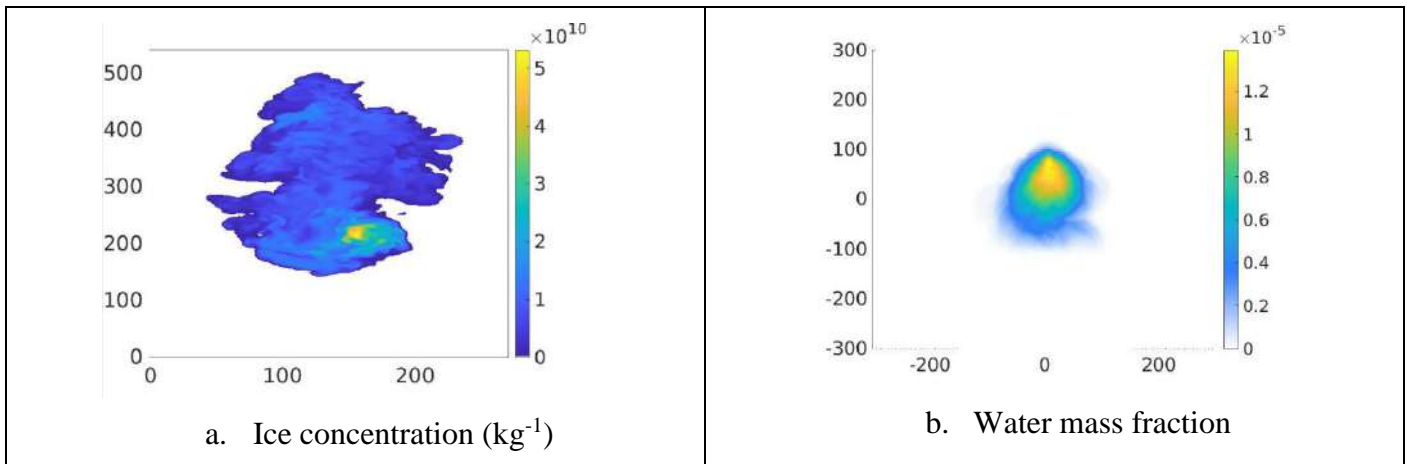


Figure 1-20: On the left side, vertical section near the centre of the domain, of the ice concentration (unit: kg^{-1}) for the Lamb Oseen simulation at 300 s. On y-axis, the altitude in m, on x-axis, the position in y in m. On the right side, vertical section of water mass fraction taken from the CEDRE simulation at 300 s

To upscale to a larger domain of $10.8 \text{ km} \times 10.8 \text{ km}$ (outer domain, with a resolution of 36 m), the outer domain of the precedent simulation becomes the inner domain (horizontal dimension: 3.6 km, resolution 12 m) of the new simulation. In this inner domain, a concatenation of several step ranges of the previous simulation are done. Indeed, it is important to take into account that the aircraft moves in the domain. Results obtained for both kind of initialisation are plotted on Figure 1-21, for the Lamb Oseen initialization and on Figure 1-22 for the CEDRE initialisation.

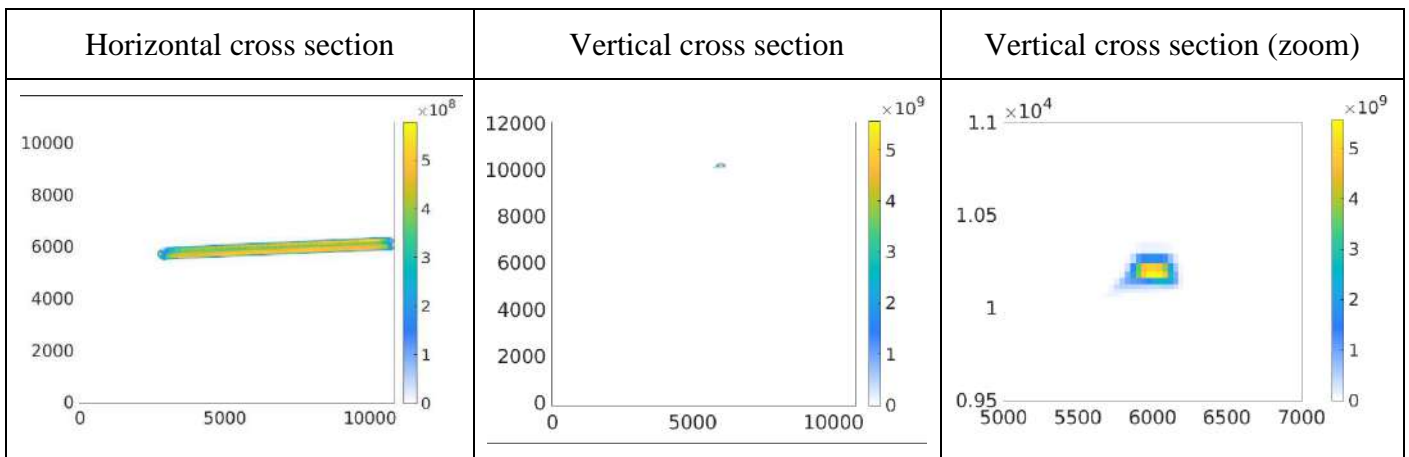


Figure 1-21: Cross section of the ice concentration (unit: kg), with the Lamb Oseen initialisation. Axes for horizontal cross section are X position on x-axis and Y position on y-axis. Axes for vertical cross section Y position on x-axis and altitude on y-axis. Unit for all axes are in m. The right panel is a zoom in vertical of the middle picture. Results after 150 s.

Results presented on Figure 1-21 have been obtained with a time period of [160 s – 200 s] for the spatial interpolation for this domain. They have been obtained after 150 s of this new simulation, corresponding at around 10 minutes of contrail lifetime. Results presented on Figure 1-22 have been obtained with a time period of [60 s – 100 s] for the spatial interpolation. They have been obtained after 100 s of the new simulation, corresponding at around 8 minutes of contrail lifetime.

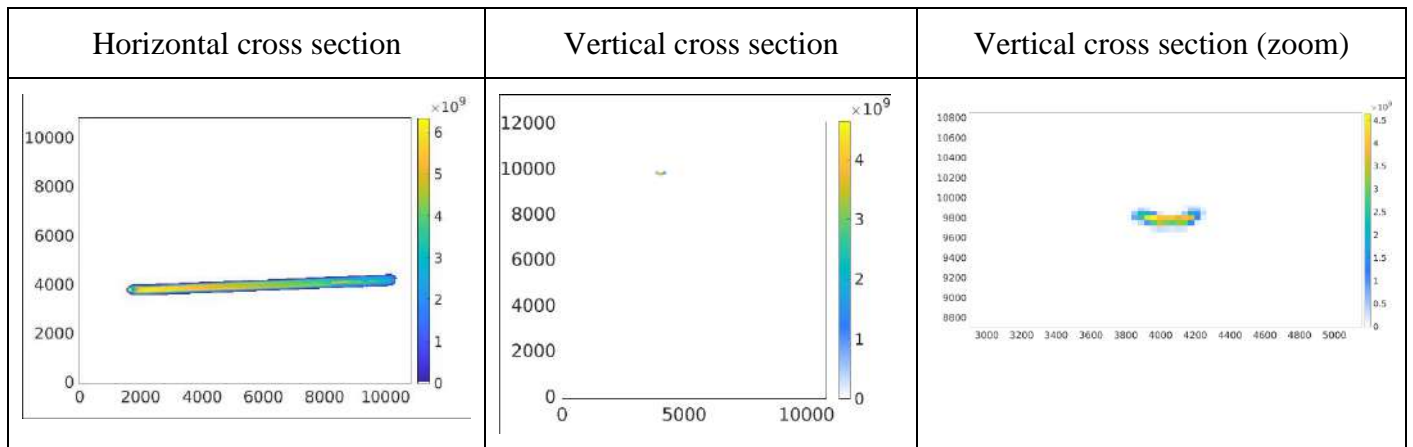


Figure 1-22: Cross section of the ice concentration (unit: /kg), with CEDRE initialisation. Axes for horizontal cross section are X position on x-axis and Y position on y-axis. Axes for vertical cross section Y position on x-axis and altitude on y-axis. Unit for all axes are in m. The right picture is a zoom in vertical of the middle picture. Results after 100 s.

The present study shows the feasibility of upscaling until the dissipation regime with a meteorological model, to study the contrail evolution in a realistic atmosphere. At the end of the simulation, the geographical domains match the needs of climate parametrization, after about 7.5 minutes of a contrail lifetime in a geographical domain about 15 km large. The two kinds of initialisation show differences since 300 s, which affects the simulation of contrail evolution.

Future development will concentrate on the validation of these preliminary results, continued work on the upscaling in a realistic atmosphere and comparison with observations.

1.5. WP 1.5: Evolution of contrails on climatic scales

The objective of work package 1.5 is to simulate the evolution of contrails at the synoptic scale. The atmospheric general circulation model LMDZ, which is a component of the IPSL climate model, will be used to do so.

1.5.1. Modelling ice supersaturation and contrails in LMDZ

Contributors: Audran Borella, Étienne Vignon, Olivier Boucher, Jérémie Juvin-Quarroz (IPSL)

A new ice cloud scheme that allows for both ice supersaturation in clear sky and ice sub- and supersaturation in cirrus clouds has been implemented in the LMDZ atmospheric general circulation model (Borella et al., 2024, submitted; Climaviation Annual Report 2024). This parameterisation has been evaluated using a case study of a warm conveyor belt cirrus cloud above the Paris area on the 27/12/2022. Comparing the observations made during this event to simulated cirrus cloud reveals that the new parameterisation better represents ice cloud fraction and relative humidity w.r.t. ice. In particular, LMDZ previously had a cold and dry bias in the upper troposphere and mid-latitudes, but with the new parameterisation the atmosphere is much moister, in line with the observations (radiosoundings, IASI) and the ERA5 reanalysis product. A glimpse of the comparison is shown in Figure 1-23, and the full comparison can be found in the preprint publication (Borella et al. (2024, submitted)).

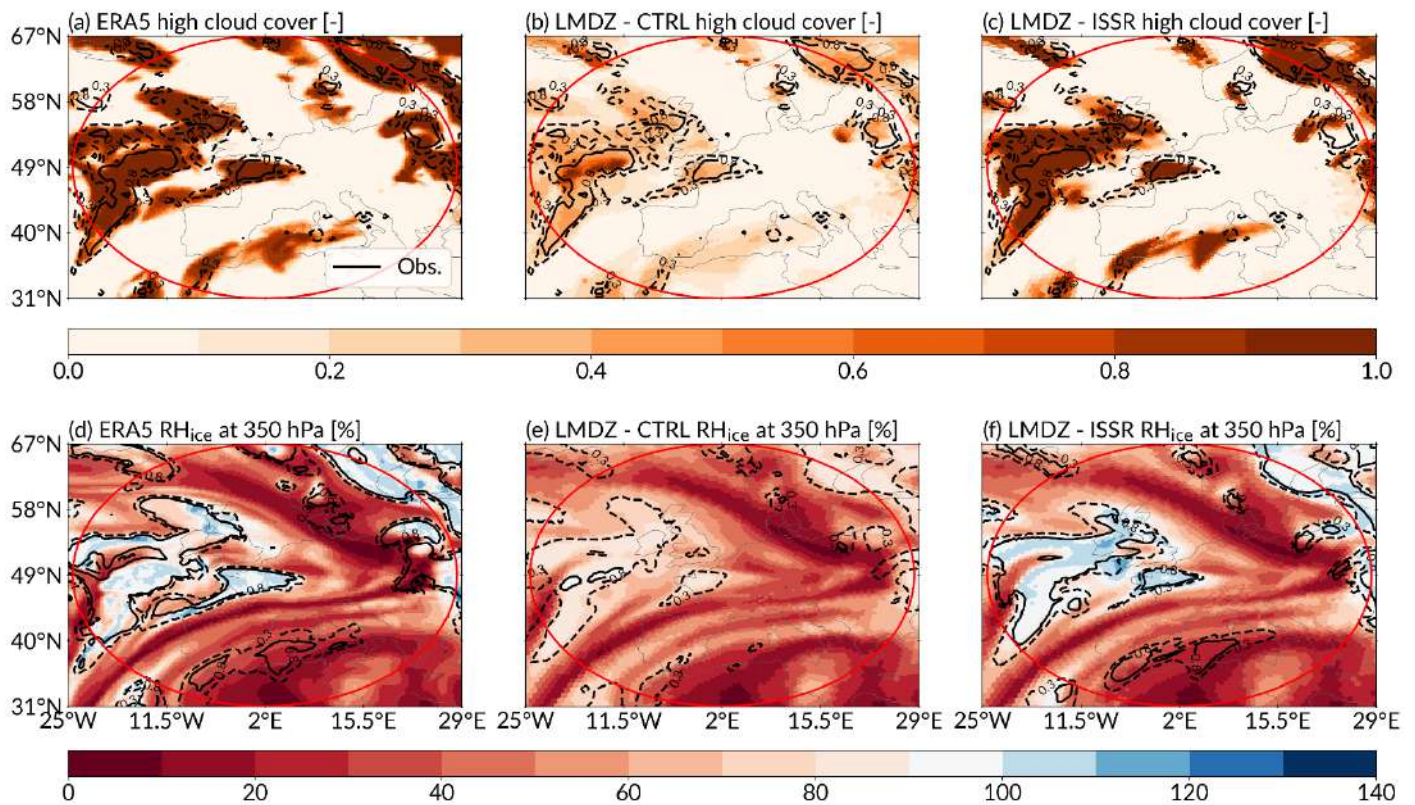


Figure 1-23: (a, b, c) High cloud cover from (a) the ERA5 reanalysis, (b) the CTRL ICOLMDZ simulation, (c) the ISSR ICOLMDZ simulation, at 04:00 UTC on the 27th December 2022. Dashed and solid black contours represent the 0.3 and 0.8 cloud cover from Meteosat-10 observations, respectively. The Meteosat-10 original measurements have been regridded to a regular $0.75^\circ \times 0.75^\circ$ longitude-latitude grid. (d, e, f) Relative humidity w.r.t. ice at 350 hPa (about 8 km) for the same three simulations at the same time. The dashed and solid black contours represent the 0.3 and 0.8 high cloud cover fractions, respectively.

With the new parameterisation implemented, the quality targets of LMDZ in terms of radiative and precipitation metrics were not reached. A new tuning of the model will be done in the future following the method described in Sanogo et al. (2025, submitted), but in the meantime a perturbed parameter ensemble (PPE) was run to find the best set of parameters that allow the model to reach quality targets. Running the model with the new parameterisation and the new set of parameters on the global scale for 10 years revealed that the high cloud cover simulated by the model is much closer to the observations than before. Moreover, as qualitatively described in the case study, the upper troposphere is moister, in line with the ERA5 reanalysis (Figure 1-24). However, there is now a wet bias in the lower stratosphere, which increases the cold bias in this region. Although this wet and cold bias of the lower stratosphere at the poles is a common feature of many AGCMs (Charlesworth et al., 2023), it may change the behaviour of contrails and will need to be corrected.

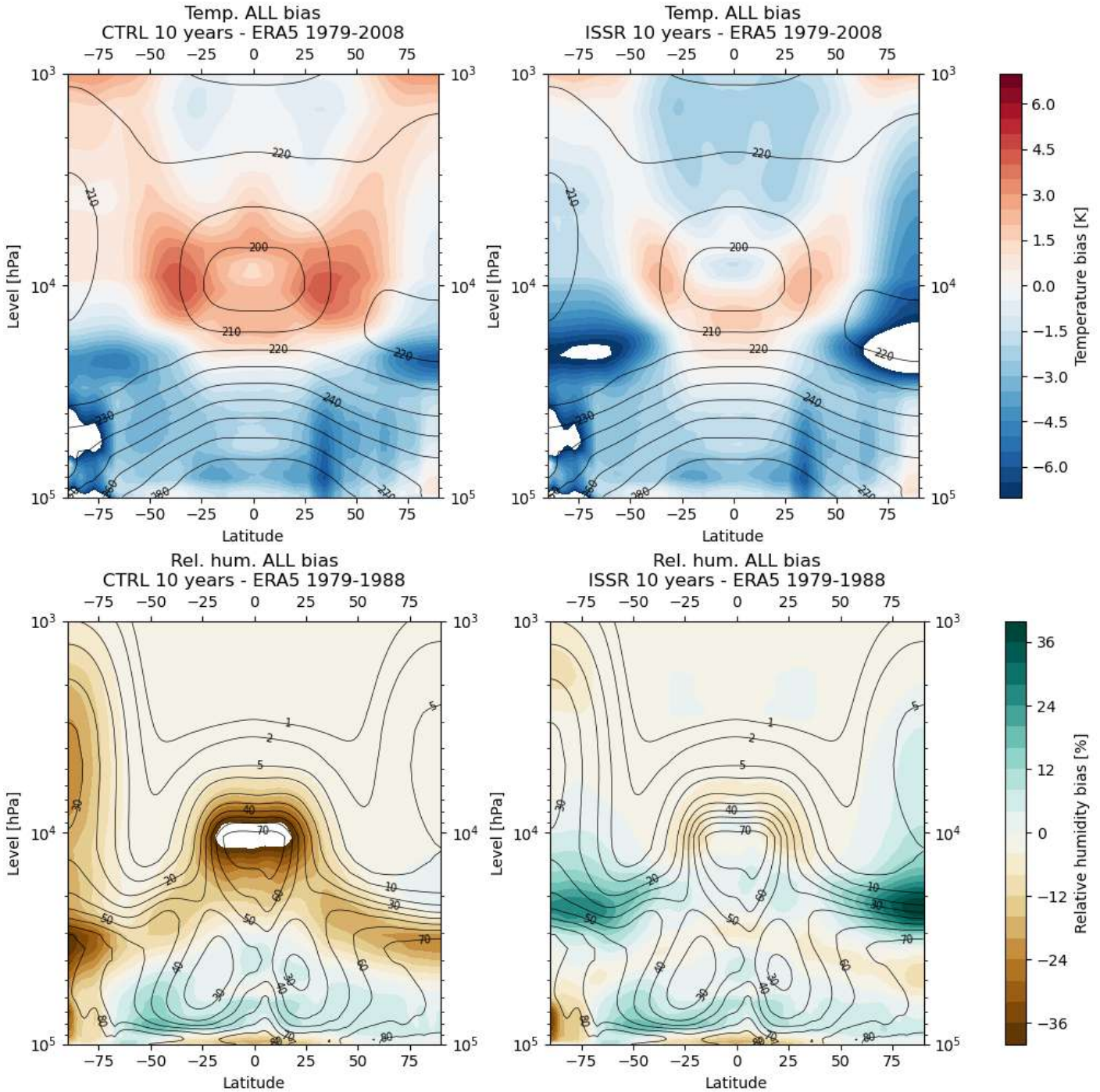


Figure 1-24: Zonal biases between the LMDZ simulations and the ERA5 reanalysis, averaged over 10 years of LMDZ simulation and 30 years of ERA5 data. First column: LMDZ without the new parameterisation, second column: LMDZ with the new parameterisation. First line: temperature bias [K], second line: relative humidity with respect to ice bias [%]. The black contours show the absolute values from the ERA5 reanalysis.

The simulation of persistent contrails has been implemented in LMDZ following preliminary work described in the Climaviation Annual Report 2023-2024. Additional work is needed to calibrate and validate the contrail parameterisation before consolidated results can be obtained. In particular, the upper tropospheric cold bias must be addressed. Persistent contrails are generated only if the Schmidt-Appleman criteria is verified in ice

supersaturated regions. A key feature of the parameterisation is that persistent linear contrail fraction is treated as a prognostic variable that is advected by the dynamical core of LMDZ. Persistent linear contrails form with a prescribed width and depth, which are fixed for the time being. Future work will consist in parameterising width as a function of temperature, relative humidity and Brunt-Väisälä frequency, using results from the LES simulations ran by the ONERA. Persistent linear contrails then transform into contrail cirrus with a given characteristic timescale, and these contrails cannot be distinguished from natural cirrus clouds in the current parameterisation. However, to assess the radiative forcing of contrail cirrus, a new cloud class will be implemented for contrail cirrus (such as persistent linear contrails). A test simulation has been run. Figure 1-25a shows the simulated newly formed persistent contrail fraction averaged over one year, while Figure 1-25b shows the average total persistent contrail fraction. This simulation was done using the GAIA flight inventory for the year 2019 (Teoh et al., 2024).

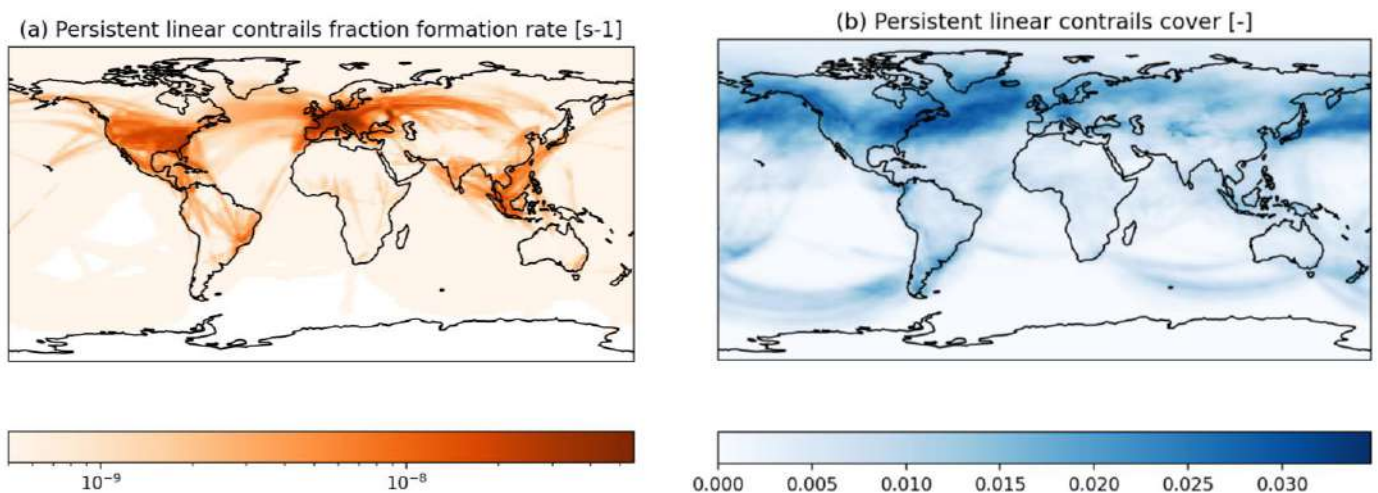


Figure 1-25: (a) Persistent linear contrails fraction formation rate [s^{-1}] averaged over one year, showing the maximum value of the vertical profile in each column. (b) Persistent linear contrails cover. This cover does not yet include contrail cirrus.

1.5.2. Response of the climate system adjustments to a perturbation in cirrus cloud cover

Contributors: Jérémie Juvin-Quarroz, Olivier Boucher, Nicolas Bellouin, Audran Borella (IPSL)

The objective of this study is to examine how the climate system adjusts in response to a perturbation in cirrus cloud cover. We developed a systematic and statistically robust method to evaluate the effective radiative forcing and, in a future step, the efficacy of this perturbation in altering global surface air temperature (GSAT) within LMDZ6A, the general circulation model used in the IPSL climate model framework.

Evaluating the effective radiative forcing and efficacy of contrails is challenging. From an observational perspective, contrail cirrus are difficult to distinguish from natural cirrus clouds, whether observed from the ground or by satellite. From a modelling perspective, the relatively small radiative forcing of contrails makes it hard to detect against the background variability of the climate system. In a recent model study (Bickel et al., 2020), air traffic density had to be significantly increased to obtain statistically significant results.

We conduct an idealised experiment in which all the water vapour present in ice-supersaturated regions is instantaneously converted into clouds during a single model timestep. The effects of this perturbation are then quantified over a four-day period to focus on short-term atmospheric adjustments. Focusing on such a brief timescale also ensures that there is virtually no change in global surface air temperature (GSAT).

To isolate the signal from background variability, we create an ensemble of simulation pairs—each consisting of one perturbed and one unperturbed simulation. Starting from a set of initial conditions (ICs), we introduce Gaussian noise into the sea surface temperature field. To decorrelate these initial conditions, we run a multi-

day spin-up, resulting in an ensemble of distinct ICs that can be used to generate corresponding perturbations. This setup enables statistical testing that effectively isolates the signal from atmospheric background noise. Furthermore, additional simulation pairs can be added to the ensemble to improve the robustness of the statistical analysis.

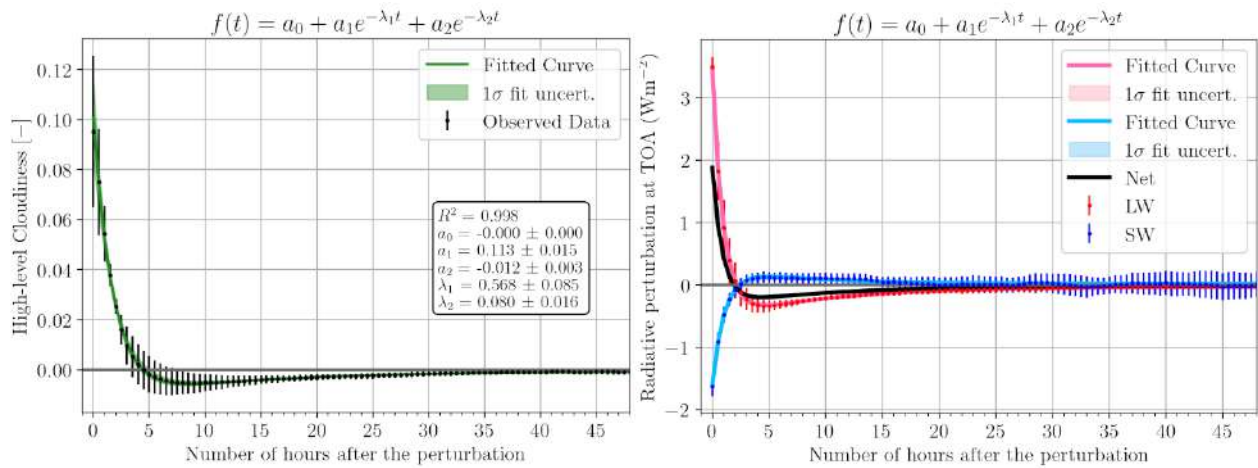


Figure 1-26: Perturbation to high-level cloudiness (left) and top-of-atmosphere (TOA) radiation (right). On the left, the black points represent ensemble-averaged data from $N = 49$ simulation pairs, with vertical bars indicating the standard deviation. The evolution of the perturbation takes the shape of the difference between two decreasing exponentials with distinct decay constants, as illustrated by the green curve. Similarly, on the right, the longwave (LW, red), shortwave (SW, blue), and net radiative perturbations (black) are shown, each accompanied by corresponding fitted curves.

Figure 1-26 shows the perturbations to high-level cloudiness and top-of-atmosphere (TOA) radiation, averaged over $N = 49$ simulation pairs. Both perturbations exhibit a behaviour consistent with the difference between two decreasing exponentials with distinct decay constants. On the left-hand side of Figure 1-26, the initial peak corresponds to a decay time of 1.76 ± 0.26 hours, which reflects the sedimentation of cirrus clouds formed immediately following the perturbation. The substantial increase in cloud cover—by approximately 10%—is followed after about 5 hours by a decrease of about 1%, likely due to the depletion of atmospheric humidity caused by precipitation. On the right-hand side of Figure 1-26, the LW radiation perturbation mirrors this behaviour, which can be attributed to the greenhouse effect of cirrus clouds. We find that the shape of these curves is highly sensitive to a tuning parameter that defines the ice crystal fall speed (here 0.4). A higher value of this parameter results in a greater initial increase in cloud fraction and radiative effect and a deeper decrease.

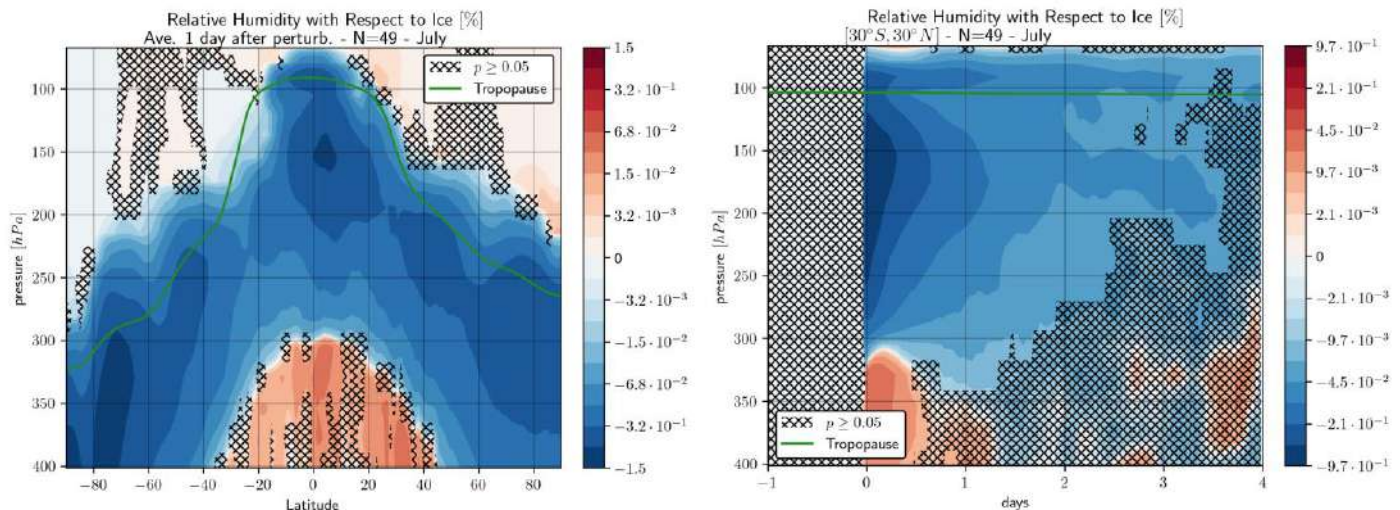


Figure 1-27: Vertical distribution (left) and time evolution (right) of the perturbation to relative humidity with respect to ice (RH_i). On the left, the data are averaged over the first day following the perturbation, while on the right, the data are averaged over the mid-northern latitude range. The green line indicates the tropopause level. The hashed regions represent data points that do not pass a Student's *t*-test at a 5% significance level ($p = 0.05$).

Figure 1-27 shows the vertical distribution and time evolution of the perturbation to relative humidity with respect to ice (RH_i). Within one day after the perturbation, a decrease in RH_i is observed, which follows the contour of the tropopause. At lower altitudes, an increase in RH_i indicates the sedimentation of cirrus clouds. On the right side of Figure 1-27, the reduction in RH_i near the tropopause persists for up to four days.

Our results demonstrate that the methodology is sufficiently robust to capture the key physical processes involved in the adjustment and to determine characteristic time constants with associated uncertainties. However, the simulations exhibit a cold bias of 5 K at 200 hPa, which lowers the saturation vapor pressure. This bias should be corrected in future work to improve the accuracy of the results.

1.6. WP 1.6: Detailed study of the radiative impact of contrails

The objective of Work Package 1.6 is to compare several numerical methods for solving the radiative transfer equation at the scale of a contrail and/or cirrus cloud. The limitations of each of these methods will be evaluated, especially in terms of their ability to consider spatial heterogeneities. Then, we will check if the assumptions made in the global models of the IPSL are appropriate, to improve or correct, if necessary, the parameterisation on which these global models are based.

1.6.1. ONERA model developments and benchmarks

Contributors: Christophe Bellisario, Claire Malherbe, Audrey Benteyn, Etienne Terrenoire, and Lionel Tessé (ONERA).

In the previous annual report, we presented the use of the international reference code ModTRAN by Berk et al. (2014) to compute the net fluxes for cloudy environments. In addition, we did the same computation with the radiative transfer model developed at ONERA, MATISSE, by Labarre et al. (2016). However, the version of MATISSE used at this time only performed the computation between 700 and 25000 cm^{-1} . Therefore, the

outside bands had to be computed by ModTRAN. With this method, we added another estimation of the radiative forcing on the benchmark presented by Myrhe et al. (2009).

Over the last year, the radiative transfer model MATISSE has been updated to encompass the missing spectral bands. In detail, the wavenumbers in MATISSE version 3.7 starts from 50 up to 40000 cm^{-1} . The database associated has also been updated, regarding the molecules, aerosols and clouds. The validation of the spectral extension has been performed by comparison with ModTRAN computation. Examples of spectral radiance computation cases are displayed in Figure 1-28, with on the left, the transmission and on the right, the radiance. The top panels are without aerosols and the bottom panels are with aerosols. In this case, the configuration is summarized in Table 1-2.

Table 1-2: Configuration of the atmospheric state and observation angle for Figure 1-28.

Observation altitude	100 km
Observation zenith angle	180 °
Atmosphere	US Standard
Longitude; Latitude	0 °; 45 °
Emissivity	1
Ground temperature	288.15 K
Date	21 st of June, 12:00 UT
Aerosol visibility	23 km

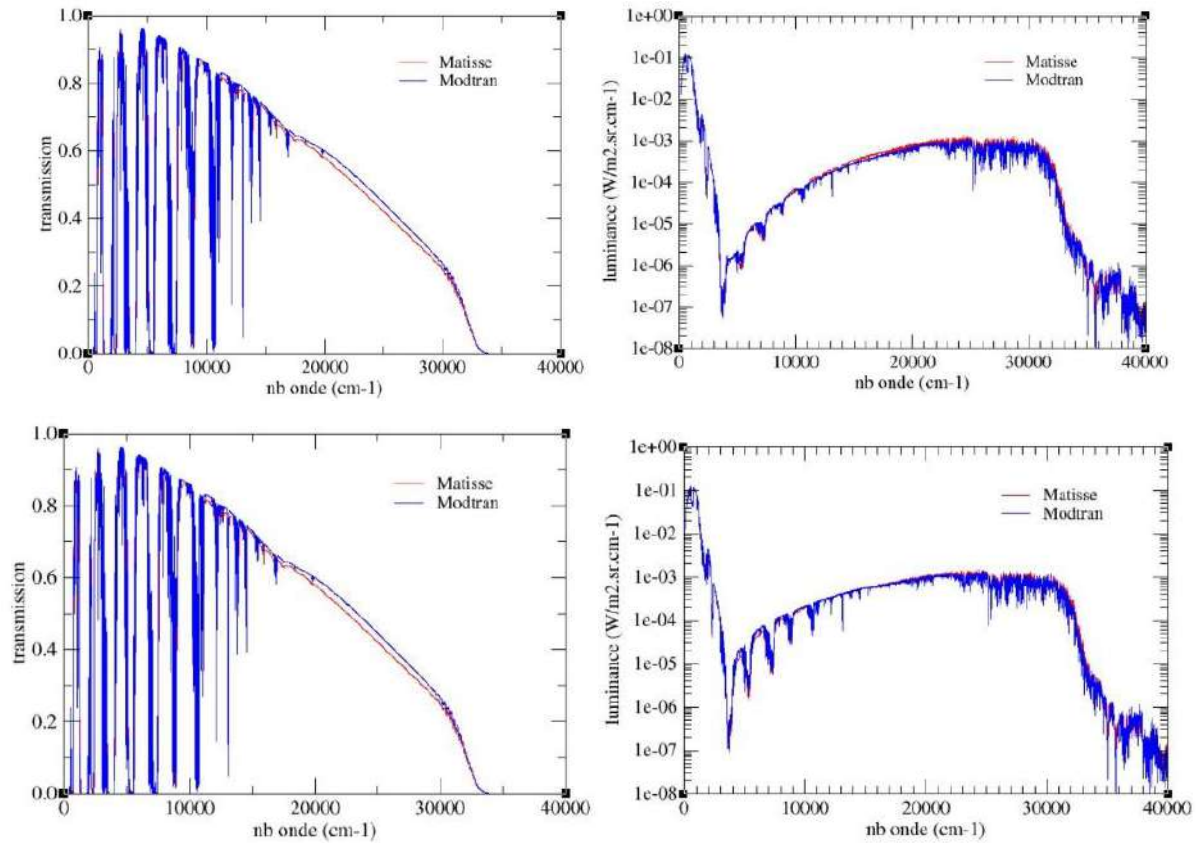


Figure 1-28: Transmission (left-hand side panels) and radiance (in $W m^{-2} sr^{-1} (cm^{-1})^{-1}$, right-hand side panels) computed with MATISSE (red) and ModTRAN (blue) for the case described in Myhre et al. (2009). The upper panels are without aerosols and the bottom panels are with aerosols (rural model with a visibility of 23 km).

The updated and validated version of MATISSE has been used to perform the benchmark case presented by Myhre et al. (2009). The parameters defined for the computation are listed in Table 1-3.

Table 1-3: Configuration of the parameters of the radiative forcing presented by Myrhe et al., 2009.

Observation altitude	13 km
Atmosphere	AFRL Summer
Solar zenith angle	30 °, 60 °, 75 °
Ground albedo	0.2
Cirrus optical thickness	0.3
Cirrus albedo (visible / IR)	1 / 0.6
G (asymmetry factor)	0.8
Height of the cirrus	10 – 11 km

The results are displayed in Figure 1-29. In addition, outputs from the ONERA three-dimensional model ASTRE are also included. As a reminder, SW and LW cloud radiative effects are computed as the difference between cloud-free and cloudy sky fluxes and the net effect is calculated as SW + LW. Positive net balance leads to a warming. For the solar zenith angle of 30 °, MATISSE and ASTRE results are consistent with the benchmark. At SZA = 60 °, the benchmark provides both warming and cooling effects. MATISSE results show a warming whereas ASTRE provides a cooling effect. Finally, both display a cooling effect for SZA = 75 °.

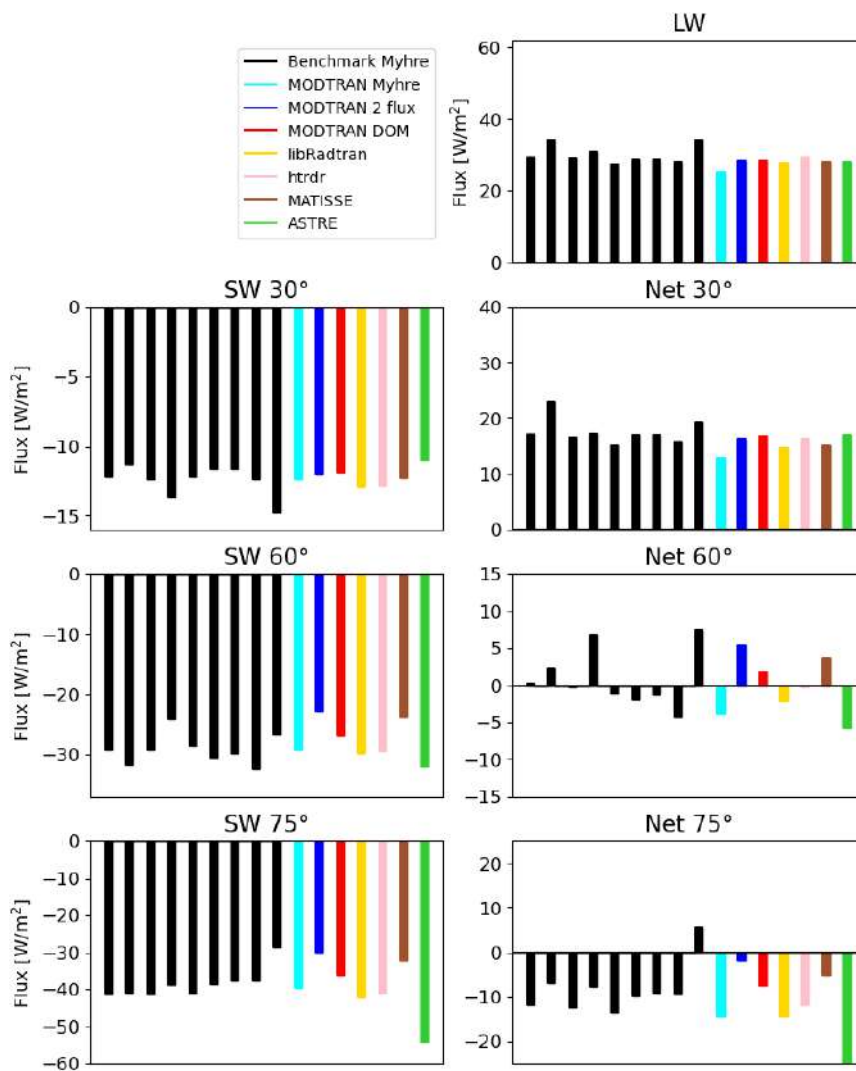


Figure 1-29: Benchmark of various radiative transfer models and computations performed within the frame of this study (ModTRAN, libRadTran, htrdr, MATISSE and ASTRE), compared with Myhre benchmarks in black. MATISSE and ASTRE are new additions this year.

The next steps are dedicated to a sensitivity study of the various parameters using MATISSE. In particular, the cirrus characteristics will be adjusted to contrail parameters. For example, the range of effective radii, IWC, albedo, etc will be extracted from observational data (Schumann et al., 2017, Wolf et al., 2023). These values will allow to display the range of SW and LW fluxes associated and assess the impact of contrails on radiative forcing.

In parallel, work has been performed with the ASTRE solver, which was adapted to the calculation of contrail radiative forcing (RF) and a first application was performed. A full sensitivity study was performed during the fourth year of Climaviation to compare to the literature (libradtran results by Wolf et al., 2024). The results are shown in Figure 1-30 for both LW and SW spectra. LW radiative forcings are positive, the contrail is indeed warming in the LW band, while it is cooling in SW, SW radiative forcings being negative. For each of the parameters, the value for which the LW radiative forcing is maximum is the same that maximises SW radiative forcing (in absolute value). Between the two solvers, a main difference appears for the reference radiative forcings, but the ranges are substantially the same. With the chosen reference parameters and the given value ranges, it may be interesting to classify the quantities which most influence the radiative impact of the contrail.

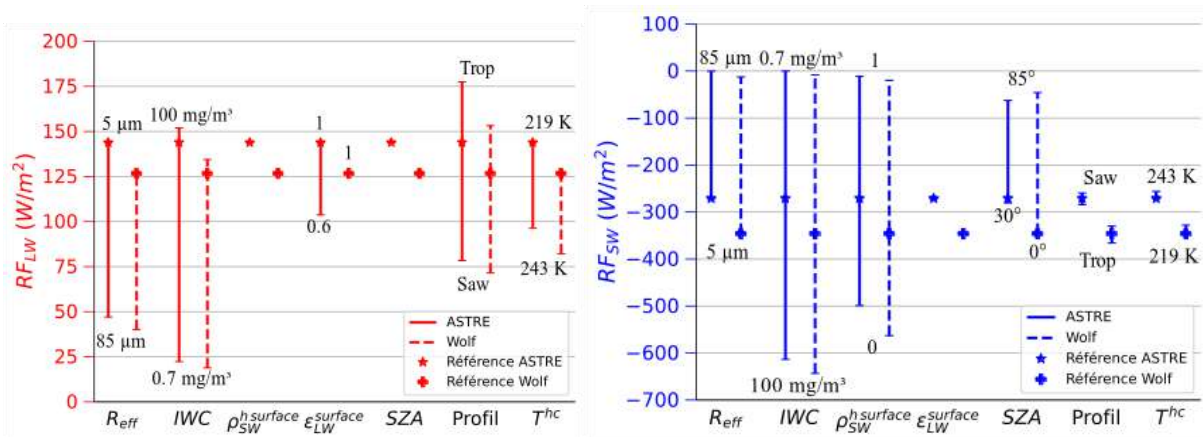


Figure 1-30: Comparison of the influence of the different parameters tested on the calculation of the LW and SW RF. Each vertical bar corresponds to the range of the associated radiative forcing values; the minimum and maximum values of the RF are indicated on either side of the vertical bar. The ASTRE results are in solid lines, those obtained by Wolf et al. (2024) using libradtran in dotted lines; the reference value is indicated by a star (ASTRE) or a plus sign (Wolf et al., 2024). “Saw” and “Trop” designate the Subarctic winter and Tropical profiles, respectively

Thus, in the LW, RF is most sensitive to ice water content, followed by crystal radius and the choice of atmospheric profile. As for the temperature at the top of the contrail and the LW emissivity of the ground, the extent of LW radiative forcing is halved compared to the other parameters. In the SW, radiative forcing is primarily driven by the ice water content, followed by the SW albedo of the ground, as well as the ice particle radius and the solar zenith angle. The atmospheric profile and the temperature at the top of the contrail have no impact on RF_{SW}.

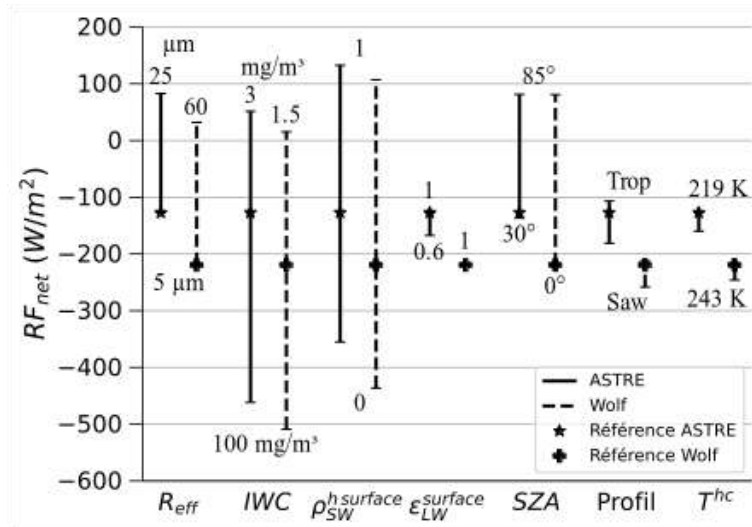


Figure 1-31: Comparison of the individual influence of each of the tested parameters on the net radiative forcing.

By summing the LW and SW contributions, the same figure can be produced for the net radiative forcing (Figure 1-31). The net RF takes positive and negative values, and its value is mainly dictated by four parameters, which are in decreasing order of influence: ice water content, surface SW albedo, solar zenith angle (SZA) and effective radius. Then, on the other hand, the choice of atmospheric profile, LW emissivity of the ground and temperature at the top of the contrail have very little influence on net radiative forcing. With the chosen reference properties, the radiative forcing is in absolute value larger in SW than in LW, explaining that the net RF is negative in many tested cases.

In the 1D configuration studied previously, the contrail is "infinite" along the x and y directions, so it occupies the entire length and width of the box. The decomposition into four calculations then involved two calculations without a contrail and two calculations with a contrail that covers the entire domain. This is what the literature calls the "independent column approximation". By performing two calculations with 0 % coverage and two others with 100 % coverage, there is no horizontal interaction between the contrail and the atmosphere; we neglect, in fact, the transport of photons on the sides of the contrail. In this section, the 3D effects occurring are presented using a new 2D configuration of ASTRE solver developed in the fourth year of the project.

The study conducted consists of comparing the results of a 1D case with a 2D configuration for which the Sun is parallel or perpendicular to the infinite length of the contrail. The zenith angle thus varies from 0° to 89° (Figure 1-32).

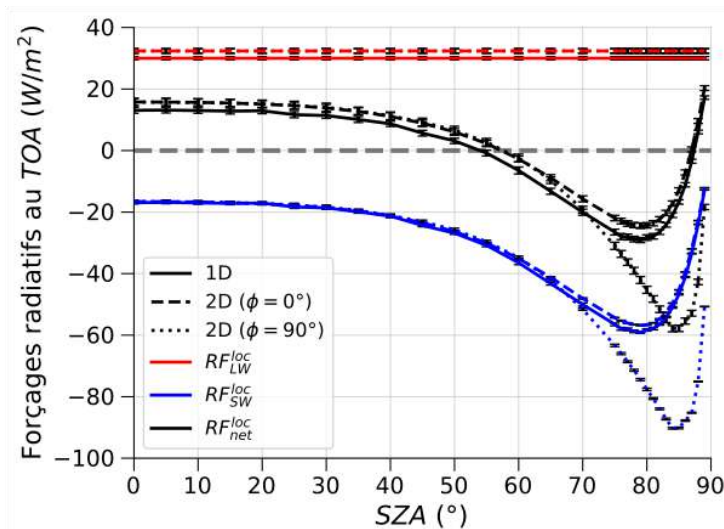


Figure 1-32: Influence of the solar zenith angle on radiative forcing and comparison between a 1D and 2D case. For the 2D configuration, two azimuthal angles are tested; the standard deviation is indicated for each value with ASTRE.

The absolute deviations observed in the net local radiative forcing are quite small up to $SZA = 60^\circ$, but the relative deviations are not negligible. For example, at the zenith, net local RF local in 1D is 13.1 W/m^2 and 15.8 W/m^2 in 2D, an increase of 21 %. At an $SZA = 60^\circ$, the relative deviation reaches -60% , although the absolute deviation is only 4 W/m^2 : this is explained by the low value of the net local radiative forcing at this zenith angle. Then, if the azimuthal angle $\phi = 0^\circ$, the absolute deviation remains constant around 4 W/m^2 and then decreases from $SZA = 79^\circ$. Net local RF becomes positive again at $SZA = 88^\circ$. For $\phi = 90^\circ$, the net local radiative forcing follows the SW curve, but remains negative even for very high zenith angles.

The contrail characteristics evolve during its formation, notably its optical thickness and its morphology. In addition, a 2D contrail offers the advantage of being able to vary two dimensions, namely its thickness and its width. For a zero solar zenith angle, we study the influence of the thickness e and the width l on the radiative forcing of an isolated contrail: $e \in \{0.25, 0.5, 1\} \text{ km}$ and $l \in \{1, 2, 4\} \text{ km}$. Optical thickness takes four different values: Optical depth (OD) at $0.55 \mu\text{m} \in \{0.25, 0.5, 1, 2\}$, i.e. a total of 36 different contrails. Maintaining the same crystal size distribution, the optical thickness is directly proportional to the product $IWC \times \text{contrail depth}$, often denoted as IWP for "Ice Water Path". Thus, for a chosen pair (e.g. OD at $0.55 \mu\text{m}$), the IWC will be adapted accordingly. To characterize the morphology of the contrail, the aspect ratio is introduced: $r = e/l$. Since width is always greater than thickness, the aspect ratio is less than or equal to 1.

Figure 1-33 shows the RF sensitivity to both its OD and its aspect ratio. For an OD (550 nm) = 2, the net radiative forcings are negative for all morphologies except if the contrail width is equal to its thickness, in which case the contrail is heating. Moreover, the shape of the nine curves is identical, increasing as a function of optical thickness up to a maximum, before decreasing. The optical thickness that maximizes the net local radiative forcing is however not the same depending on the morphologies. If $r \geq 1/2$, the maximum is reached at OD (550 nm) = 1, while an optical thickness of 0.5 allows maximizing RF local when $r < 1/2$. Finally, in both LW and SW, a fluctuation in optical thickness led to greater variations in local radiative forcing than a change in aspect ratio.

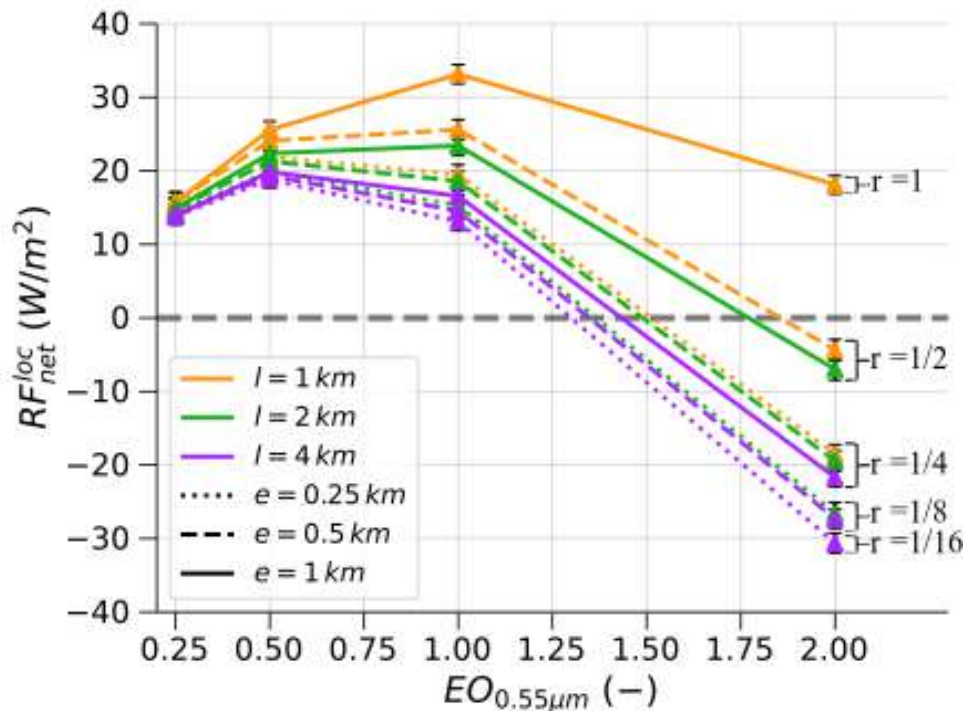


Figure 1-33: Evolution of net radiative forcing according to optical thickness at $0.55 \mu\text{m}$ and contrail width l , geometric thickness e , and aspect ratio r .

Further short-term developments have been identified during the fourth year of Climaviation. In the SW, atmospheric Rayleigh scattering and ozone absorption must be taken into account, while in the LW, the influence of methane, nitrous oxide, and ozone must be studied to determine the need to add them to the atmospheric composition represented in ASTRE. Furthermore, it would be interesting to add the possibility of working with non-spherical ice crystals, for example by reading the radiative properties used by libRadtran. Furthermore, the size distribution of ice crystals is currently Gaussian, but measurement campaigns tend to indicate lognormal distributions, which could be introduced into ASTRE. Moreover, only uniform contrails were studied. However, the contrail exhibits vertical and horizontal heterogeneity, which can for example be taken into account in the solver by spatially parameterizing the mean particle size distribution and the IWC.

1.6.2. Integration of three-dimensional radiative effects

Contributor: Julie Carles, Jean-Louis Dufresne, and Nicolas Bellouin (IPSL)

The cloud radiative effect (CRE) and 3D effects (difference between 3D and 1D radiative transfer calculations) of an idealised contrail has been integrated on selected days and latitudes: summer and winter solstices and equinoxes, at 45° and 60° latitude. The contrail has a width of 1 km and geometrical thickness of 500 meters. Three cloud optical depths are studied, 0.25, 1 and 4. Figure 1-34 shows that shortwave 3D effects averaged over daytime increase in magnitude with increasing optical depth, latitude and from summer solstice, to equinoxes, to winter solstice. Thus, the largest 3D effects are observed at winter solstice at latitude 60 degrees. In addition to the dependence on cloud optical depth, day of the year and latitude, 3D effects also exhibit a dependence on contrail orientation relative to the Sun. Two situations are studied: one with the cloud aligned in a south-north (SN) direction, the other in a west-east (WE) direction. Clouds most often oriented perpendicularly to the Sun rays show stronger 3D effects. This leads to a contrast between 3D effects of the

two orientations according to the seasons: at 60° of latitude, during the equinox, the SN cloud shows the largest 3D effects, whereas in winter it is the WE cloud. Shortwave 3D effects are negative in most of the studied cases, but adding the longwave 3D effects can result in positive net 3D effects.

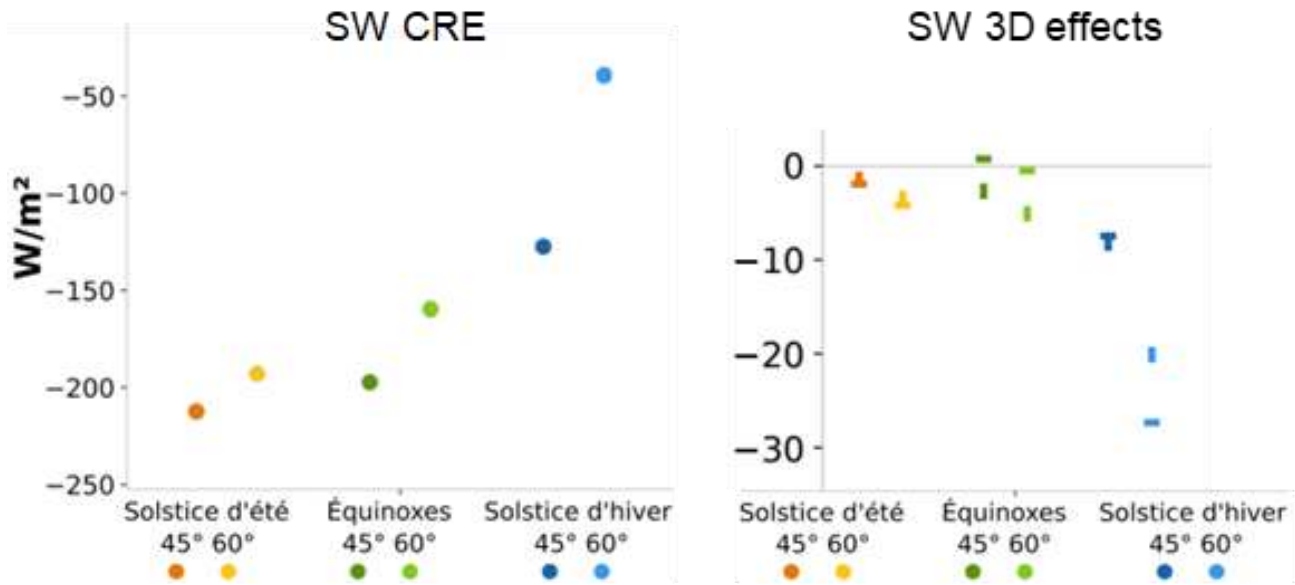


Figure 1-34: Mean SW daytime and 3D effects, in $W m^{-2}$, for selected days, latitudes and cloud orientations. Dots denote the 1D calculations and dashes the 3D calculations: horizontal (vertical) dashes are for WE (SN) oriented clouds. Cloud optical depth is 0.25. From left to right the colours correspond to summer solstice, equinox and winter solstice, dark colours for 45 degrees latitude and lighter colours for 60 degrees latitude. The calculations are for a rectangular cloud with 1000 meters width and 500 meters height.

Then, the CRE and 3D effects for a 10 km wide and 800 m thick contrail of optical depth 0.25 have been calculated along three transatlantic flight trajectories. Results are shown in Figure 1-35. The atmosphere (a Mid Latitude Summer profile) and contrail properties are kept constant: the integration simply follows the plane along the trajectories. Once again, a strong impact of the season is found because of very different solar angle distributions. Two similar trajectories, in September and January, result in net CRE and 3D effects of opposite sign due to different solar positions: the September flight leads to warming net CRE and 3D effects while the January flight leads to cooling CRE and 3D effects. The net 3D effects are often several tens of per cent of the 1D calculations. These preliminary results highlight the significant role of solar position, via both zenith and absolute azimuth angle formed between the contrail and the Sun, in the resulting sign and magnitude of CRE and 3D effects of radiation.

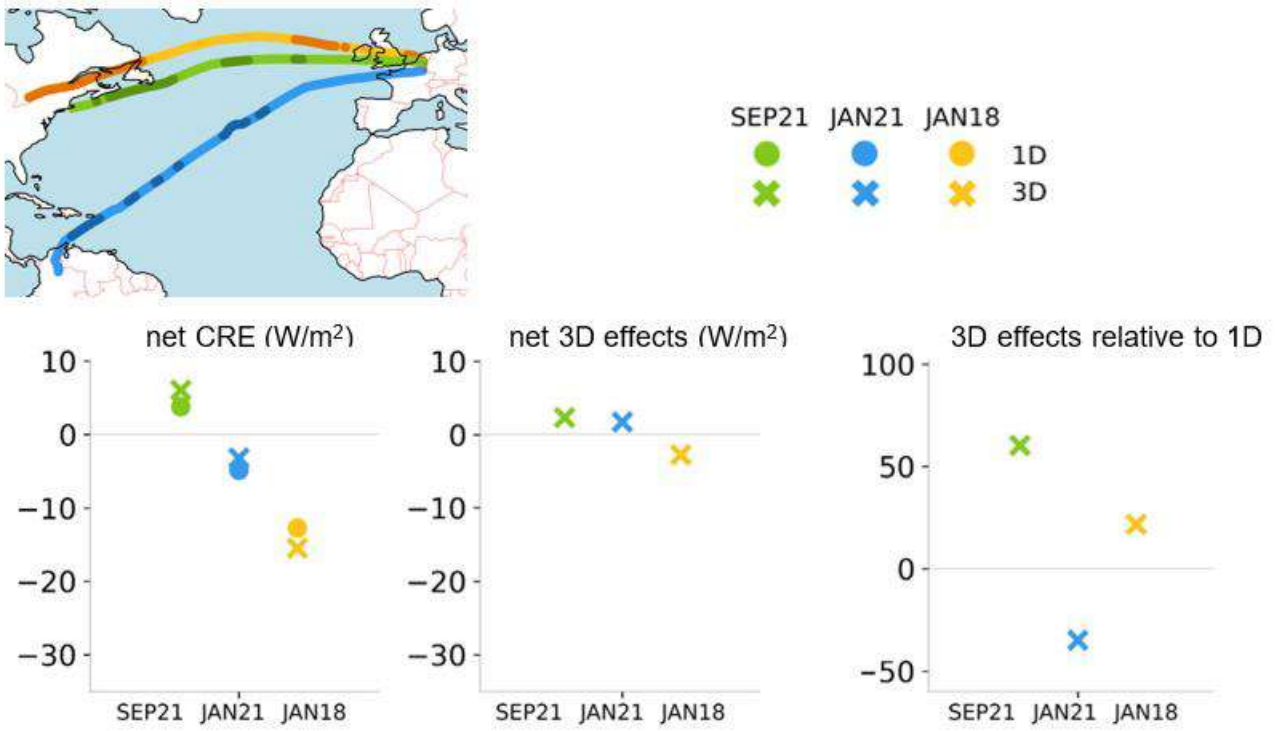


Figure 1-35: Mean net CRE and 3D effects for three trajectories. Dots denote the 1D calculations and crosses the 3D calculations. In all cases, the contrail optical depth is 0.25, for a rectangular contrail with 10,000 m width and 800 m height.

2. AXIS 2: ATMOSPHERIC CHEMISTRY

The objective of this axis of research is to study the chemical mechanisms that occur in the upper atmosphere and involve aircraft engine emissions. Particular attention is paid to the impact of NO_x on ozone and aerosols.

2.1. WP 2.1: Effective NO_x emission index

Contributors: Etienne Terrenoire (ONERA), Didier Hauglustaine (IPSL)

The objective of this work package is to calculate the chemical evolution of engine emissions (NO_x, SO₂, sulphate, nitrate) in the plume downstream of the aircraft to provide climate models with inputs relevant to climate scales. This will improve the accuracy of large-scale chemical mechanism assessments.

The selected approach follows the two-step approach described in Cariolle et al. (2009). During the fourth year of the project, the first step of the Cariolle et al. (2009) approach described in the third-year annual report of the project was applied to a set of 200 real trajectories taken from the North America air traffic on 1 July 2019. To do so, the plume cross-section and the associated dilution were calculated using pycontrails software (pycontrails, 2025) following the logic described in Figure 2-1.

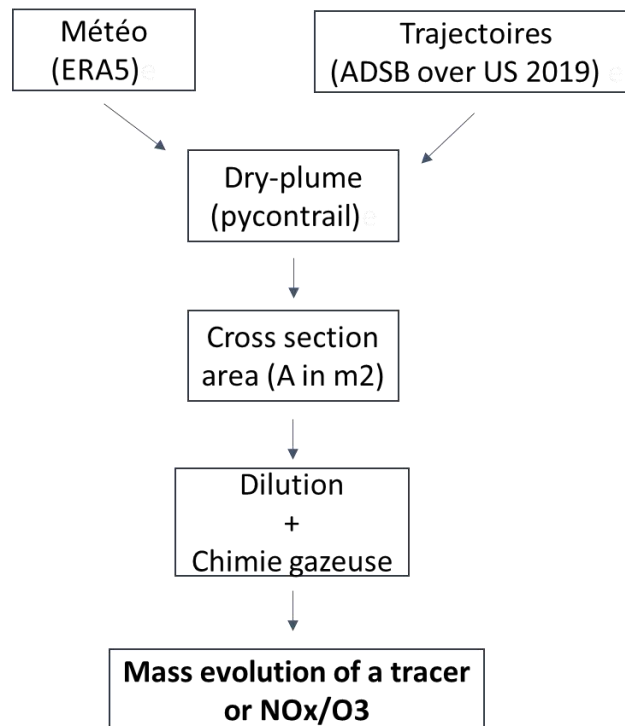


Figure 2-1: Methodology used to calculate the mass time evolution of a given chemical species within the plume.

First, the work for step 1 consisted of determining using pycontrails (pycontrails, 2025) the volume of the plume for each waypoint of all trajectories (dilution). Main inputs to pycontrails include real aircraft trajectories and meteorological data at the plume locations. Figure 2-2 shows, as an example, the plume cross section evolution, for a mean of trajectories representative of 6 aircrafts types. That evolution is used as an input for step 2.

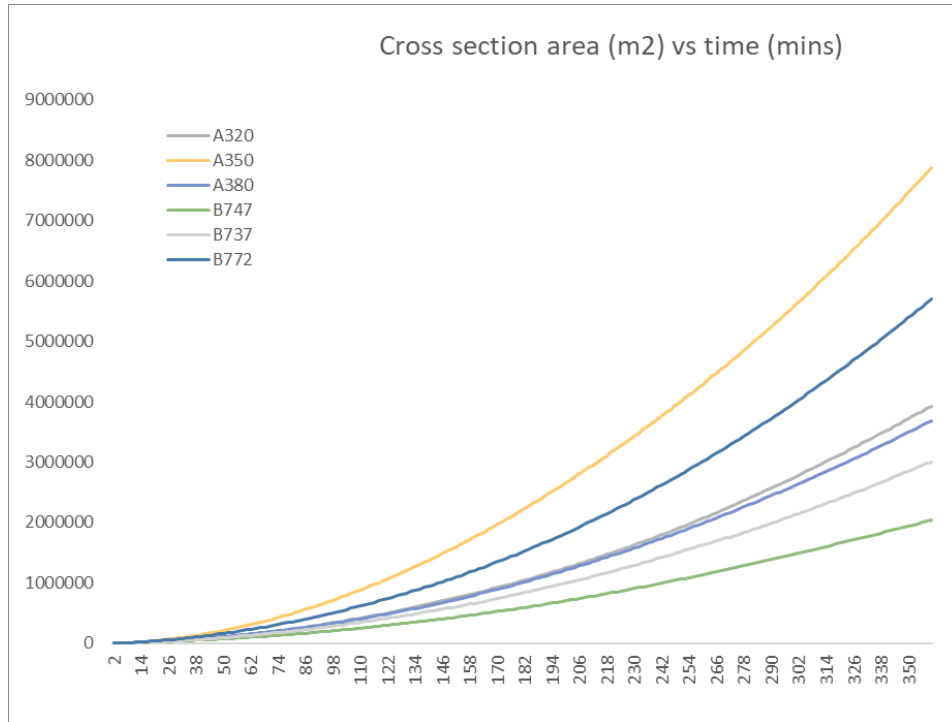


Figure 2-2: Evolution over time of selected aircraft engine plume cross section, in m².

Then the mass evolution of a given species is calculated as Petry et al. (1998):

$$C_i(t+\Delta t) = \frac{A(t+\Delta t) - A(t)}{A(t+\Delta t)} C_i^b(t+\Delta t) + \frac{A(t)}{A(t+\Delta t)} C_i^p(t+\Delta t)$$

where A is the time evolving plume sectional area, C_i is the concentration of species i in the grid-cell, C_i^b the background concentration and C_i^p the concentration within the plume. The final step of step 1 is to determine the coefficient τ (the decay time of the tracer concentration evolution) to approximate the decay of a tracer as described in the following equation approximating $M(t)$, the mass of the tracer in the plume, by an exponential function whose time integral is the same as the exact mass integral over the plume total duration (T_i):

$$\tau \equiv \int_{t_0}^{+\infty} \exp\left(\frac{-t}{\tau}\right) dt = \frac{1}{M(t_0)} \int_{t_0=0}^{T_i} M(t) dt$$

Figure 2-3 shows the mass time evolution of a passive tracer for two dilution magnitude for the same aircraft (A320):

- Case 1 is representative of a strong dilution (blue) corresponding to a $\tau = 8$ h
- Case 2 is representative of a weak dilution (orange) corresponding to a $\tau = 11$ h

It clearly shows that the dilution can vary for a given aircraft as the local meteorology where the plume evolves is a key driver for dilution. Overall, the value of τ that is calculated with this approach (8 - 10 hours) is lower than the one modelled by Cariolle et al. (2009), which was estimated to be 15.9 hours.

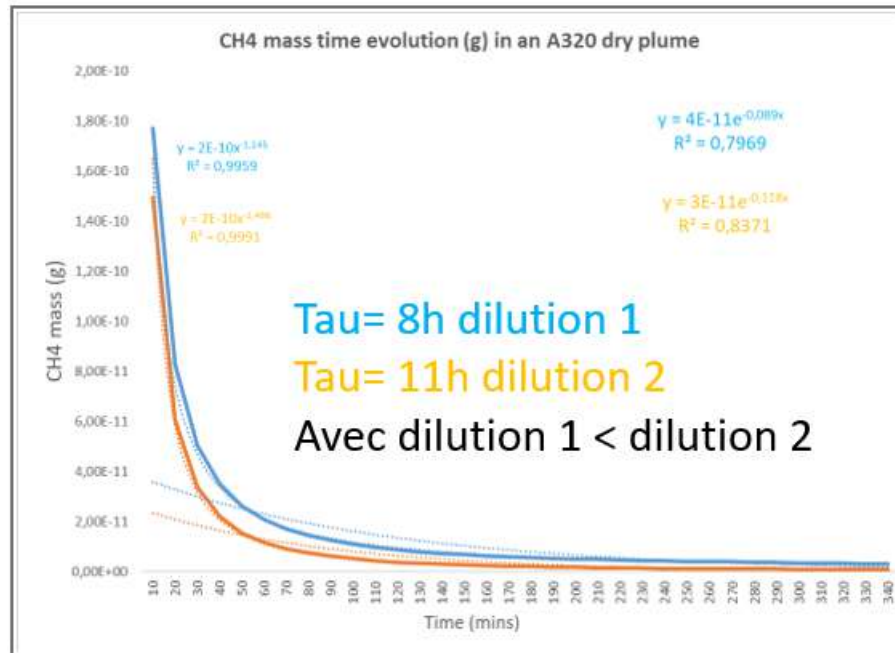


Figure 2-3: Mass time evolution of a passive tracer (in g) for two types of dilution (weak as dilution 1 and strong as dilution 2).

The second step of the Cariolle et al. (2009) approach dedicated to the calculation of NO_x/O₃ contains in the aircraft plume using the INCA 0D chemical model (Hauglustaine et al., 2004) is currently ongoing. The results for step 1 are still under analysis and will be presented next year in the final report of Climaviation.

2.2. WP 2.2: Improvement of LMDZ-INCA

Contributors: Didier Hauglustaine, Yann Cohen, Nicolas F evrier (IPSL)

The objective of the work package is to implement a new version of the LMDZ-INCA global model, more complete and including the parameterization of the chemistry in the plumes to better quantify the NO_x forcing.

Previous aviation impact results (e.g., Terrenoire et al., 2022; contribution to the ACACIA project) have been obtained with the LMDZ v6-INCA v6 version of the model including 39 vertical levels and the former LMDZ parameterizations for convection and boundary layer mixing. We are progressively switching to the version 7 of INCA coupled to the version of LMDZ including 79 levels and the latest parameterizations for convection, boundary layer mixing and the RRTM radiative transfer model. We previously mentioned we assessed the results for these 2 versions of the model at aircraft flight altitudes using measurements routinely carried out on board airliners by the IAGOS programme. These measurements have already enabled us to assess ozone, carbon monoxide, water vapour and NO_y (total nitrogen). This work was carried out using the 39-level vertical version of the LMDZ-INCA model, as well as the 79-level version and new physics of the LMDZ model. This evaluation showed the need to review the treatment of NO_x emissions by lightning in tropical regions. Indeed, with the modified convection scheme in the CMIP6 version of LMDZ, convective clouds appear at a significantly higher altitude in the tropics, leading to excessive NO_x emissions from lightning. Using flashes of lightning measured by the OTD and LIS satellite instruments, we can now constrain and correct this major source of nitrogen oxides in the upper troposphere.

In addition to this work on this new version of the model, we will also continue to improve the scavenging of soluble species and aerosols in the model. Several scavenging parameterisations are being compared and evaluated based on the ATOM measurement campaigns. The impact of the scavenging scheme on the atmospheric response to aviation emissions are being analysed as part of Nicolas Février's thesis (2022-2025). This work will enable us to understand whether the parameterisation of scavenging is a major source of uncertainty and to what extent it can explain some of the differences obtained between the different models for HNO₃ and aerosols (BC, SO₄). In addition, as part of this thesis, we will also study the role of redistribution of in-flight emissions towards the surface and how in-flight aviation emissions are then transported towards the boundary layer to participate in the degradation of air quality and interact with aerosols and low clouds or, conversely, how they are transported towards the stratosphere.

It is often written, and rightly so, that the chemistry of ozone and nitrogen oxides in the troposphere is highly non-linear. This is particularly true of surface emissions of ozone precursors. Studies of the impact of surface emissions on air quality therefore need to take account of this problem when attributing disturbances to a specific sector. In the case of emissions at altitude (from aviation in particular), this non-linear nature needs to be analysed using a series of simulations of disturbances of different amplitudes. Analysis of the results obtained for perturbations in NO_x emissions from aviation of 100%, 50%, 20% and 5% will enable us to assess the extent of this non-linearity. It may be necessary in the future to consider developing another method (e.g. by marking) to determine the impact of aviation on ozone and its radiative forcing.

2.3. WP 2.3: Impact of NO_x emissions on ozone and oxidising capacity

The objective of this work package is to evaluate the atmospheric chemistry simulations by the LMDZ-INCA model with the IAGOS database, to identify improvements that can be made on the existing emissions and/or parameterizations, and to use the new version of the model to evaluate the impact of aviation emissions.

A modelling experiment done as part of the EU-funded ACACIA project has involved five global chemistry-climate models (CCMs) or chemistry-transport models (CTMs): EMAC, LMDZ-INCA, MOZART3, OsloCTM3, UKESM1.1. Another model has been incorporated into the experiment, though with a slightly different simulation setup (as the runs were made independently of our experiment). In a first step, an assessment of the model daily output on a (bi-)decadal timescale in the upper troposphere – lower stratosphere (UTLS) is based on the airborne IAGOS observations in ozone, carbon monoxide (CO), water vapour (H₂O_v), and reactive nitrogen species (NO_y, which comprises mainly NO_x, nitric acid – HNO₃, and peroxyacetyl nitrate – PAN in this region). Following the methodology described in Cohen et al. (2021) and Cohen et al. (2023), the separation between upper troposphere (UT) and lowermost stratosphere (LS) was made possible using the model Ertel potential vorticity (PV), provided by the models EMAC, LMDZ-INCA, OsloCTM3, and UKESM1.1. The tropopause definition is chosen as the 2 PVU isosurface. In a second step, an analysis of the model sensitivities to aviation NO_x emissions is based on a set of present-day runs (2014 – 2018) for five of the models (EMAC, LMDZ-INCA, MOZART3, OsloCTM3, and GEOS-Chem), including a run without aviation emissions, a run with 20% less aviation emissions and, when possible, a run without NO_x emissions only.

The model assessment using IAGOS has been recently accepted (Cohen et al., 2025). It highlights that the models reproduce realistically the seasonal specificities linked to the effects of the photochemical activity and of the Brewer-Dobson circulation on ozone and NO_y, in the UT and LS respectively. In the UT however, most models show a positive ozone bias, and the relative differences between the models are important, with more

ozone with EMAC and less ozone seen by LMDZ-INCA, as for NO_x (which suggests that the mean NO_x concentrations are the main factor controlling the ozone amounts in the UT). As for ozone and NO_y, the other species show a similar seasonal behaviour between the models, though with different amounts. The summertime maximum in H₂O_v for both layers shows the effects of convection in the UT, and of turbulent mixing with the UT in the LS. Among the models, EMAC shows less H₂O_v in the UT and more in the LS, which suggests an overestimated turbulent mixing between the two layers. UKESM1.1 also underestimates H₂O_v in the UT, as well as in the LS, rather suggesting a lack of uplifted water vapour from the lower troposphere. Concerning CO, a summertime maximum in the LS is visible in the observations as in the models, but the models do not reproduce the observed springtime maximum in the UT. It may reflect an underestimated convection during this season, an overestimated CO sink in the lower troposphere in winter, or an underestimated secondary CO production.

The impact of the aviation NO_x emissions in the UTLS as seen by the models is represented in Figure 2-4 and 2-5, for NO_x and ozone, during the months that minimize (January) and maximize (April, May, or June depending on the model) the ozone perturbation. For this experiment, five models have their output available: EMAC, GEOS-Chem, LMDZ-INCA, MOZART3, and OsloCTM3. As expected, the NO_x perturbation peaks in the northern mid-latitudes, as the emissions are the most important above North America, Europe and the Atlantic corridor (not shown). The NO_x perturbation is confined into the midlatitudes during winter as the NO_x are mostly converted into nitric acid (HNO₃) before reaching the higher latitudes, and spreads toward the pole in spring-summer. It is generally stronger with the OsloCTM3 model and weaker with GEOS-Chem. Concerning ozone, the mean perturbation is more homogenized compared to NO_x, which can be expected from a secondary pollutant as its formation can take place days or weeks after the NO_x emission. The ozone perturbation is stronger in spring-summer compared to January, which is also expected as the sunlight is more abundant and mainly takes place in the lowermost stratosphere (LS). The fact that the ozone perturbation generally reaches its maximum before summer can be due to the higher tropopause levels, which causes a greater proportion of NO_x emitted in the troposphere, thus increasing ozone tropospheric production (thus reducing the lower-stratospheric ozone loss by mixing). Further investigation using ancillary variables in EMAC and LMDZ-INCA showed that ozone loss decreases in the LS as well as OH mixing ratio in this layer, thus contributing to this ozone perturbation maximum.

Similar analysis has been performed for the year 2050 based on different scenarios. In these simulations under analysis the impact of aircraft emissions on atmospheric composition are calculated as a function of the background atmosphere and (surface) emissions from other sectors. The idea being these simulations is to determine whether the net response to NO_x emissions can switch from being a positive forcing dominated by the ozone effect to a negative forcing dominated by the methane effect. These results will be presented next year in the final Climaviation report.

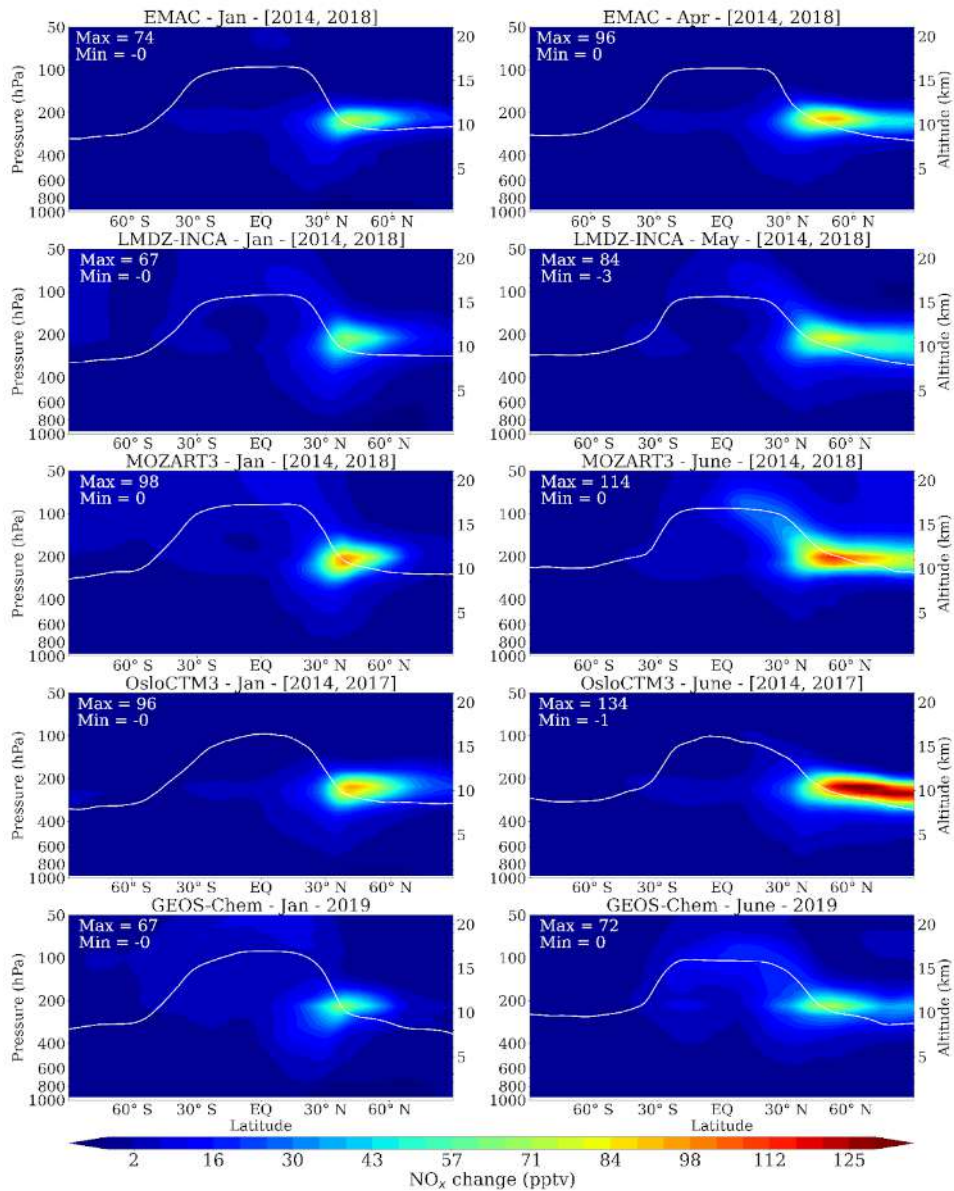


Figure 2-4: Zonal cross sections showing the NO_x perturbation due to aircraft emissions, for the five models (from top to bottom) and for the months minimising and maximising the ozone perturbation (from left to right). These months and the years considered are shown in the panel titles with the model names.

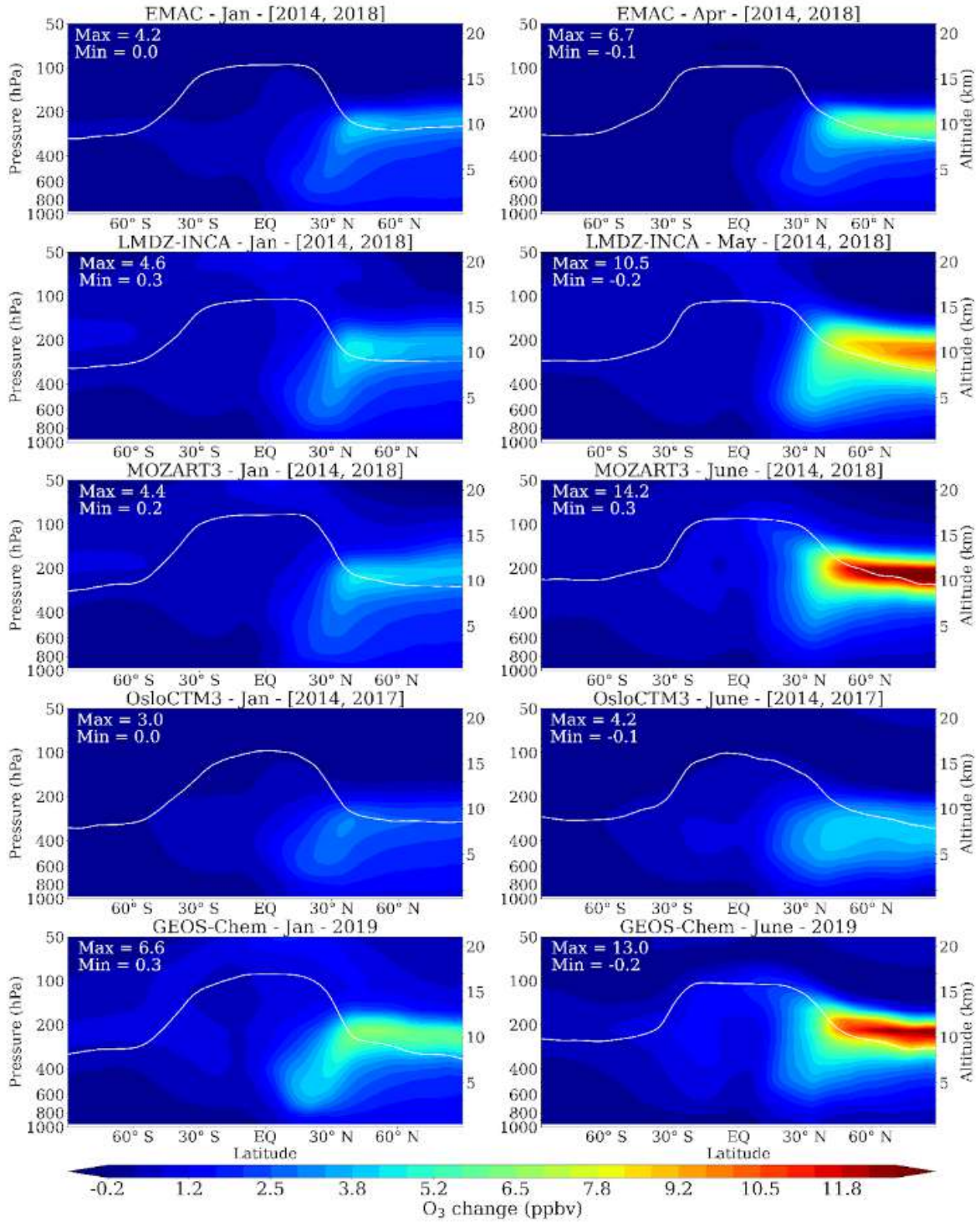


Figure 2-5: As Figure 2-4, but for the ozone perturbation.

2.4. WP 2.4: Impact of NOx emissions on methane

The objective of this work package is to simulate the response of methane to aviation emissions and in particular its residence time to aviation emissions and to estimate the indirect perturbations (O₃, H₂O).

The results presented in Section 2.3 for the different models and for the present-day aircraft perturbations have been used to calculate the radiative forcing of climate change by ozone and methane. Figure 2-6 and Figure 2-7 show the effective radiative forcings from aviation-induced species, respectively gaseous and particulate, calculated by our colleagues from CICERO (Oslo, Norway). The net impact on gaseous chemistry (ozone + methane forcings associated with the NOx emissions) is in relative agreement between the models, ranging between +7 and +22 mW m⁻². For the present-day, note that this net forcing is positive among all participating models. The aerosol impact ranges between -6 and -18 mW m⁻², with important differences between the models for each species (e.g. nitrate forcing can vary by a factor 6 between two models). These results show that the total aerosol direct forcing is subject to a large variation among the models and uncertainty. This forcing is however negative for all models and dominates the total forcing associated with gaseous and aerosol emissions. This of course excludes the indirect effects of aerosols investigated in Climaviation Axis 3.

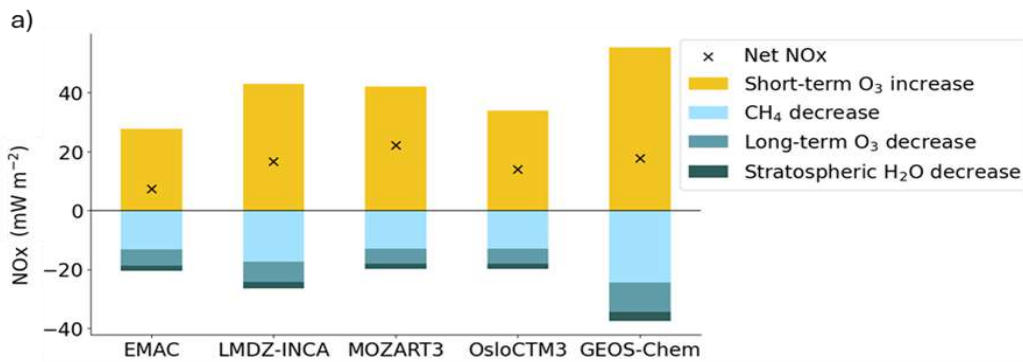


Figure 2-6: Effective radiative forcings (ERF, in mW.m⁻²) linked to the impact of NOx emissions on gaseous species.

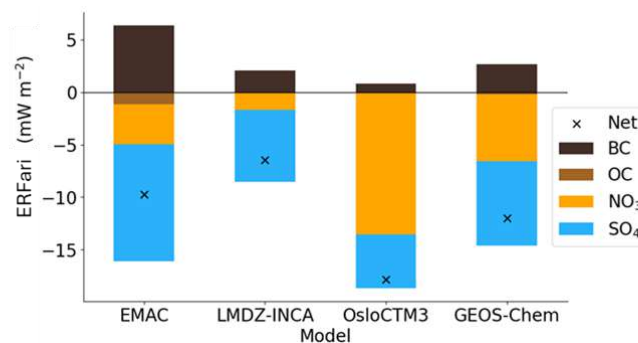


Figure 2-7: Radiative forcing caused by aviation-induced aerosols, for the models that include aerosols.

In addition to investigating the radiative forcings associated with 2050 perturbations, as part of the British Natural Environment Research Council (NERC) CRANE project, in which we are part in collaboration with the Universities of Reading and Manchester, we will attempt to go beyond the simple radiative forcing of ozone by calculating the climatic response associated with an idealised ozone perturbation associated with

NO_x from aviation and by comparing the results of the UKESM and the coupled IPSL model to determine the efficacy of the ozone perturbation from aviation NO_x emissions.

3. AXIS 3: IMPACT OF AEROSOLS ON NATURAL CLOUDS

The objective of the third axis of research is to investigate the mechanisms by which aerosol emissions from aircraft modify the formation and evolution of liquid and ice clouds, and to quantify the resulting radiative forcing.

3.1. WP 3.1: Competition with background aerosols

The objective of this work package is to understand, model, and predict the competition between aerosols emitted by aviation and pre-existing aerosols in the atmosphere in terms of their contribution to the populations of condensation nuclei and ice nuclei. This work is described in Section 3.3.

3.2. WP 3.2: Aerosol transport from aviation

Contributors: Nicolas Février, Didier Hauglustaine, Nicolas Bellouin (IPSL)

The objective of this work package is to understand, model, and quantify the time scales that govern the horizontal and vertical transport of aerosols from aviation.

This work uses the LMDZ-OR-INCA model, which couples the LMDZ atmospheric model with the INCA tropospheric chemistry model and the ORCHIDEE land surface model. LMDZ (see for example Boucher et al., 2020) uses 79 sigma-pressure levels as vertical coordinate; the highest level is at about 80 km – around the mesopause. The horizontal resolution is 144×142 grid-cells on a staggered latitude-longitude Arakawa C-grid. For the present work, the model winds are nudged towards the ECMWF reanalysis with a relaxation time of 2.5 hours.

LMDZ calls INCA with a 30-minute timestep. INCA simulates homogeneous and heterogeneous chemical reactions and accounts for surface and atmospheric emissions, including for NO_x generated by lightning, calculates dry and wet deposition and solves photo-chemical reactions (Hauglustaine et al., 2004). INCA also applies ageing to Black Carbon (BC, or soot): insoluble BC is converted into soluble BC at a rate proportional to OH concentration. Consequently, BC ages faster during daytime and summer.

Previously, this work was focused on transport and scavenging of BC aerosols. A realistic parameterisation of wet scavenging is crucial because about 70% of total BC is removed from the atmosphere through scavenging and because adjusting scavenging in climate models improves BC concentrations (Lund et al., 2018; Gao et al. 2022). Now, sulfate and nitrate aerosols have been added to the study. BC is a primary aerosol: it is directly emitted from aircraft engines, while sulfate and nitrate are secondary aerosol: they are the product of the oxidation of sulfur dioxide and NO_x respectively, which are emitted by aircraft engines.

Three LMDZ-INCA scavenging parameterizations have been compared:

- Wetdep: INCA's default routine for BC.
- Sethet: INCA's routine for species that undergo heterogeneous chemistry (especially HNO₃, SO₄ and NO₃).
- Scav: LMDZ's routine, used when LMDZ is run without INCA. Some bug corrections were implemented in this code in the context of this work.

Table 3-1 summarises the differences among these parameterizations.

Table 3-1: Description of the three routines used to simulate wet scavenging of black carbon aerosols in LMDZ-INCA in this work.

Routine	Stratiform scavenging level of detail	Convective scavenging level of detail	Reevaporation represented
Wetdep	- In-cloud: \propto precipitations - Below-cloud: first-order loss equation	Shallow vs deep convection	No
Sethet	Falling raindrop-model HNO ₃ used as reference	Continuous function of the height of the convective system	No
Scav	First-order loss equations (both in and below-cloud)	Three terms: - adiabatic ascent - mixtures - environment	Yes

In this work, for each of the three scavenging routines, four 3-month long simulations have been run, during different periods of the year. The data shown in the following corresponds to the last month of simulation. These last months are January, May, August and October. We show here the results for January and May.

Figures 3-1 and 3-2 show the zonal mean aviation perturbation for BC, sulfate and nitrate aerosols in January and May, respectively, for each of the three scavenging routines. As found in previous studies (Terrenoire et al. 2022), the aviation aerosols emitted at cruise level (~250 hPa) in the Upper Troposphere-Lower Stratosphere (UTLS) are caught in the descending branch of the general circulation between the Hadley and the Ferrel cells, between 30°N and 45°N. Also as expected, the aviation nitrate perturbation is negative at cruise levels, due to the competition with sulfate. The sulfate and nitrate perturbations are significantly stronger in May than in January because the atmosphere is more oxidising in May because of higher solar irradiation. For Sethet, positive and negative aviation nitrate perturbations are multiplied by 4.1 and 3.7 from January to May, respectively.

An unexpected result is that the choice of scavenging parameterisation has a strong impact on aviation perturbations in the UTLS, despite precipitations being very rare in this region. That is explained by the fact that aerosols have very weak sinks in the UTLS, especially aviation aerosols which are in the accumulation mode, for which sedimentation is negligible. Consequently, the weak but non-zero precipitation rates in the UTLS combined with modified scavenging rates depending on the scavenging scheme lead to sizeable changes. The general result is that Sethet yields the strongest aviation impact, followed by Wetdep then Scav.

In May (Figure 3-2), the maximal BC perturbation is 4% and 20% weaker when switching from Sethet to Wetdep and Scav, respectively. For sulfate aerosol, the numbers are 10% and 26%. For nitrates, the maximal negative perturbation decreases by 5% and 35% and the maximal positive perturbation by 42% and 73%, respectively. The higher sensitivity of sulfate and nitrate to the scavenging parameterization compared to BC is related to their solubility. Sulfate and nitrate become soluble, and hence subject to wet scavenging, as soon as they are chemically formed, whereas 80% of aviation primary BC is emitted as insoluble before ageing and becoming soluble through coating.

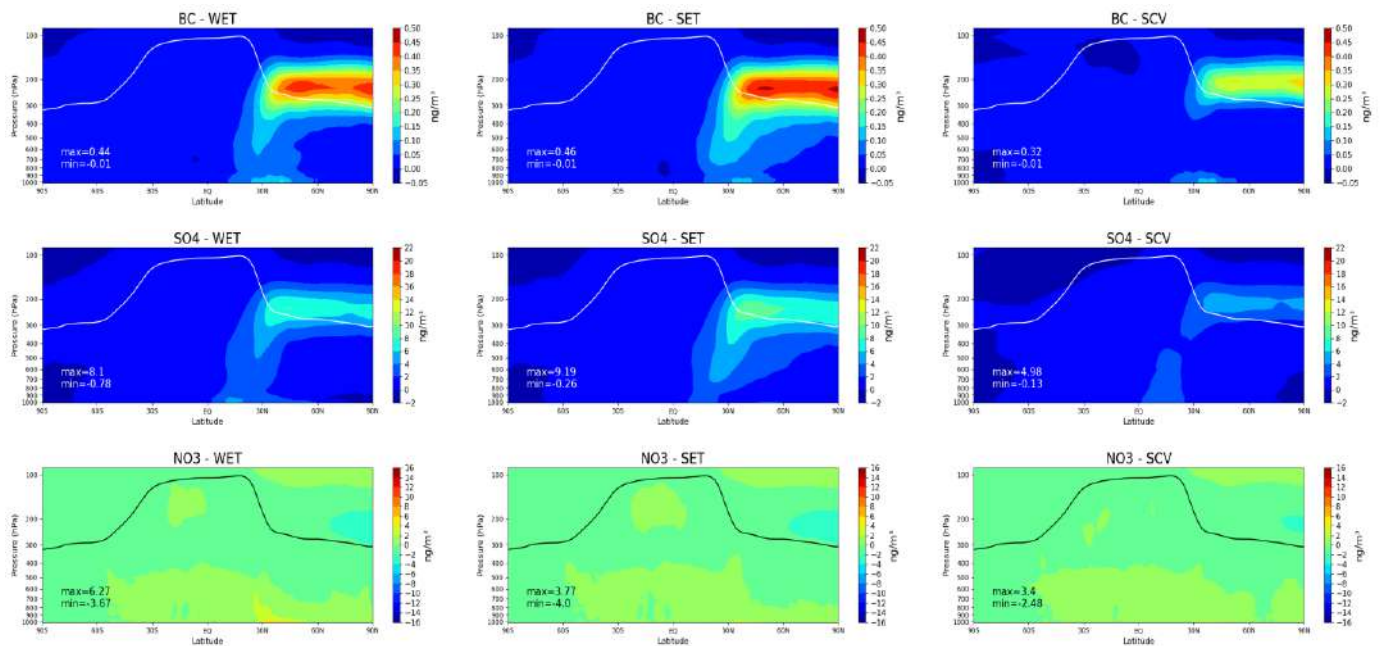


Figure 3-1: Zonal mean aviation perturbation in January for black carbon (top row), sulfate (middle row) and nitrate (bottom row) aerosols, respectively. The scavenging routines used are, from left to right, Wetdep, Sethet, and Scav.

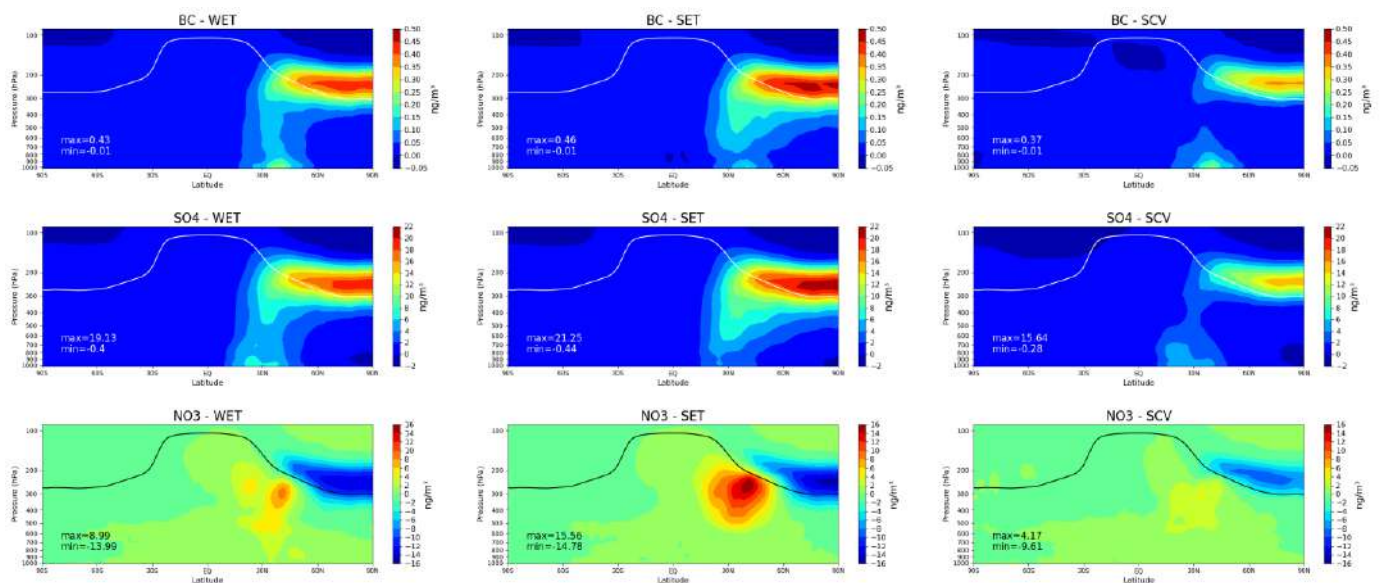


Figure 3-2: As Figure 3-1, but for the month of May.

Figure 3-3 shows the aviation perturbation to PM_{2.5} concentrations at the surface in May. PM_{2.5} is an important air quality indicator. The maximal perturbation is largest with Wetdep, being 33% and 20% lower with Sethet and Scav, respectively. As expected, the choice of scavenging routine impact surface PM_{2.5} originating from cruise emissions more than those originating from LTO emissions. Aerosols that are emitted higher in the atmosphere will likely meet more precipitations during their transport, hence be more sensitive to differences in scavenging rates. Concretely, switching from Wetdep to Sethet or Scav decreases the maximal PM_{2.5} perturbation by 33% and 20% respectively for LTO emissions, while it is 57% and 49% for cruise emissions.

Figure 3-3 shows that LTO emissions dominates the impact on surface air quality in regions around major airports such as North America, Europe and Eastern Asia. The impact of cruise emissions occurs over the oceans, the Middle East and the highly populated South Asia. Eastham et al. (2024) attributed 80% of aviation-induced premature deaths to cruise emissions, and it is not yet known how our results compare to that estimate. However, our results suggest a strong dependency on the way scavenging is represented in models, leading to more uncertainty than previously thought on aviation impacts on surface air quality.

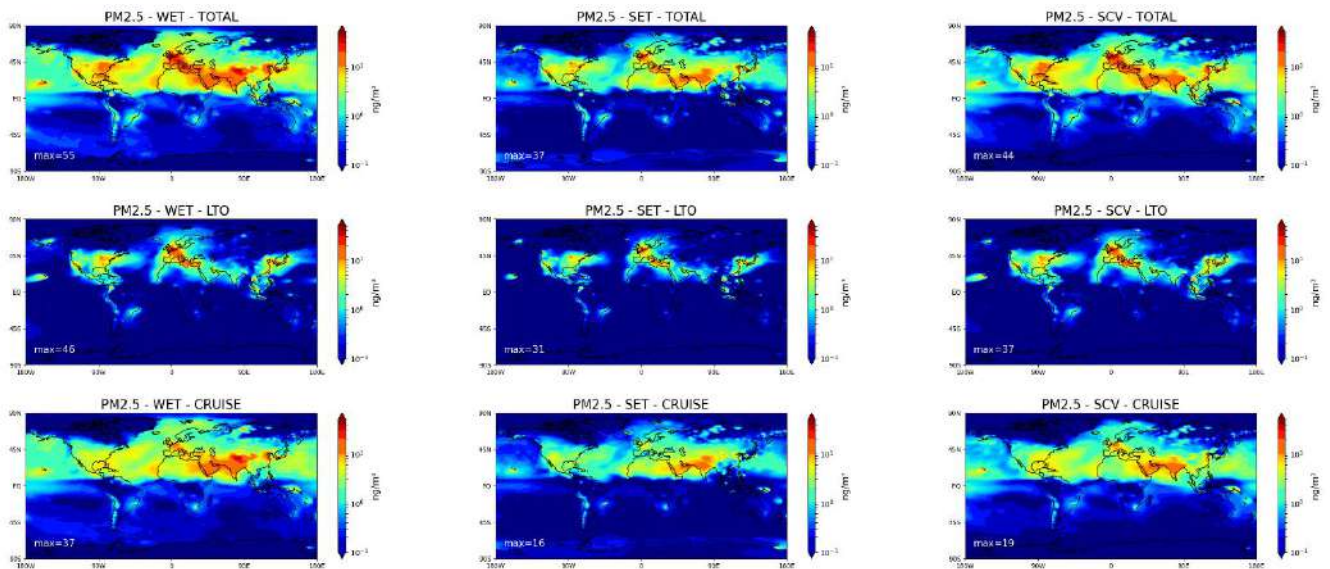


Figure 3-3: Perturbation to PM2.5 concentrations at the surface, in ng m^{-3} , by aviation emissions. The top row shows the perturbation due to total aviation emissions, while the middle and bottom rows show the perturbations caused by LTO and cruise emissions, respectively. The scavenging routines used are, from left to right, Wetdep, Sethet, and Scav.

3.3. WP 3.3: Cloud response to aerosol-cloud interactions

The objective of this work package is to understand, model, and predict the response of liquid, ice, and mixed clouds to a perturbation of their droplet and/or crystal counts.

3.3.1. Impact of aerosol perturbations on the formation and evolution of cirrus clouds

Contributors: Vincent Caillé, Lambert Delbeke, and Nicolas Bellouin (IPSL)

The work presented in this section builds upon the research conducted by Jhaswantsing Purseed, whose postdoctoral position concluded at the end of 2023. This study aims to investigate the aerosol-cloud interaction chain, specifically how aviation-induced emissions might influence the formation or temporal evolution of cirrus clouds. To achieve this, the MONC (Met Office NERC Cloud) model is employed—a Large Eddy Simulation (LES) model whose relatively high resolution enables a detailed examination of the microphysical processes governing cloud evolution through idealised simulations. These simulations are idealised in that they do not attempt to simulate an observed cloud, and they involve simplifications in the representation of the atmosphere and surface. Within MONC, cloud microphysics are represented by CASIM (Cloud and Aerosol Interacting Microphysics; Field et al., 2023).

Initially, we built on previous work investigating the influence of a perturbation on a pre-existing cirrus cloud in the atmosphere, focusing on the response of Ice Water Path (IWP) to a microphysical perturbation. This perturbation was introduced as a direct modification to the Ice Crystals Number Concentration (ICNC) in two types of cirrus clouds, called Gravity Wave Cirrus and Warm Conveyor Belt Cirrus after Kramer et al. (2020). However, this ICNC perturbation is not easily traceable to aviation emissions, since applying the perturbation itself assumes that there is a ICNC response to aviation emissions. That assumption goes against results by Kärcher et al. (2021). Still, such a simulation could be useful if it were possible to neatly separate the response of ICNC to an aerosol perturbation ($\frac{\partial N_i}{\partial N_a}$) from the response of IWP to an ICNC perturbation ($\frac{\partial I}{\partial N_i}$). But that assumption needs to be justified.

MONC model improvements are necessary to simulate the aerosol-ICNC part of the chain properly. To check those developments, we aim to reproduce the results of Kärcher et al. (2021), who employed a 1D model to simulate three cirrus cases: a base case, without a perturbation to aerosol concentrations, a plume case, where the cloud is perturbed by a large concentration of soot over a small area, and a background case, representing a perturbation by a lower soot concentration distributed over a wider range. Thanks to MONC developments, it is now possible to define multiple aerosol categories with different density, molar mass, and size distributions. More importantly, it is now possible to represent soot with a dedicated activation rate, as proposed by Kärcher et al. (2021). Dedicated soot ageing will be implemented soon.

Recent simulations with the improved model are encouraging. They show large differences between the base case and plume case (Figure 3-4). Parallel work by Farshid Naziri, described in the next subsection, focused on improving the model vertical resolution with the aim of bringing MONC predictions of ICNC and IWP evolution closer to those obtained by Kärcher et al. (2021). We are currently working on combining physical and resolution improvements to get the first complete set of simulations that we will be able to fully compare with the reference study.

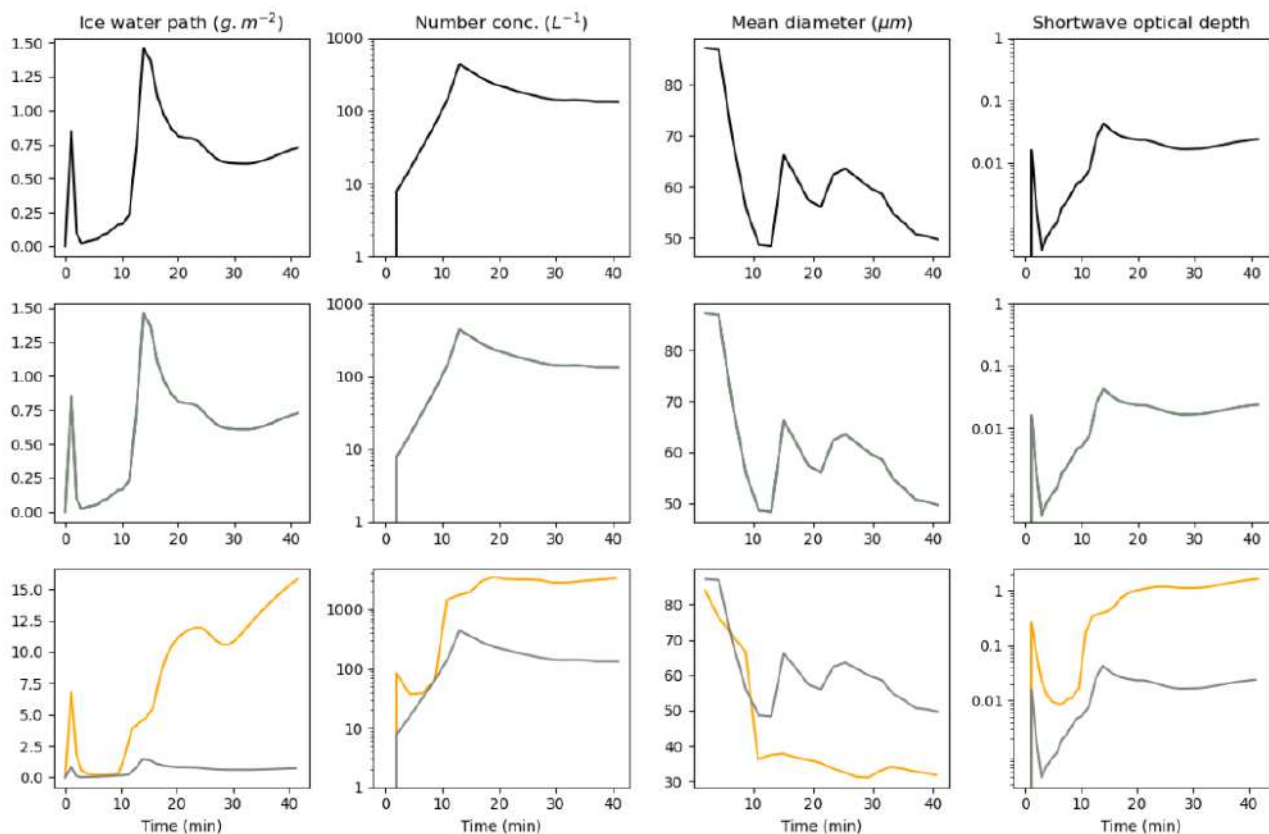


Figure 3-4: Temporal evolution of (from left to right) ice water path, ice crystals number concentration, ice crystal mean diameter and cirrus shortwave optical depth for base case (first row), background case (middle row) and plume case (last row). Base case results are plotted in grey in the background and plume panels, to make comparison easier.

3.3.2. Effects of MONC vertical resolution on cirrus cloud evolution

Contributors: Farshid Nazari and Nicolas Bellouin (IPSL)

In previous Climaviation Annual Reports, it was found using Large Eddy Simulation (LES) that idealised perturbations to ice crystal number in cirrus clouds lead, when applied when the cirrus cloud forms, to changes in ice water path and that such idealised perturbations can be obtained in a more realistic way by perturbing aerosols. A possible modification of the cloud response by atmospheric dynamics was also considered in last year's report. This was studied by changing the vertical subsidence forcing profile applied to the simulated domain, which results in a change in vertical velocity.

However, there is now a need to simulate a more realistic aerosol-crystal-response chain, as discussed in the previous section. Part of that requirement involves working at higher resolution that has been done so far in Axis 3 of Climaviation: the reference domain was 6 by 6 km with a 100 m horizontal resolution and 117 m vertical resolution, and a model top at 22 km. In what follows, simulations use initial profiles from Karcher et al. (2021). Figure 3-5 shows the result of a higher-resolution simulation, compared to this initial configuration case. The time evolution of ice mass mixing ratio (IMMR) shows a clear difference between the two simulations, which are due to the impact of the model resolution. The cloud is thinner and more rapidly dissipated at higher resolution. In both cases, the cloud height is from 9.5 to 11 km with larger IMMR in higher altitudes. The quantitative comparison of different resolutions is shown in Figure 3-6, for an initial aerosol radius of 40 nm. The results converge as the resolution increases, as for the 50 m horizontal and 40 m and 20 m vertical resolutions, very similar ICNC and IMMR are obtained, and they are in good agreement with the simulations by Karcher et al. (2021). As shown, the cirrus cloud starts to develop at around 800-900 s, at

peak ice supersaturation. The IWP continues to increase thereafter due to continued homogeneous freezing at the cloud top until ice crystals are lost because of micro-physical processes.

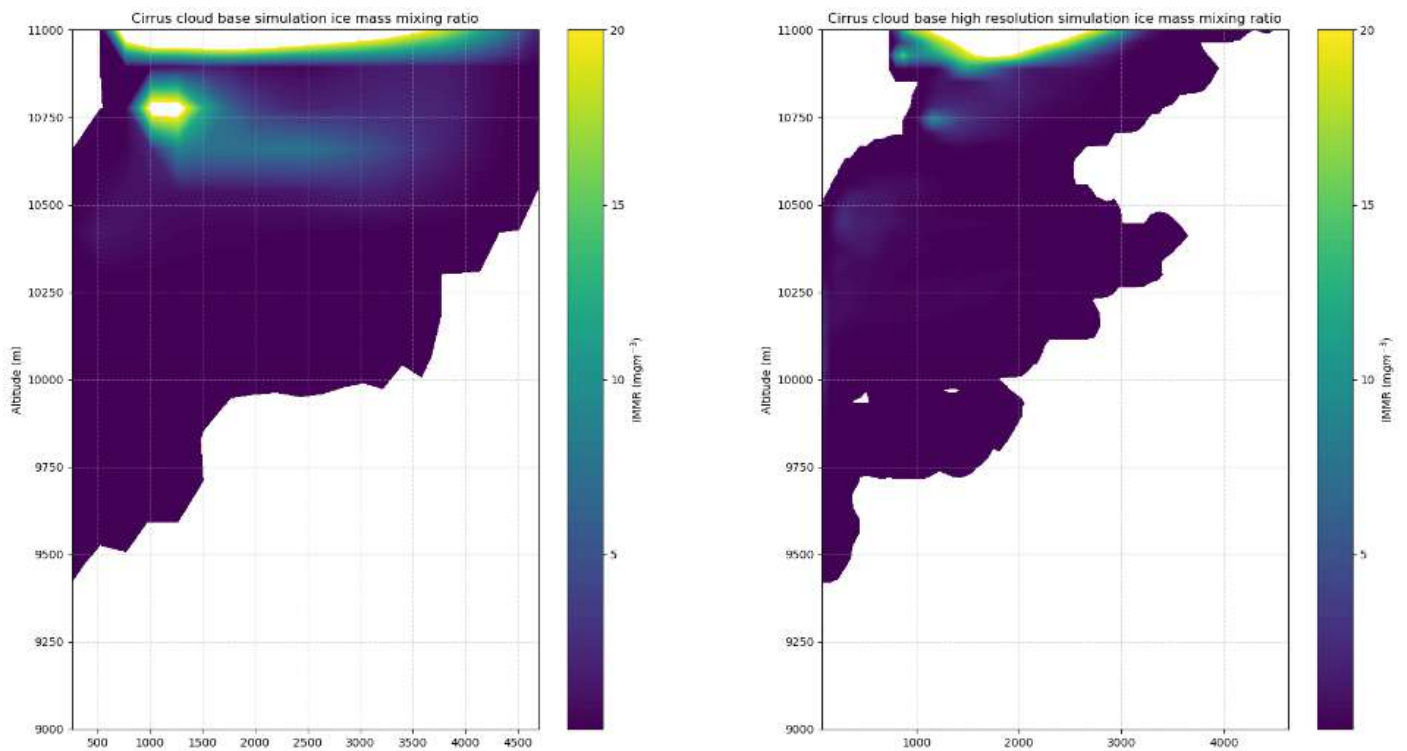


Figure 3-5: Time series of the vertical profile of ice crystal mass in (left) the base configuration (6×6 km², 100-m horizontal, 117-m vertical, model top at 22 km) and (right) a higher resolution simulation with a 3×3 km² domain, 50-m horizontal, 40-m vertical, and 15 km model top. The x-axis shows time in seconds.

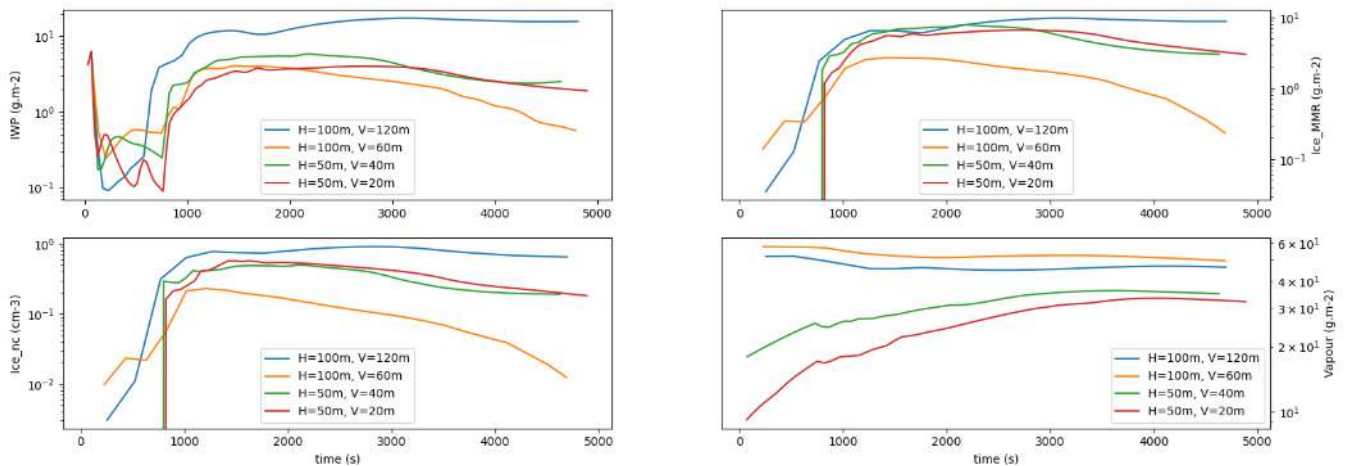


Figure 3-6: Time series of ice water path (g.m^{-2}), ice mass mixing ratio (g.m^{-2}), ice crystal number concentration (cm^{-3}), and vapour mass ratio (g.m^{-2}) from top to bottom. The different horizontal and vertical resolutions are shown by the different coloured lines.

4. AXIS 4: OBSERVATION

The objectives of the fourth axis of research are to use existing data in new ways and acquire additional observations to extract information that will allow an evaluation and a recalibration of the mainly numerical results on which the study of atmospheric mechanisms is based.

4.1. WP 4.1: Use of existing data

The objective of this work package is to survey existing observational data on contrails and to develop algorithms for large-scale processing to create a database that can be used to evaluate and calibrate the results obtained by numerical simulation to describe the evolution of contrails at different scales.

4.1.1. Contrail automatic detection on ground-based camera

Contributors: Nicolas Gourgue, Laurent Barthes, and Olivier Boucher (IPSL)

4.1.1.1. Ground-based image database

We have finished labelling the database of ground-based images taken by the hemispheric camera at SIRTAs with the roboflow utility. This database is needed to evaluate both morphological and deep learning algorithms. The annotated database contains 1600 images, including 1025 images with contrails. We have published this database in open access in EASY DATA storage (Gourgue et al., 2025). Annotations are based on 7 classes:

- *Maybe contrail* for very small contrails without certainty.
- *Young contrail* for linear contrails that appear within 3 minutes of a plane flying in the camera's field of view.
- *Old contrail* for linear contrails that are older than 3 minutes.
- *Very old contrail* for other contrails,
- *Parasite* for sun reflection that happens to look like a contrail.
- *Sun* for the solar disc
- *Unknown* for other contrail-looking shapes.

Each image is checked twice. Figure 4-1 shows an example of an annotated image.

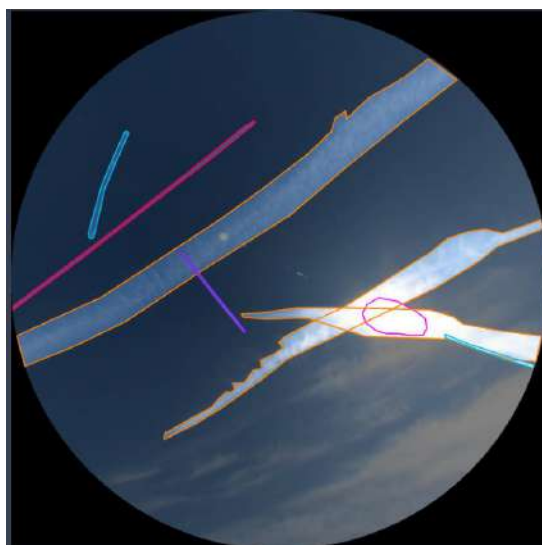


Figure 4-1: Annotation example with polygons

We complete the contrail classes with tags. The first four tags concern cloud cover:

- *Blue sky* when there are no clouds.
- *Broken cloud* for cases where less than 50% of the image is cloudy.
- *Mostly cloud* for the cases where more than 50% of the image is cloudy.
- *Full overcast* for cases where the image is completely cloudy.

Figure 4-2 shows examples of those four tags.

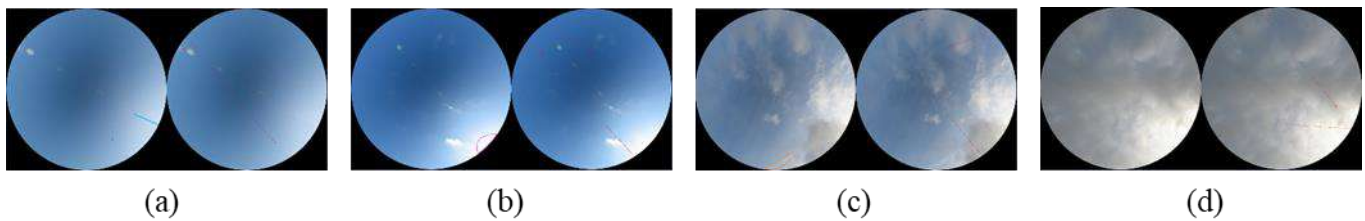


Figure 4-2: Examples of clouds tag. (a) blue sky. (b) broken cloud. (c) mostly cloud. (d) full overcast.

The annotated image database was built to be balanced with respect to the different classes. The *Maybe* contrail and *Unknown* are under-represented because they are not very relevant. For the other contrails, we have a few hundred objects for each class.

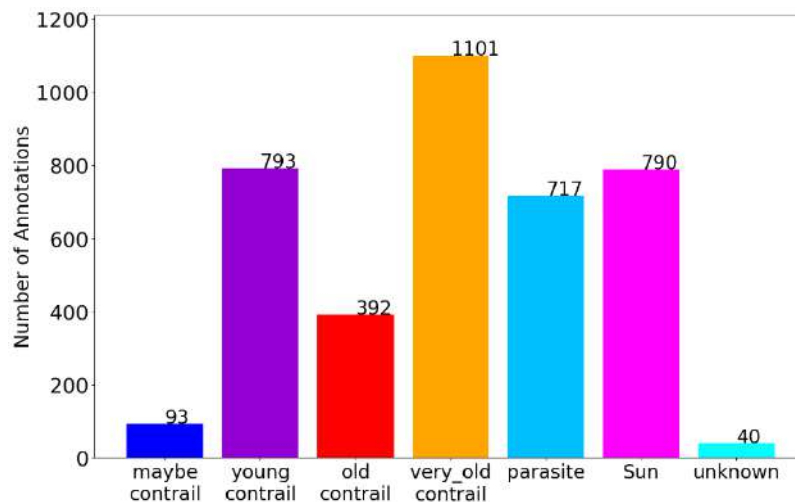


Figure 4-3: Class annotation repartition

4.1.1.2. Morphological algorithm

Last year, we used the young contrails produced by the database described in the previous section to optimise certain parameters of the morphological algorithm. We have 300 images for optimisation and 100 images for testing. Figure 4-4 shows that performance deteriorates with increasing cloud cover, as mentioned last year. However, performance between the test and optimisation databases is comparable.

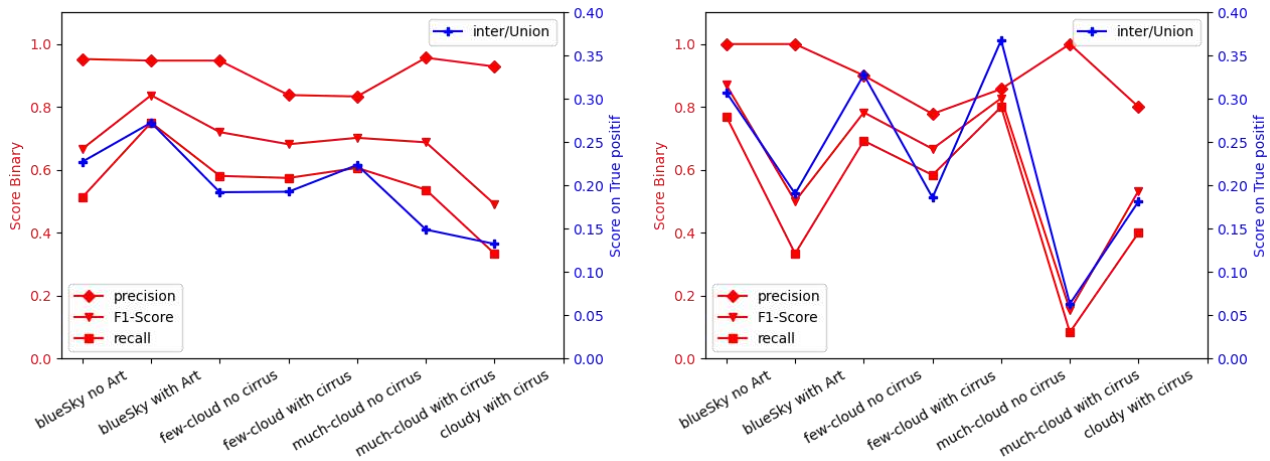


Figure 4-4: Performance scores of the morphological algorithm compared to annotated contrail images. On the left, morphological performance on the optimisation dataset. On the right, morphological performance on the test dataset.

We have now started the analysis of the original hemispherical image database. We are processing 5 years from 2019 to 2025 to analyse the detection characteristics. We added a qualitative module to perform contrail tracking between consecutive images. We cannot evaluate tracking performance globally, but we can only check the part of the anomalous value. Looking at the growth in contrail width, we estimate a maximum growth of 5 or 10 pixels between two images separated by two minutes. Plotting the growth rate as a function of time is therefore an initial estimate of algorithm misidentifications. The red line corresponds to growth of 0 pixels and the green line to growth of 10 pixels. The violin plots in Figure 4-5 show that most time steps produce a number of pixels below 10 and few extreme values.

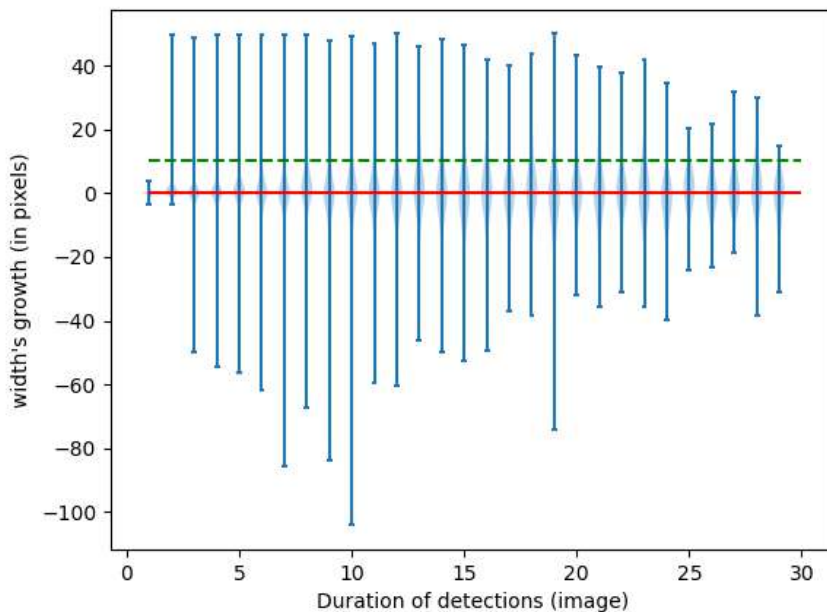


Figure 4-5: Violin plot of velocity of width growth contrail. The x-axis shows the number of images in which a given contrail is detected, with 1 image every 2 minutes.

Regarding contrail detection counts, Figure 4-6 shows the number of contrails detected for each day in the database. The same contrail detected in the next image counts as one. We detect a large number of contrails and we can see a seasonality in detection because in summer the days are longer and less likely to be overcast so the number of detections can be higher. Note the small number of detected contrails during the year 2020, when the Covid pandemic strongly reduced the number of flights.

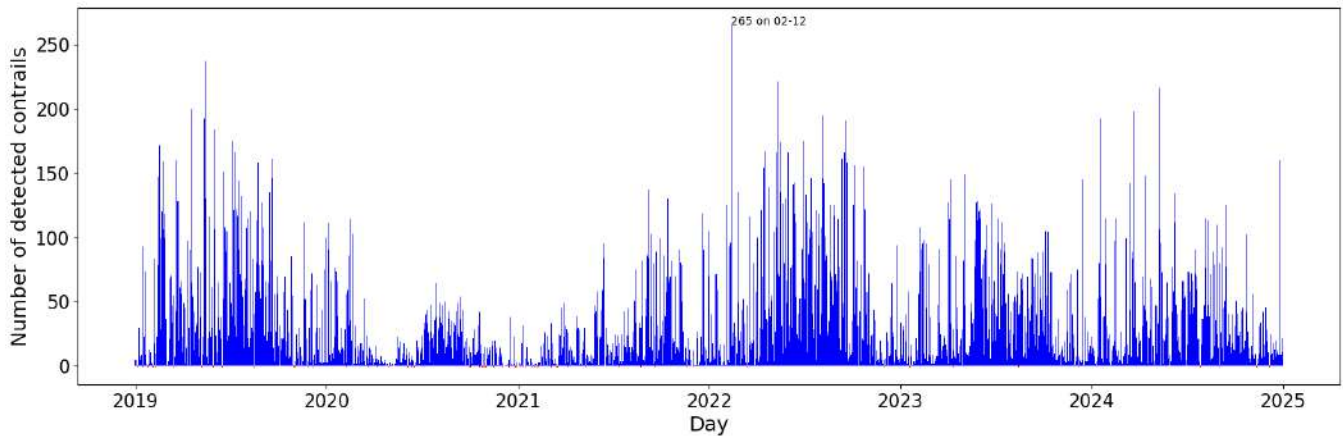


Figure 4-6: Number of contrails detected by day as obtained by the morphological algorithm applied to the hemispheric camera image database from 1 Jan 2019 to present.

4.1.1.3. Deep learning

The second activity is to train a deep-learning algorithm to detect contrails in the ground camera imagery. We are restarting the training with the full database. We are using the same architecture as last year, Unet and deeplabV3, and the same way to eliminate bias like splitting database with randomly drawn days to generate the dataset to avoid images with little time between them ending up in different datasets. We need one month to train a complete model. The Unet model has almost finished learning. Its results are encouraging, as shown in the confusion matrices shown in Figure 4-7. We have the complete confusion matrix with a correct score for each class except for *Old contrail* because this class is under-represented and is between *Young contrail* and *Very old contrail*. The image on the right in Figure 4-7 is the confusion matrix with *Young contrail*, *Old contrail* and *Very old contrail* aggregated in *contrail* class and all others in *No contrail*. The confusion matrix shows a good classification, with most cases falling on the diagonal.

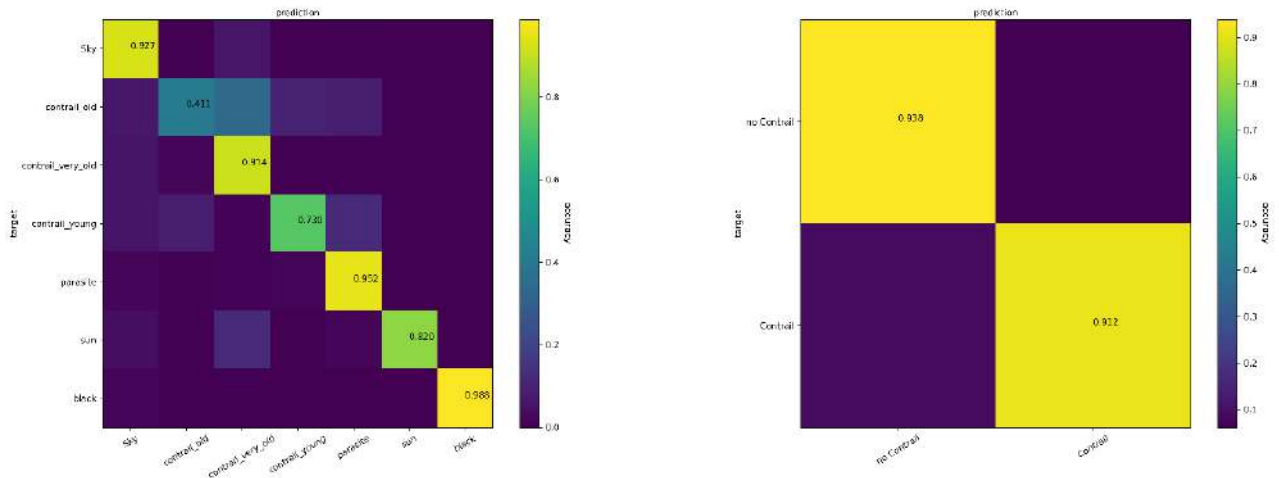


Figure 4-7: Confusion matrix. On the left, confusion matrix with all classes. On the right, the confusion matrix with only contrails.

4.1.2. Selection of interesting past cases with strong instrumental synergy

Contributor: Cheikh Dione (IPSL)

This study aims to quantify the optical, geometrical and microphysical properties of contrails at the SIRTa observatory in Palaiseau, France. We used a co-localised instrumental synergy consisting of the multi-channel Raman Lidar IPRAL, a total sky camera, and aircraft flight altitudes received from ADS-B to detect the occurrence of contrails over the site during the period 2018-2023.

We analysed day by day the possible occurrences of contrails over the SIRTa, using the data from the Lidar and the total sky camera. This laborious work has allowed us to identify 3 case studies of contrail outbreaks and to document their characteristics. The first case study is observed on 26 February 2019 and is characterised by contrails that form under thin cirrus and have a short lifetime. The second case study is observed on 7 July 2019, and concerns contrails that form under clear sky and having relatively long lifetime. And the last case study is observed on 22 July 2022, and concerns contrails formed in a layer of natural cirrus clouds observed. Based on these three case studies, the particular and molecular integration methods are applied to Lidar backscatter, to estimate the optical depth of the contrails. As an illustration, Figure 4-8 shows the total sky camera image on 7 July 2019 at 1050 UTC and the lidar backscatter measurement for the same period.

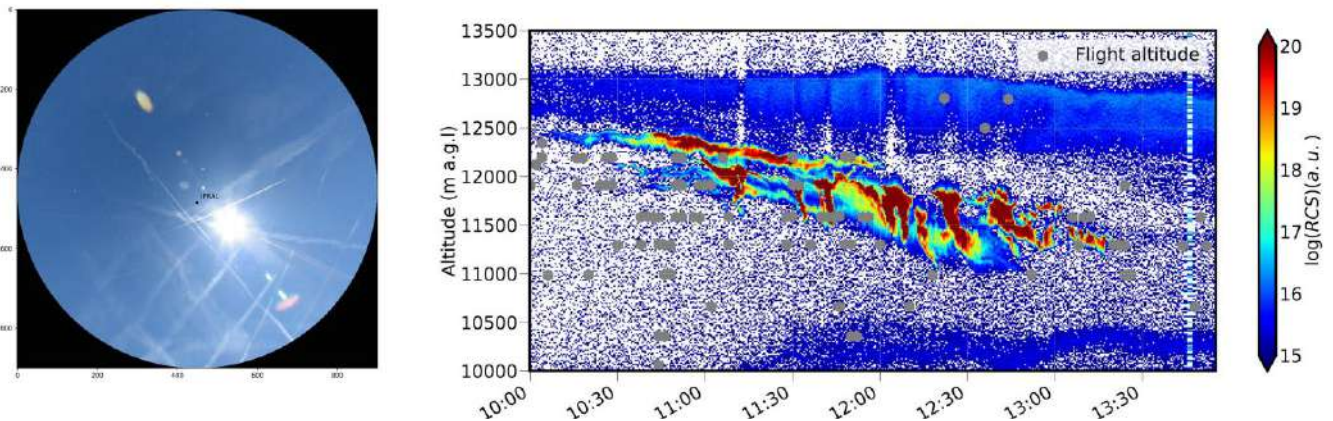


Figure 4-8: 7 July 2019 case study: total sky camera image at 1050 UTC (left) and lidar backscatter measurement from IPRAL (right)

In a second step, we use the vertical profiles of air temperature and relative humidity from radiosoundings at Trappes to characterise the atmospheric conditions in which these contrails form, based on the criteria of Wolf et al. (2023), following the Schmidt-Appleman criterion (SAc) and the definition of the ice supersaturation regions (ISSR). These criteria characterize the layer in which contrails form into three categories: non-persistent, persistent, and spreading. Results show that contrails often form in the persistent layer and that their duration and optical thickness depend on the thickness of this layer.

We use the particular integrated (PI) method to estimate, with the IPRAL backscatter coefficient at 1064 nm, the evolution of the optical depth of contrails over this instrument and calibrated the optimal Lidar effective ratio (18). Over the Lidar, we find a variability of contrail optical depth, as shown on Figure 4-9.

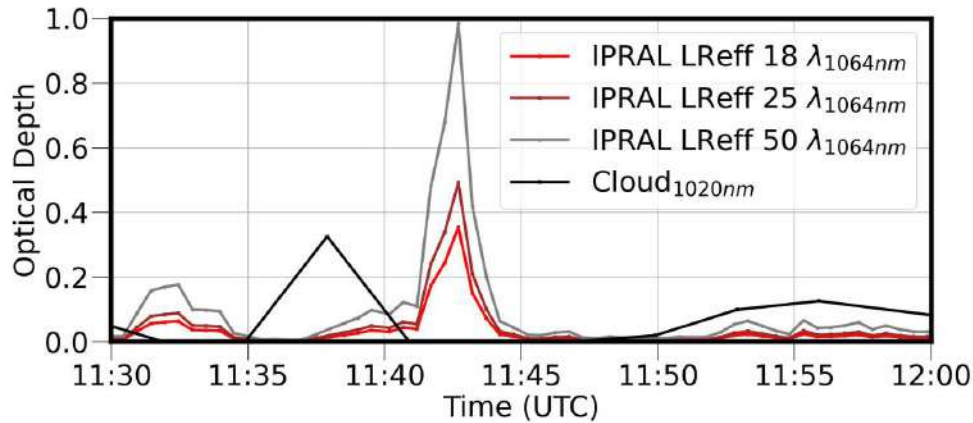


Figure 4-9: Contrail optical depth retrieved from the IPRAL lidar with the Particular Integrated method for the 7 July 2019 case study

The case study of 7 July 2019 is further documented by the Sentinel-2 image at 10:50 UTC, which shows a large contrail outbreak covering a large area south of the observatory. Using SIRTAs pyranometers, we evaluate the radiative impact of the contrail at -218 W m^{-2} for this case. During the day, young contrails contribute to a significant reduction of the measured surface downwelling and upwelling shortwave radiation. Their effect on longwave radiation is relatively small compared to that of shortwave radiation.

4.2. WP 4.3: Model evaluation for contrail prediction

The objective of Work Package 4.3 is to use contrails, clouds, and atmospheric chemistry observations to evaluate models.

4.2.1. Radiative effect of two contrail outbreaks estimated using geostationary satellite observations

Contributor: Xinyue Wang (Postdoctoral Researcher, IPSL)

Contrails contribute significantly to aviation-induced climate effects, yet their energy forcing (EF) remains challenging to quantify. The Contrail Cirrus Prediction (CoCiP) model (Schumann, 2012) is a Lagrangian model that simulates contrail evolution based on meteorological inputs, providing estimates of contrail optical depth, ice water content, and radiative forcing. While widely used, its accuracy depends on cloud property assumptions and radiative transfer calculations.

To assess CoCiP's performance, we compare its EF estimates with those from our previously published case study (Wang et al., 2024), where MSG/SEVIRI satellite retrievals by EUMETSAT's Optimal Cloud Analysis (OCA) and ecRad radiative transfer modelling were used to quantify contrail EF. That study demonstrated the feasibility of deriving contrail radiative effects from remote sensing data, but some uncertainties remained, particularly related to thin contrail detection and cloud property retrievals. Here, we apply CoCiP to the same case and compare its outputs against ecRad to evaluate differences in warming and cooling trends, cloud properties, and radiative transfer treatments.

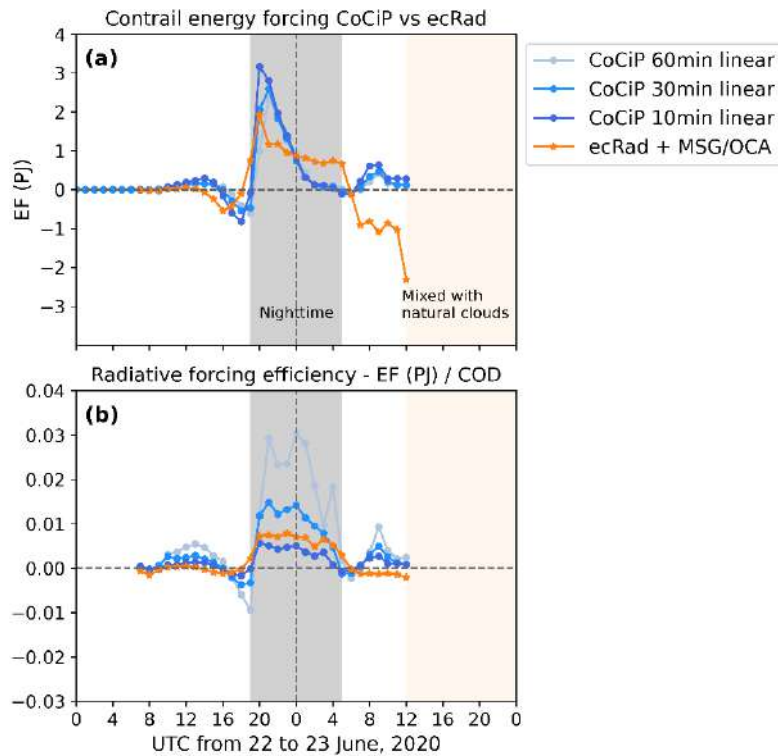


Figure 4-10: Time series of contrail energy forcing and radiative forcing efficiency for 22–23 June 2020. (a) Total contrail energy forcing (EF) estimated using the CoCiP model with different time steps (blue colours, 10 min, 30 min, and 60 min, all using linear interpolation of meteorological data) is compared to EF derived from the ecRad radiative transfer model combined with MSG/OCA satellite observations (orange). (b) The radiative forcing efficiency, defined as the energy forcing per unit contrail optical depth (EF/COD), is shown for the same datasets.

Figure 4-10 shows the comparison between CoCiP and MSG/OCA/ecRad. It shows a reasonable agreement in contrail energy forcing (EF) on 22 June, with both models capturing a similar pattern of warming and cooling effects. However, a discrepancy emerges from the beginning of 23 June (0–4 UTC), where the ecRad output exhibits a persistent warming effect, whereas CoCiP predicts a rapidly decreasing warming. This discrepancy becomes more pronounced in the morning (5–12 UTC), where CoCiP simulates a warming effect, while ecRad suggests a cooling effect. When analyzing spatial distributions, we observed that between 5–12 UTC, thin contrails were present in the CoCiP output, and were partially detected by the MSG satellite, yet they were not successfully retrieved by the optimal cloud analysis (OCA) algorithm. This retrieval limitation aligns with previous studies showing that the OCA algorithm has difficulties detecting optically thin contrails, especially under certain atmospheric conditions (Watts et al., 2011; Vidot et al., 2015). The latest version of the OCA retrieval scheme should improve performance for MTG observations, potentially reducing such inconsistencies.

To further investigate the differences in warming and cooling effect distributions between CoCiP and ecRad, we ensured that the surface properties, temperature, and humidity profiles were as consistent as possible between the two models. This suggests that the observed discrepancies may be attributed to input cloud properties or differences in radiative transfer calculation schemes. The ECMWF IFS, which provides ERA5 distributions, uses ecRad as its radiative transfer model (Hogan et al., 2017). CoCiP takes some radiative flux distributions from ERA5 but uses its own look-up table based on libradtran for EF calculations.

To isolate the impact of optical depth variations, Figure 4-10(b) presents the radiative efficiency (EF per unit COD), which minimises the influence of COD differences. The discrepancy during nighttime (0–4 UTC) is

significantly reduced, particularly between CoCiP with a 10-min timestep and MSG/OCA/ecRad. However, CoCiP still maintains a warming effect between 5–12 UTC. It is possible that the way ECMWF IFS represents radiation tendencies and cloud-radiation interactions may introduce biases when used as input for CoCiP. But assumptions built-in within CoCiP must also contribute, and work is ongoing to identify those.

Previous studies have demonstrated that contrail radiative forcing is highly sensitive to ice crystal properties, optical depth, and cloud overlap assumptions (Schumann et al., 2012; Brasseur et al., 2016). A more detailed comparison of the cloud phase assumptions, ice particle size distributions, and COD parameterizations could provide further insight into the differences in contrail radiative forcing between CoCiP and ecRad. To further validate these findings, we plan to expand our evaluation by including more cases under different meteorological conditions, which will allow for a more comprehensive assessment of the model differences and retrieval uncertainties.

5. AXIS 5: CLIMATE IMPACTS OF AVIATION

The fifth axis of research aims to bring together the advances made in the modelling and evaluation of the various contributors to the radiative perturbation generated by aviation, to assess the resulting total impact on climate change.

5.1. WP 5.1: Traffic and emission scenarios

The objective of work package 5.1 is to quantify all air traffic emissions and their spatial and temporal distribution over the globe, and to define scenarios for the evolution of air transport.

Contributors: Claire Sarrat (ONERA), Judicaël Bedouet (ONERA), Brieuc Danet (ONERA)

5.1.1. Global emissions inventory

The 4D global emission inventory is based on the air traffic simulator developed by ONERA and described in Joulia et al. (2025). The ATMLab is a comprehensive suite of hardware and software tools designed for research in Air Traffic Management (ATM). The platform integrates various functionalities, including simulations, data analysis, and visualization, to support ATM-related studies. Additionally, ATMLab operates a network of ADS-B antennas that cover a large portion of French airspace, providing real-time flight data. ATMLab's software architecture follows a microservices approach, allowing independent, modular services tailored to specific research needs. One of its primary applications is the assessment of the environmental impact of aviation, particularly its contribution to climate change.

For the aviation environmental impact assessment, the simulation framework within ATMLab is described on Figure 5-1. In this study, it relies on meteorological data from ECMWF ERA5 reanalysis. This dataset provides essential atmospheric variables, including pressure, wind, temperature, and humidity, which influence flight performance and emissions modelling. Flight simulations in ATMLab estimate fuel consumption based on EUROCONTROL's BADA3 aircraft performance model. These simulations use both direct and inverse methods to reconstruct flight trajectories and compute fuel consumption and emissions. The platform also integrates machine learning techniques for data-driven performance estimation (including take-off masses).

ATMLab relies on **both direct and inverse simulation methods**, particularly because the study is based on ADS-B flight trajectories. However, these ADS-B data streams can be incomplete:

- For flights over well-covered regions (e.g., continental airspace), we often have detailed and continuous ADS-B tracks, enabling accurate inverse simulations based on real-world data.
- For trans-oceanic flights or remote areas, ADS-B coverage is limited or non-existent. In these cases, only a few data points are available—typically the departure and arrival positions, with no intermediate waypoints.

To compensate for these gaps, a hybrid approach is required, combining **inverse simulations**, when sufficient ADS-B data is available, with **direct simulations** to reconstruct missing trajectory segments.

- **Inverse simulation** is used to analyse real ADS-B trajectories where data is dense. By differentiating successive positions, we compute horizontal/vertical speeds, acceleration, and then infer thrust and fuel consumption.
- **Direct simulation** is necessary when ADS-B data is missing. In such cases, a flight plan is reconstructed using a performance model, meteorological conditions, and navigation constraints to estimate the aircraft's trajectory. Figure 5-2 illustrates a direct simulation.

For transoceanic flights, this means that the simulation process typically consists of:

1. Inverse simulation for the departure and arrival phases, where ADS-B data is available.
2. Direct simulation to reconstruct the missing en-route phase, ensuring consistency with atmospheric conditions and aircraft performance models.

By combining both approaches, ATMLab ensures a more accurate estimation of fuel consumption, emissions, and climate impact, even when ADS-B data is incomplete.

In terms of emissions modelling, ATMLab calculates the production of CO₂, NO_x, SO_x, and other pollutants using the Boeing Fuel Flow Method (BFFM2). Additionally, it includes the open-source version of CoCiP, PyContrail, which uses the Schmidt-Appleman Criterion and Ice Supersaturated Regions (ISSR) to quantify the climate impact of contrails.

The output of these simulations will be a 4D gridded emissions inventory with the following characteristics:

- 1° of latitude and longitude resolution.
- 500 m of vertical resolution.
- Hourly timestep on an annual basis.
- Meteorological data from the ERA5 reanalysis (including corrections for the humidity bias).
- Emissions of CO₂, NO_x, nvPM, SO₂, H₂O.
- Number of aircraft per grid cell, number of kilometres travelled by aircrafts per grid cell.

Overall, ATMLab provides a robust environment for studying the interaction between aviation and climate, enabling both retrospective analysis and predictive modelling for future air traffic scenarios as described in Section 5.1.2.

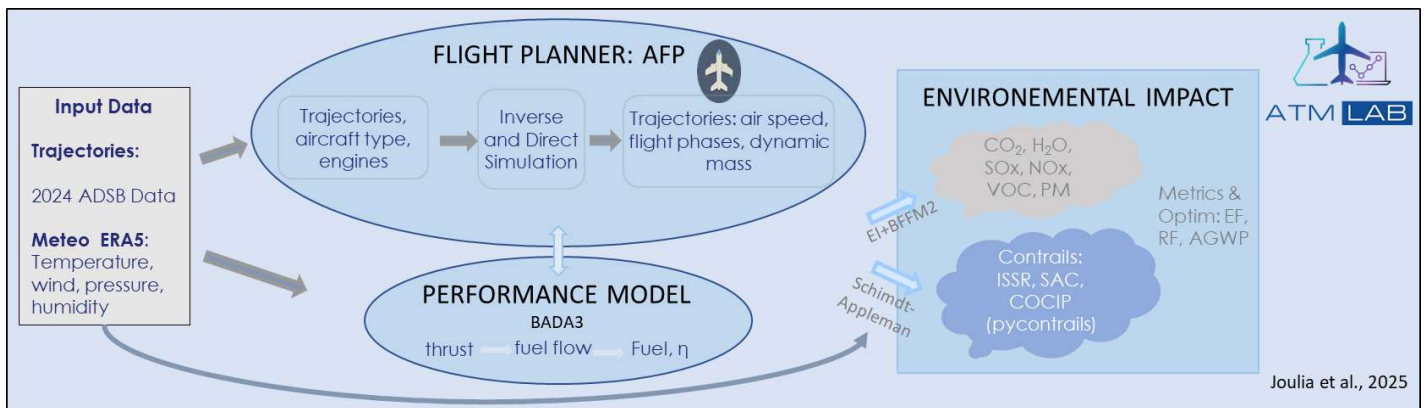


Figure 5-1: ATMLab framework for environmental impact studies

Direct simulation

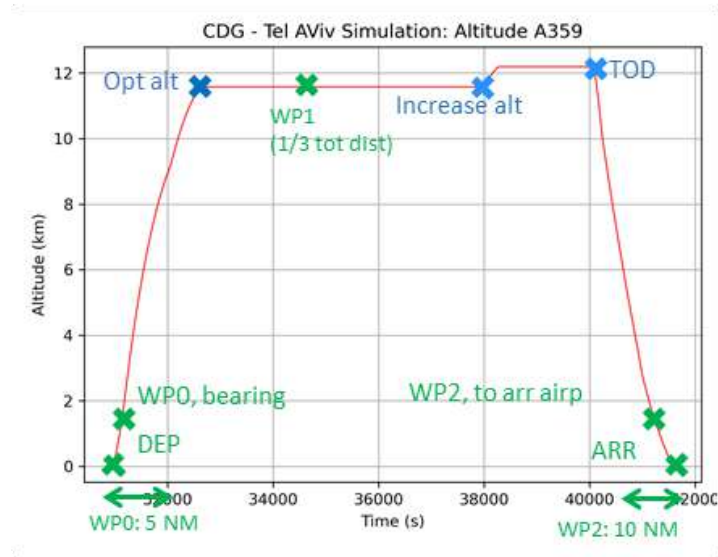


Figure 5-2: Example of a direct simulation based on the departure and arrival coordinates.

5.1.2. Scenarios for future aviation

5.1.2.1. Work Approach

The work approach of Task 5 relies on the ATM-Lab, the ONERA's air traffic simulator, which generates a "4D" mapping of annual air traffic emissions worldwide (Section 5.1.1).

This work proposes to exploit future air transport evolution scenarios to evaluate corresponding emission changes and ultimately assess their climate impact at a given horizon.

Initially, we rely on trend-based scenarios that forecast air traffic evolution by projecting past trend analyses. These scenarios, developed by air transport stakeholders (aircraft manufacturers, airlines, or airports), provide the advantage of quantified evolution laws for central air transport data (passenger volumes, aircraft replacement rates, etc.). Typically, these are normative scenarios built as strategic plans to achieve specific objectives at a given horizon, such as the "Zero CO₂ Emissions by 2050" goal set by the ICAO.

A second phase should consider more prospective exploratory scenarios, aiming not to predict the future but to evaluate the capacity of the air transport system to meet its objectives despite strong political, economic, and societal uncertainties.

5.1.2.2. Hypotheses for Air Transport Evolution

Most normative scenarios envisioned by air transport stakeholders (ATAG, ICAO, IATA) assume constant growth in air traffic in the coming years, consistent with pre-COVID trends. However, CO₂ emission reduction objectives must be achievable through a set of measures and technological advances, including:

- Substantial technological progress for engine technology, and to a lesser extent or at a more distant horizon, new aircraft configurations.
- Progressive but massive production and use of more sustainable fuels.

- Continuous improvements in air operations.

Quantified hypotheses vary across scenarios. These hypotheses can be discussed but do not question the methodology for accounting for air transport emission evolution.

5.1.2.2.1. Traffic Growth

Firstly, we consider continuously growing traffic worldwide, with significant regional variations. Notable disparities can be envisioned between national/regional and international flights in certain countries.

Boeing provides the most comprehensive forecasts, distinguishing:

- On the one hand, the growth of transport volume in RPK or Revenue Passenger Kilometres, see Figure 5-3), which integrates both passenger numbers and kilometres travelled.
- On the other hand, the evolution of the number of flights performed and the corresponding aircraft need, accounting for both fleet replacement (with a global average rate) and specific traffic growth in each zone (see illustration on Figure 5-4)

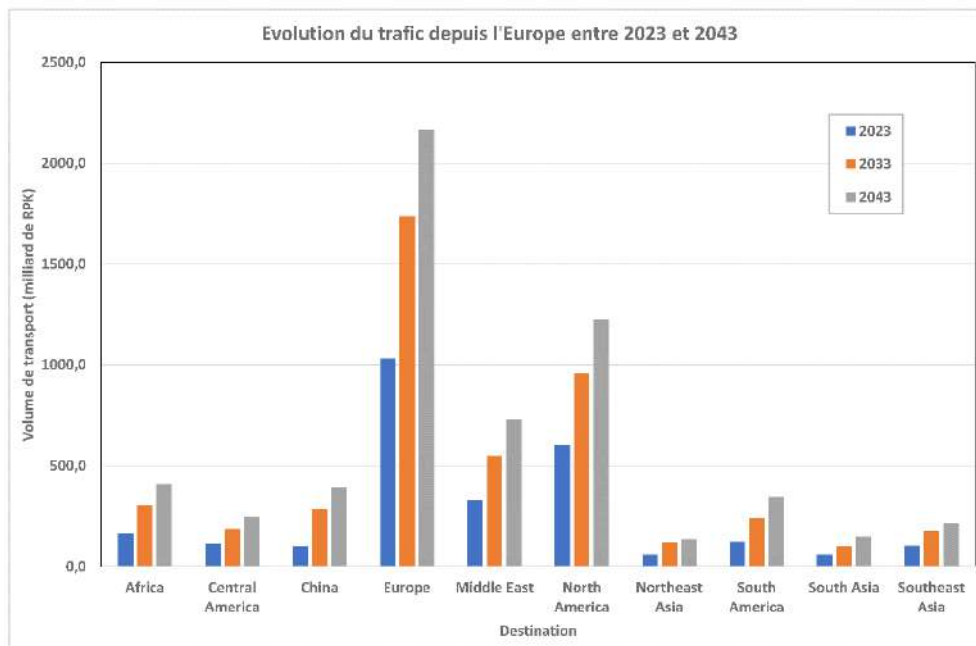


Figure 5-3: Passenger traffic evolution from Europe, in billion RPK, between 2023 and 2043. Boeing data.

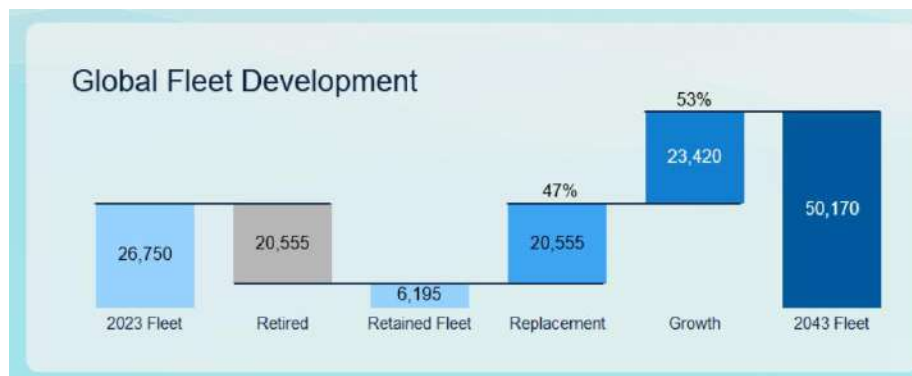


Figure 5-4: Assessment of new aircraft demand between 2023 and 2043. Boeing data.

5.1.2.2.2. Technological Advances

Technological advancements primarily aim to reduce aircraft in-flight fuel consumption (at equivalent thrust levels), thus decreasing CO₂ emissions, through new engine technologies and more efficient configurations. However, these improvements are tied to fleet renewal, which will occur heterogeneously based on airlines' investment choices and commercial strategies.

IATA estimates that each aircraft generation has reduced consumption by 15% to 20%, a trend that could continue until 2043. This hypothesis aligns with the CORAC's "Business as Usual" scenario (CORAC 2021), assuming 15% performance improvement every 15 years. More ambitious scenarios foresee the arrival of:

- A new regional aircraft in 2035 with 20% gains.
- A new SMR aircraft between 2033 and 2035, improving performance by 30%.
- A new long-haul aircraft in 2037 with 20% gains.

5.1.2.2.3. Usage of Sustainable Aviation Fuels (SAF)

The International Air Transport Association (IATA) estimates that in 2023, coal, oil, and natural gas represent 80% of the energy consumed by the industry globally, with a goal to reduce this figure to 20% by 2050. The difficulty for air transport in using renewable energy sources (solar, wind) and the high price of SAF as the primary alternative to oil (2 to 5 times more expensive) lead to setting a target of 45% for the aviation sector by 2050 (IATA, 2024). Furthermore, the progressive use of aromatic-free synthetic fuels is expected to reduce the number of generated particles, thus perhaps decreasing contrails formation and their impact on climate.

Nevertheless, the availability of synthetic fuels, the number of airlines that can use them, and the number of airports capable of providing them remain highly uncertain for the coming years. ICAO has defined several scenarios to simulate the incentive for SAF production, the profitability of different production means, and the priority given to aviation for their use. Various hypotheses, linked to the need (low/medium/high) depending on traffic growth, have been integrated into ICAO's LTAG scenarios (ICAO, 2022) (Figure 5-5).

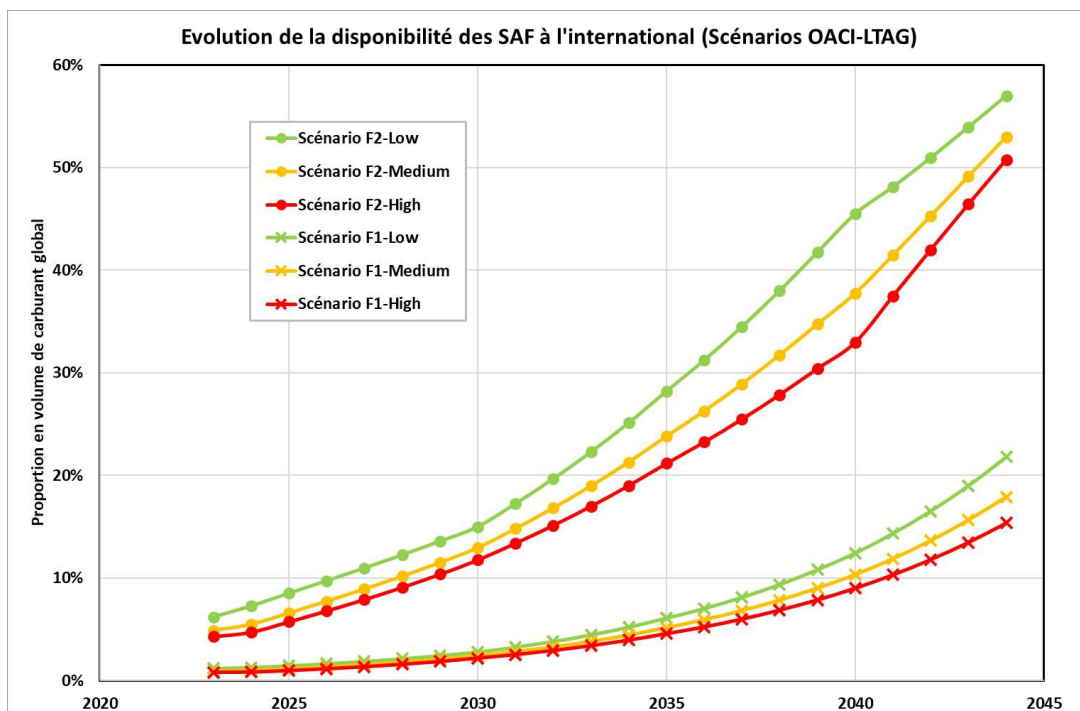


Figure 5-5: Evolution of SAF Availability between 2023 and 2044 (Source ICAO-LTAG)

5.1.2.3. Simulation of Future Emissions

Various hypotheses regarding traffic growth evolution, technological advancements, and SAF usage extracted from aviation stakeholder scenarios can be integrated into the ATM-Lab calculation chain, as presented in Figure 5-6.

Thus, traffic growth hypotheses by global region directly impact fuel expenditure on corresponding trajectories, while technological improvements can reduce engine emission indices and aircraft consumption, considering a variable fleet replacement rate depending on the airline. Similarly, SAF can decrease emissions in regions where they are expected to be available in sufficient quantities.

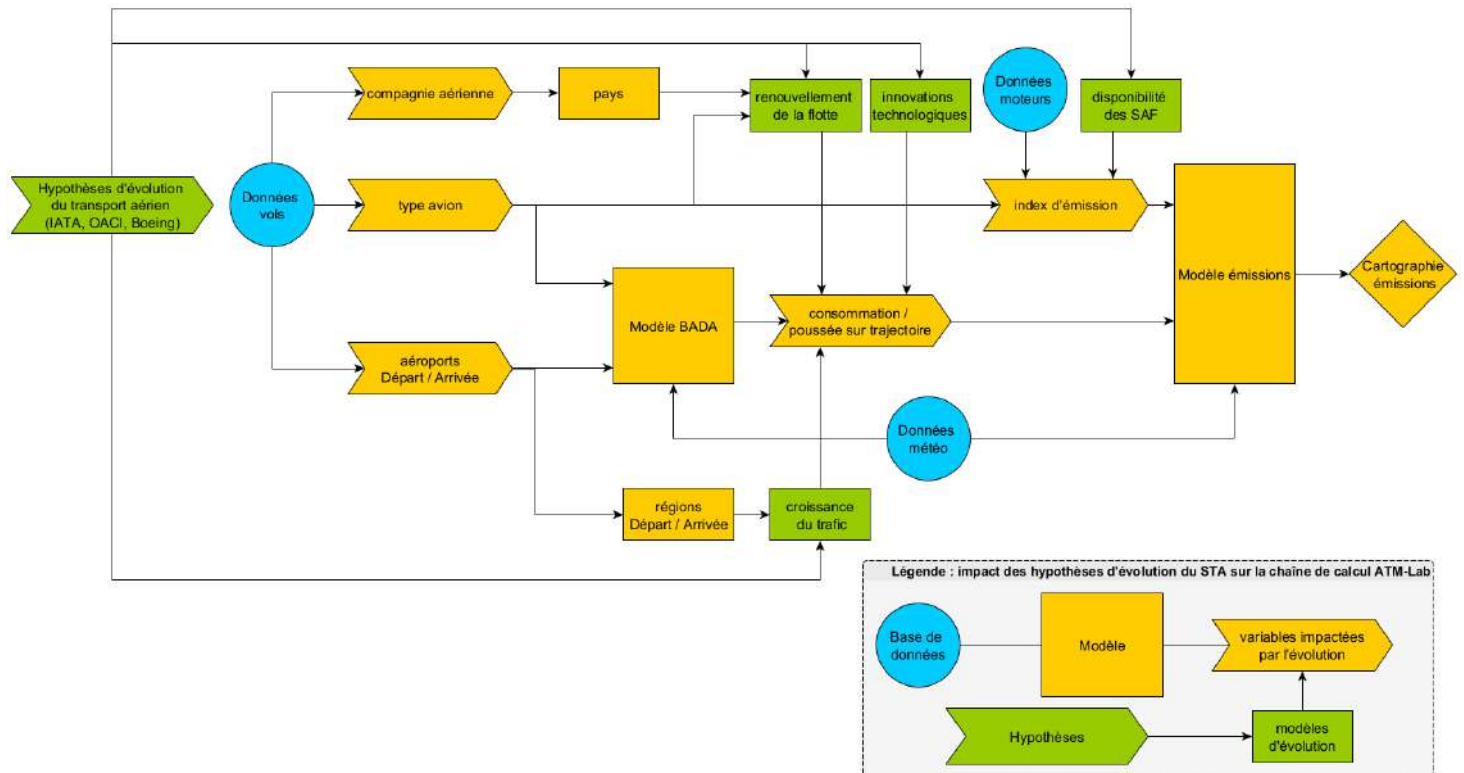


Figure 5-6: Integration of aviation evolution hypotheses into the ATM-Lab Calculation Chain

5.2. WP 5.2: Integration of all non-CO₂ effects in the climate model

The objective of work package 5.2 is to extend and improve the LMDZ global climate model by incorporating the parameterizations developed or improved by work in axes of research 1 to 3. This work has been described in those sections.

5.3. WP 5.3: Estimation of climate impacts

The objective of work package 5.3 is to estimate the CO₂ and non-CO₂ forcing from aviation and their past evolution, and to estimate the resulting climate change. This work is currently taking place in axes of research 1 to 3. An integrated view will be taken in the last year of Climaviation.

5.4. WP 5.4: Development of OSCAR-Aviation

The objective of work package 5.4 is to develop a version of the OSCAR model adapted to the climate impact of aviation.

Contributors: Audrey Lecouffe, Didier Hauglustaine, Nicolas Bellouin (IPSL)

The OSCAR model is a compact climate model whose modules mimic models of higher complexity. It was developed by Gasser et al. (2017) and simulates anthropogenic climate perturbations with reference to a pre-industrial reference state set at the year 1850. In Climaviation, the OSCAR model is modified to improve representation of the aviation sector, by considering its emissions separately from other sectors. Doing so allows the use of parameters tailored to aviation emissions, representing for example the fact that aviation emissions are made in the upper atmosphere, where residence times and the background atmosphere are different from those experienced by surface emissions. The impact of contrails, NO_x-induced tropospheric ozone, and emission of water vapour in the stratosphere are for the moment represented as time series of effective radiative forcing, with the value for 2018 set at the best estimate of Lee et al. (2021) and other years scaled accordingly to changes in fuel consumption.

In the following, emissions from the Community Emissions Data System (CEDS) inventory are used, covering the years 1750 to 2022, so including the disruptions caused by the Covid pandemic. Biomass burning emissions are from the Global Fire Emissions Database (GFED4) for 2015 to 2022. Shared Social Pathways (SSP) scenarios are used from 2030 and 2100 where emissions are provided every 10 years and then linearly interpolated annually. To bridge the period between 2022 to 2030, a new handshake is applied between historical emissions and SSP scenarios by assuming that sectoral emissions in 2024 have recovered from the pandemic disruption (if any) and returned to 2019 levels, which is true for aviation (Dannet et al., 2024).

The use of OSCAR requires two simulations: one simulation with all sector emissions ("Plane") and one simulation without aircraft emissions ("No Plane"). For tropospheric ozone, water stratospheric vapor and contrails, the effective radiative forcing is imposed from input time series in the "Plane" simulation and is set to 0 in the "No Plane" simulation. Each OSCAR simulation consists of 200 Monte Carlo elements, resulting in output ranges of concentrations, temperature or forcings with an annual time step.

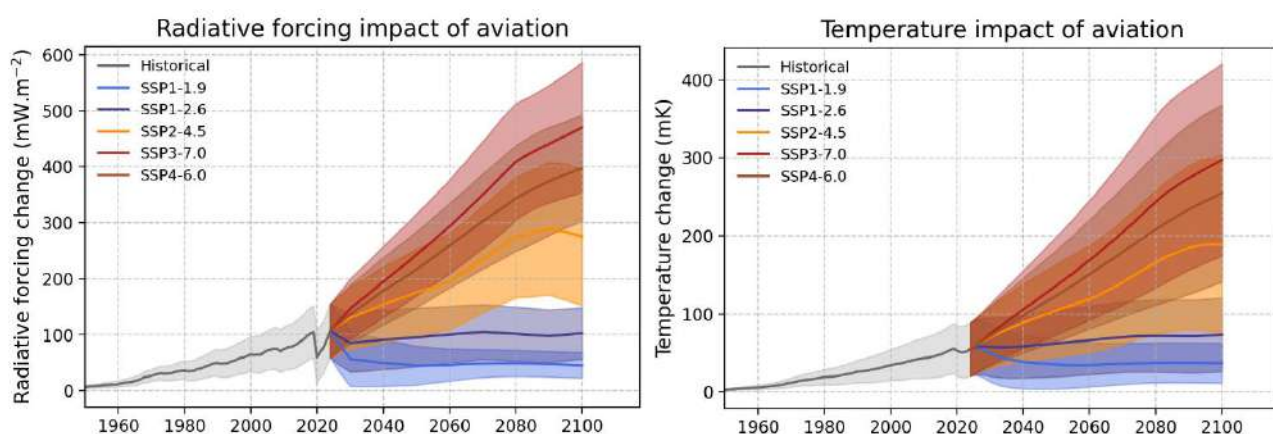


Figure 5-7: Radiative forcing ($mW m^{-2}$, left panel) and temperature (mK, right panel) contributed by aviation from 1950 to 2100 for CEDS historical and SSP scenario datasets. Uncertainty ranges represent the uncertainty in OSCAR parameters and the climate response.

Figure 5-7 shows effective radiative forcing and temperature (right) change of aviation from 1950 to 2100. With a total of 102 mW m^{-2} in 2018, it is consistent with Lee et al. (2021), who obtained 101 mW m^{-2} . However, note that large contributors are set to the best estimate of Lee et al. (2021) by construction, as mentioned above. In addition, not all OSCAR parameters have been tailored to aviation yet, so surface parameters are used instead for the moment – this impacts the simulation of the NO_x -induced methane response and aerosol-radiation interactions. Figure 5-7 suggests that in 2050, the aviation impact on temperature will be between 0.6 to 2.4 times that of today depending on scenario. For the SSP3-7.0 scenario, aviation-induced warming varies from about 0.25 to 0.40 K. That scenario gives aviation CO_2 emissions similar to those used in the ICAO LTAG mid-traffic scenario with aircraft technology frozen at 2050 levels, with about 2800 MtCO_2 in 2070. Such a large contribution to surface temperature warming is a considerable increase over the current contribution. However, note that contrail radiative forcing and NO_x -induced ozone forcing are assumed to scale with fuel consumption, but are in fact known to scale non-linearly so the current estimate is an overestimate of the temperature impact.

Our first application consisted of two contrail avoidance scenarios using OSCAR. In both scenarios, avoidance starts in 2030 and is assumed to involve only a reduction in contrail effective radiative forcing, with no increase in other contributions, including CO_2 . That is a very optimistic view of the mitigation capacity of contrail avoidance but is of interest to quantify the maximal gain that can be expected. The first scenario has a 11% reduction in contrail effective radiative forcing, which corresponds to the contribution of the North Atlantic region to global contrail forcing according to CoCiP calculations by Teoh et al. (2024) (their Table 2). The second scenario has a 50% reduction, which corresponds to the contribution of the USA, North Atlantic and Europe regions together according to Teoh et al. (2024). The base scenario for this application is the SSP3-7.0 scenario.

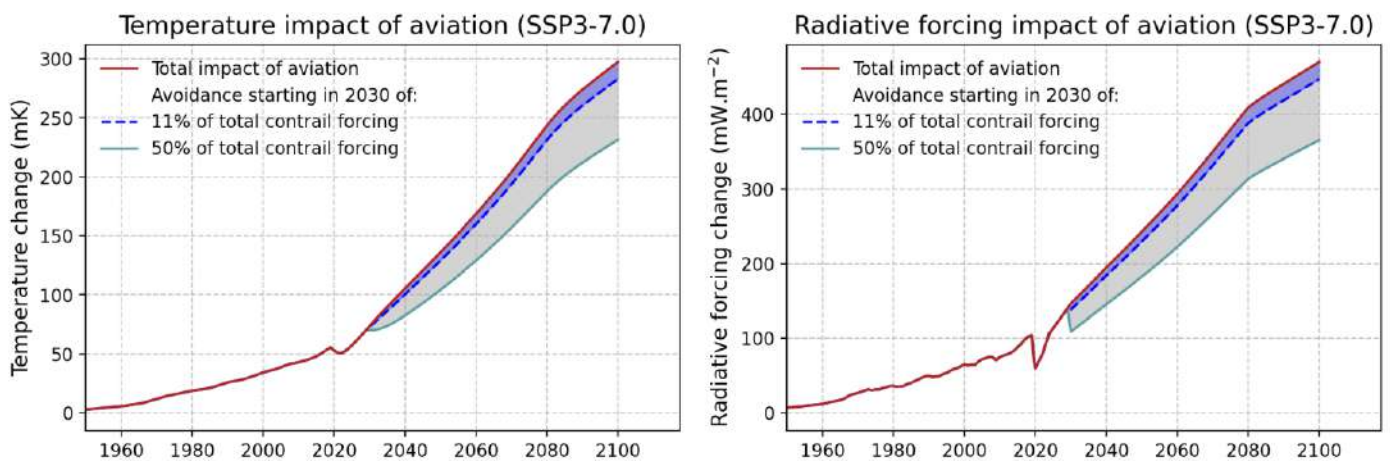


Figure 5-8: Temperature (mK, left panel) and radiative forcing (mW m^{-2} , right panel) contributed by aviation from 1950 to 2100 for the SSP3-7.0 scenario (red line) and in the case of an 11% (dark blue line) and 50% (light blue curve) reduction in contrail effective radiative forcing.

Figure 5-8 shows the results of these simplified contrail avoidance scenarios. For an 11% reduction in contrail radiative forcing, we observe a reduction of 13 mW m^{-2} in total aviation radiative forcing and 7 mK in surface temperature warming. For a 50% reduction, the values increase to 60 mW m^{-2} and 32 mK, respectively. Even the 50% reduction does not inverse the increasing contribution of aviation but slows it down by approximately 20 years in 2100 compared to the case with no avoidance.

OSCAR Aviation needs to be further improved with parameters adapted to the aviation sector. In addition, time series of external forcing need to be refined to account for non-linearities with fuel consumption. Regional response functions for aviation NO_x will eventually be integrated into OSCAR based on LMDZ(-INCA) simulations.

6. AXIS 6: OPTIMISATION STRATEGIES

The sixth axis of research has the general objective of exploring strategies for minimising the overall impact of aviation on the climate, considering not only CO₂ but also the other types of impact studied within the framework of the project.

6.1. WP 6.1: Assessment and relevance of climate change metrics for aviation

The objective of this work package is to evaluate different climate metrics and their relevance to several objectives of reducing the climate impact of aviation. Relevant work is described in WP6.4 below.

6.2. WP 6.2: Climate impact of the fleet estimated by OSCAR

The objective of work package 6.2 is to simulate the climate impact of aviation based on different scenarios of future fleet evolution. This work will take place during the last year of Climaviation.

6.3. WP 6.3: Quality and relevance of numerical weather prediction for contrail forecasting

The objective of this work package is to quantify the quality of forecasts of water vapour and regions supersaturated with respect to ice. No relevant activities have taken place over the reporting period.

6.4. WP 6.4: Study of optimisation strategies

The objective of the work package is to reflect on the different solutions that could reduce the overall climate impact of aviation, considering the specificity of the different contributors to radiative forcing and surface temperature change. The conditions for minimising the impact depend on the contributors, so compromises must be made.

6.4.1. FlightOptima: a versatile and fast cost-climate optimisation tool

Contributors: Audran Borella, Olivier Boucher (IPSL)

Contrail avoidance is attracting increasing interest to reduce the total climate impact of aviation (Frias et al., 2024, Sonabend-W et al., 2024). To address different questions linked to avoidance and climate optimisation, we developed FlightOptima, a new tool to optimise flights. This tool has been designed to answer a variety of questions; therefore, it must be versatile and fast. The core of the tool consists in the resolution of a classical 3D optimisation problem (longitude-latitude-level) using a modified Bellman-Ford algorithm. Dynamical aircraft performances are modelled, as well as aircraft emissions (CO₂, NO_x, H₂O, soot) and the formation and climate impact of contrails (CoCiP and OSCAR, aCCFs) (Engberg et al., 2025; Borella et al., 2024, Dietmüller et al., 2023). The optimised trajectory can be subject to ATC restrictions or any other restrictions, including avoidance of a contrail-forming area.

This algorithm can be used to reconstruct flightpaths from scratch, based only on the departure time and the departure and destination airports, as done in Figure 6-1. In this case, the objective function is set to minimise the actual cost of the flight. Another option is to do a cost-climate optimisation, where the total climate impact from the flight is given a cost, and thus the minimisation process includes the total climate impact from the flight. In Figure 6-2, the flight trajectory is optimised assuming that emitting 1 tCO₂eq costs 20€ (in terms of GWP100). The optimised trajectory avoids highly warming contrail forming areas, such that the total climate

impact is reduced by 12% between the cost-climate optimal route and the cost optimal route, from 219 tCO₂eq to 193 tCO₂eq in terms of GWP100. Fuel consumption is increased by 0.2%, from 48.2 tonnes to 48.3 tonnes of fuel.

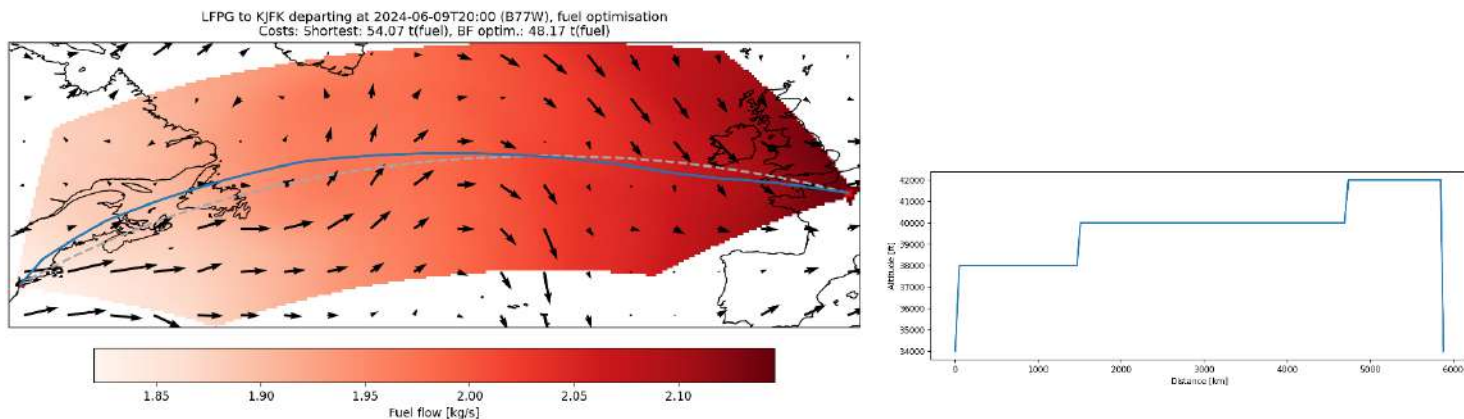


Figure 6-1: Fuel-optimised trajectory for a flight departing from Paris CDG (LFPG) at 20 UTC on 09/06/2024 to New York JFK (KJFK). The flown trajectory is shown with a blue line. The 2D trajectory is shown on the left, and the level-distance graph on the right. The wind field is represented with black arrows, and the background shows the potential fuel consumption of the aircraft [kg/s]. It diminishes as the aircraft gets lighter.

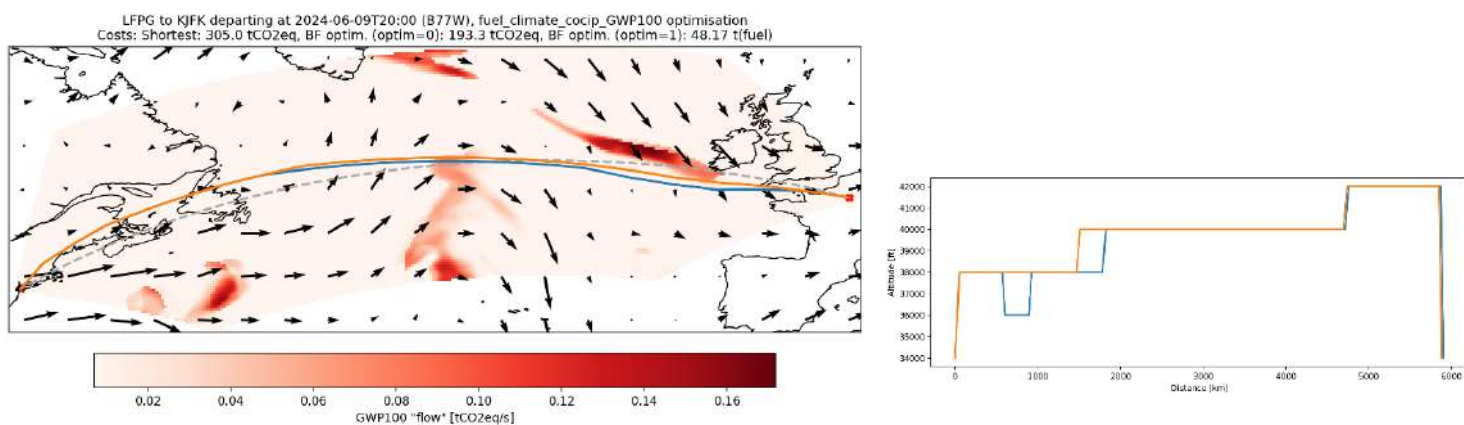


Figure 6-2: As Figure 6-1 but for a cost-climate optimisation, where emitting 1 tCO₂eq (GWP100) is assumed to cost 20€. The orange line is the cost optimal route, and the blue line is the cost-optimal route. The background shows the potential contrail climate impact [tCO₂eq/s].

Using FlightOptima, we can assess whether the cost-climate optimal route is dependent on the chosen CO₂-equivalence metric or not. Figure 6-3 shows a flight with different optimal routes, each one being optimised using a different CO₂-equivalence metric (Borella et al., 2024). There are 3 clusters of routes: (1) the fuel-optimal route that forms warming persistent contrail that are predicted to warm climate by 95 tCO₂eq (GWP100); (2) a cluster of trajectories that completely avoids the persistent contrail-forming region and fly North. This cluster is composed of routes optimised using the CO₂-equivalence metrics which put most weight on contrails: ATR100, ATR50, ATR20, GWP50, and GWP20. (3) A cluster that deviates from the fuel-optimal route to minimise contrail formation but still goes through the persistent contrail-forming region. It is composed of routes optimised using GTP100, GTP50, GTP20, and GWP100, which are the CO₂-equivalence

metrics that put more weight on CO₂ emissions. Although the cost-optimal routes differ geographically, they all imply a drastic reduction in total climate impact of contrails. Flying any one of these routes decreases the contrail climate impact from 95 tCO₂eq to at least 28 tCO₂eq (for GTP100). Moreover, the additional fuel consumption is increased by at most 1.7% (for the ATR20 route). Using this case study, we see that although the choice of CO₂-equivalence metric alters the optimal route, all cost-climate optimal routes significantly decrease the climate impact at a low additional fuel consumption.

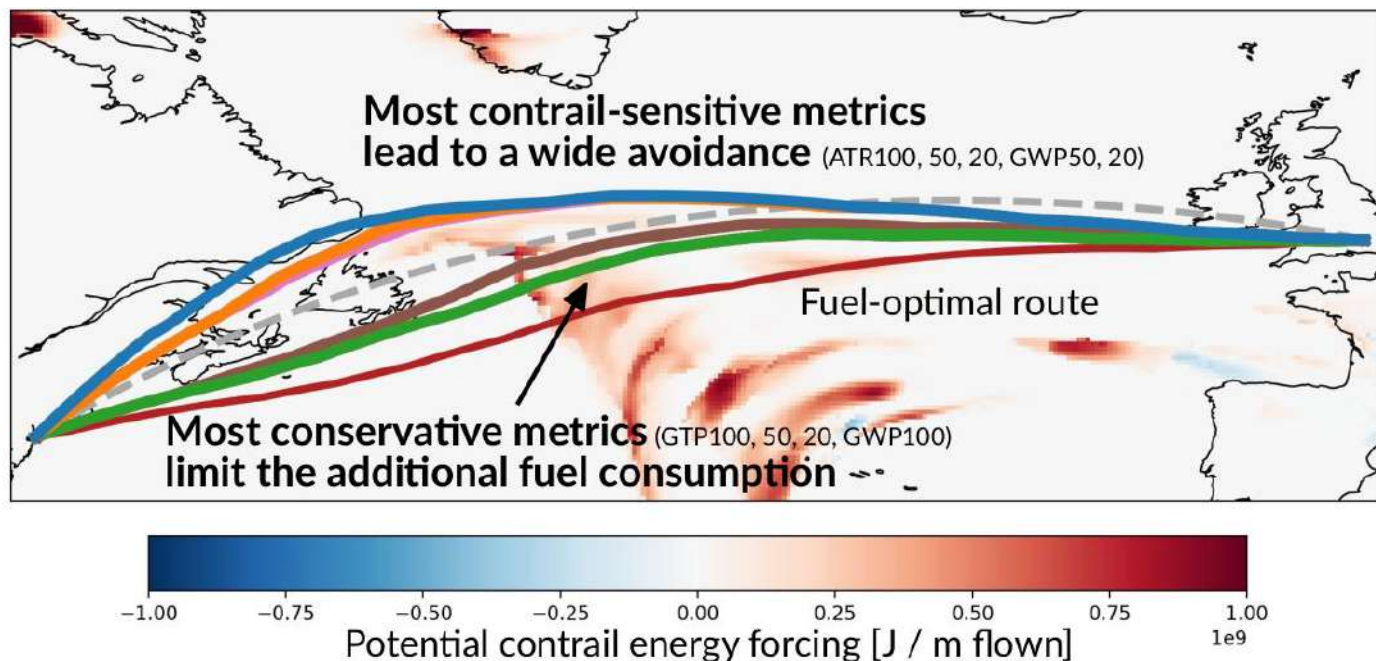


Figure 6-3: Fuel optimised and cost-climate optimised trajectories for a flight departing from New York JFK (KJFK) at 20 local time on the 20/11/2024 to London Heathrow (EGLL). The background shows the potential contrail energy forcing [in $J m^{-1}$].

The robustness of these results is yet to be assessed. High uncertainties in the prediction of the contrail climate impact arise from the uncertainties in weather forecasts and from uncertainties in the contrail prediction models (CoCiP, aCCFs, contrail efficacy, etc.) (Platt et al., 2024; Sausen et al., 2023; Hofer et al., 2024). Moreover, the optimised route may not be flown exactly as planned, because of ATC constraints, or any other modifications made en-route. All these parameters must be accounted for when optimising a flight trajectory. As a first step, we assess the uncertainties arising from weather forecasts using an ensemble prediction system. Note that the ensemble prediction system does not necessarily encompass all weather uncertainties from the weather forecast. Future work will therefore consist in assessing the consistency of cost-climate optimisation between the operational ensemble prediction system of the ECMWF and the ERA5 reanalysis. This is an important step, as operational avoidance can only be done with operational weather forecasts rather than reanalysis products.

7. REFERENCES

- Baran, A. J., Hill, P., & Francis, P. N. (2001). A consistent set of single-scattering properties for cirrus cloud radiative transfer modeling. *Journal of Quantitative Spectroscopy and Radiative Transfer*, Volumes 79-80, p549-567, [https://doi.org/10.1016/S0022-4073\(02\)00307-2](https://doi.org/10.1016/S0022-4073(02)00307-2)
- Berk, A., Conforti, P., Kennett, R., Perkins, R., Hawes, F. and van den Bosch, J., "MODTRAN® 6: A major upgrade of the MODTRAN® radiative transfer code," 2014 6th Workshop on Hyperspectral Image and Signal Processing: Evolution in Remote Sensing (WHISPERS), Lausanne, Switzerland, 2014, pp. 1-4, <https://doi.org/10.1109/WHISPERS.2014.8077573>
- Bickel M., M. Ponater, L. Bock, U. Burkhardt, S. Reineke, Estimating the Effective Radiative Forcing of Contrail Cirrus, *Journal of Climate* 33.5, pp. 1991–2005, <http://dx.doi.org/10.1175/JCLI-D-19-0467.1>, 2020.
- Borella, A., Vignon, É., Boucher, O., and Rohs, S.: An empirical parameterization of the subgrid-scale distribution of water vapor in the UTLS for atmospheric general circulation models, *Journal of Geophysical Research: Atmospheres*, 129, e2024JD040981, <https://doi.org/10.1029/2024JD040981>, 2024a.
- Borella, A., Boucher, O., Shine, K. P., Stettler, M., Tanaka, K., Teoh, R., and Bellouin, N.: The importance of an informed choice of CO₂-equivalence metrics for contrail avoidance, *Atmospheric Chemistry and Physics*, 24, 9401–9417, <https://doi.org/10.5194/acp-24-9401-2024>, 2024b.
- Borella, A., Vignon, É., Boucher, O., Meurdesoif, Y., and Fairhead, L.: A New Prognostic Parameterization of Subgrid Ice Supersaturation and Cirrus Clouds in the ICOLMDZ AGCM, *JAMES*, <https://doi.org/10.22541/essoar.173542221.18676203/v1>; 2024, submitted.
- Boucher, O., Borella, A., Gasser, T., and Hauglustaine, D.: On the contribution of global aviation to the CO₂ radiative forcing of climate, *Atmos. Environ.*, 267, 118761, <https://doi.org/10.1016/j.atmosenv.2021.118762>, 2021.
- Brasseur, G. P., Gupta, M., et al. (2016). Impact of aviation on climate: Research priorities. *Bulletin of the American Meteorological Society*, 97(4), 561–583. <https://doi.org/10.1175/2009BAMS2850.1>
- Cariolle, D., Caro, D., Paoli, R., Hauglustaine, D.A., Cuénot, B., Cozic, A., Paugam, R., 2009. Parameterization of plume chemistry into large-scale atmospheric models: Application to aircraft NO_x emissions. *J. Geophys. Res.* 114, D19302. <https://doi.org/10.1029/2009JD011873>.
- Charlesworth, E., Plöger, F., Birner, T., Baikhadzhaev, R., Abalos, M., Abraham, N. L., Akiyoshi, H., Bekki, S., Dennison, F., Jöckel, P., Keeble, J., Kinnison, D., Morgenstern, O., Plummer, D., Rozanov, E., Strode, S., Zeng, G., Egorova, T., and Riese, M.: Stratospheric water vapor affecting atmospheric circulation, *Nat Commun*, 14, 3925, <https://doi.org/10.1038/s41467-023-39559-2>, 2023.
- CORAC - Décarbonation du Transport Aérien, Analyses et propositions du CORAC, Septembre 2021. <https://aerorecherchecorac.com/wp-content/uploads/2022/01/decarbonation-corac-rapport-complet-decembre2021.pdf>
- Dannet, G., Boucher, O., Bellouin, N. Features and evolution of civil aviation CO₂ emissions based on ADS-B data for the period between 2019–2024[J]. *Metascience in Aerospace*, 1(4): 346-370. <https://doi.org/10.3934/mina.2024016>, 2024

- Dietmüller, S., Matthes, S., Dahlmann, K., Yamashita, H., Simorgh, A., Soler, M., Linke, F., Lührs, B., Meuser, M. M., Weder, C., Grewe, V., Yin, F., and Castino, F.: A Python library for computing individual and merged non-CO₂ algorithmic climate change functions: CLIMaCCF V1.0, *Geoscientific Model Development*, 16, 4405–4425, <https://doi.org/10.5194/gmd-16-4405-2023>, 2023.
- Engberg, Z., Teoh, R., Abbott, T., Dean, T., Stettler, M. E. J., and Shapiro, M. L.: Forecasting contrail climate forcing for flight planning and air traffic management applications: the CocipGrid model in pycontrails 0.51.0, *Geoscientific Model Development*, 18, 253–286, <https://doi.org/10.5194/gmd-18-253-2025>, 2025.
- Fabre, D., Jacquin, L., & Loof, A. (2002). Optimal perturbations in a four-vortex aircraft wake in counter-rotating configuration. *Journal of Fluid Mechanics*, 451, 319-328. <https://doi.org/10.1017/S0022112001006954>
- Frias, A. M., Shapiro, M. L., Engberg, Z., Zopp, R., Soler, M., and Stettler, M. E. J.: Feasibility of contrail avoidance in a commercial flight planning system: an operational analysis, *Environ. Res.: Infrastruct. Sustain.*, 4, 015013, <https://doi.org/10.1088/2634-4505/ad310c>, 2024.
- Gasser, T., Ciais, P., Boucher, O., Quilcaille, Y., Tortora, M., Bopp, L., and Hauglustaine, D.: The compact Earth system model OSCAR v2.2: description and first results, *Geosci. Model Dev.*, 10, 271–319, <https://doi.org/10.5194/gmd-10-271-2017>, 2017.
- Ghedhaifi W., Bienner A., Megherbi R., Montreuil E., Terrenoire E., Vancassel X., Loseille A., Influence of atmospheric conditions on contrail formation: 3D simulation versus Schmidt- Appleman criterion. ISABE 2019 - 24th ISABE Conference, Sep 2019, Canberra, Australia. <https://hal.science/hal-02470854v1>, 2019.
- Hauglustaine, D. A., Hourdin, F., Jourdain, L., Filiberti, M. A., Walters, S., Lamarque, J. F., and Holland, E. A.: Interactive chemistry in the Laboratoire de Meteorologie Dynamique general circulation model: Description and background tropospheric chemistry evaluation, *J. Geophys. Res.*, 109, D04314, <https://doi.org/10.1029/2003JD003957>, 2004.
- Hofer, S., Gierens, K., and Rohs, S.: How well can persistent contrails be predicted? An update, *Atmospheric Chemistry and Physics*, 24, 7911–7925, <https://doi.org/10.5194/acp-24-7911-2024>, 2024.
- Hogan, R. J., Hirahara, S., & Mayer, B. (2017). A new radiation scheme for the IFS. *ECMWF Technical Memorandum No. 816*.
- Hogan, R. J., & Bozzo, A. (2018). A flexible and efficient radiation scheme for the ECMWF model. *Journal of Advances in Modeling Earth Systems*, 10(8), 1990–2008. <https://doi.org/10.1029/2018MS001364>
- Holmes, C. D., Prather, M. J., Søvde, O. A., and Myhre, G.: Future methane, hydroxyl, and their uncertainties: key climate and emission parameters for future predictions, *Atmos. Chem. Phys.*, 13, 285–302, <https://doi.org/10.5194/acp-13-285-2013>, 2013.
- IATA - A World with Lower Oil Prices? Technical Report December 2024. <https://www.iata.org/en/iata-repository/publications/economic-reports/global-outlook-for-air-transport-december-2024/>
- ICAO - Long-Term Aspirational Goal (LTAG) Report on Reducing International Civil Aviation CO₂ Emissions, Committee on Aviation Environmental Protection (CAEP), March 2022. <https://www.icao.int/environmental->

[protection/LTAG/Documents/REPORT%20ON%20THE%20FEASIBILITY%20OF%20A%20LONG-TERM%20ASPIRATIONAL%20GOAL_en.pdf](https://doi.org/10.1016/j.atmosenv.2020.117834)

- Jouliia, A., Bedouet, J., Sarrat, C., Parzani, C., and T., D.: First steps towards aviation climate impact assessment using ATMLab, Towards Sustainable Aviation Submit, Toulouse, France, 2025. <https://doi.org/10.60711/TSAS25.20250224.7828349968154456>
- Kärcher, B., Mahrt, F. & Marcolli, C. Process-oriented analysis of aircraft soot-cirrus interactions constrains the climate impact of aviation. *Commun Earth Environ* 2, 113 (2021). <https://doi.org/10.1038/s43247-021-00175-x>
- Khou, J. C., Ghedhaifi, W., Vancassel, X., & Garnier, F. (2015). Spatial simulation of contrail formation in near-field of commercial aircraft. *Journal of Aircraft*, 52(6), 1927-1938. <https://doi.org/10.2514/1.C033101>
- Labarre, L., Croizé, L., Fauqueux, S., Huet, T., Malherbe, C., and Pierro, J., Matisse-v3.0 : overview and future developments. In 11th International IR Target & Background, Modelling Workshop, 2016.
- Lee D.S, D.W. Fahey, A. Skowron, M.R. Allen, U. Burkhardt, Q. Chen, S.J. Doherty, S. Freeman, P.M. Forster, J. Fuglestedt, A. Gettelman, R.R. De León, L.L. Lim, M.T. Lund, R.J. Millar, B. Owen, J.E. Penner, G. Pitari, M.J. Prather, R. Sausen, L.J. Wilcox, The contribution of global aviation to anthropogenic climate forcing for 2000 to 2018, *Atmospheric Environment*, 244, 117834, <https://doi.org/10.1016/j.atmosenv.2020.117834>, 2021
- McFarquhar, G. M., & Heymsfield, A. J. (1998). The definition and significance of an effective radius for ice clouds. *Journal of the Atmospheric Sciences*, 55(2), 203–216. [https://doi.org/10.1175/1520-0469\(1998\)055%3C2039:TDASOA%3E2.0.CO;2](https://doi.org/10.1175/1520-0469(1998)055%3C2039:TDASOA%3E2.0.CO;2)
- Myhre, G., Kvalevåg, M., Rädel, G., Cook, J., Shine, K. P., Clark, H., Karcher, F., Markowicz, K., Kardas, A., Wolkenberg, P., Balkanski, Y., Ponater, M., Forster, P., Rap, A., Leon, R., and Rodriguez. Intercomparison of radiative forcing calculations of stratospheric water vapour and contrails. *Meteorologische Zeitschrift*, 18(6) :585–596, December 2009. ISSN 0941-2948. doi : 10.1127/0941-2948/2009/0411. <https://doi.org/10.1127/0941-2948/2009/0411>
- Petry. H , J. Hendricks , M. Möllhoff , E. Lippert , A. Meier , A. Ebel and R. Sausen , Chemical conversion of subsonic aircraft emissions in the dispersing plume: Calculation of effective emission indices, *J. Geophys. Res.: Atmos.*, 1998, <https://doi.org/10.1029/97JD03749>, 103, 5759 —577.
- Platt, J. C., Shapiro, M. L., Engberg, Z., McCloskey, K., Geraedts, S., Sankar, T., Stettler, M. E. J., Teoh, R., Schumann, U., Rohs, S., Brand, E., and Arsdale, C. V.: The effect of uncertainty in humidity and model parameters on the prediction of contrail energy forcing, *Environ. Res. Commun.*, 6, 095015, <https://doi.org/10.1088/2515-7620/ad6ee5>, 2024.
- Pycontrails: <https://github.com/contrailcirrus/pycontrails>. Last access 31/03/2025.
- Saulgeot, P., Brion, V., Bonne, N., Dormy, E., & Jacquin, L. (2023). Effects of atmospheric stratification and jet position on the properties of early aircraft contrails. *Physical Review Fluids*, 8(11), 114702. <https://doi.org/10.1103/PhysRevFluids.8.114702>
- Sausen, R., Hofer, S. M., Gierens, K. M., Bugliaro Goggia, L., Ehrmanntraut, R., Sitova, I., Walczak, K., Burridge-Diesing, A., Bowman, M., and Miller, N.: Can we successfully avoid persistent contrails by

- small altitude adjustments of flights in the real world?, *Meteorologische Zeitschrift*, 2023. <https://doi.org/10.1127/metz/2023/1157>
- Sanogo, S., Boucher, O., Borella, A., Hourdin, F., Bellouin, N., Vignon, É., Musat, I., Coulon-Decorzens, M., Sima, A., Cheruy, F.: Tunability of ice supersaturation in the upper troposphere and lower stratosphere in the LMDZ atmospheric model, *JAMES*, 2025, submitted.
- Schumann, U., Graf, K., & Mayer, B. (2012). Radiative forcing by contrail cirrus. *Atmospheric Chemistry and Physics*, 12(3), 11969–11984. <https://doi.org/10.5194/acp-12-11969-2012>
- Schumann, U., Baumann, R., Baumgardner, D., Bedka, S. T., Duda, D. P., Freudenthaler, V., Gayet, J.-F., Heymsfield, A. J., Minnis, P., Quante, M., Raschke, E., Schlager, H., Vázquez-Navarro, M., Voigt, C., and Wang, Z., Properties of individual contrails : a compilation of observations and some comparisons. *Atmospheric Chemistry and Physics*, 17(1) :403–438, January 2017. ISSN 1680-7324. <https://doi.org/10.5194/acp-17-403-2017>, 2017.
- Spichtinger, P., Gierens, K., & Wernli, H. (2005). A case study on the formation and evolution of ice supersaturation in the vicinity of a warm conveyor belt's outflow region. *Atmospheric Chemistry and Physics*, 5(4), 973–987. <https://doi.org/10.5194/acp-5-973-2005>
- Teoh, R., Engberg, Z., Shapiro, M., Dray, L., and Stettler, M. E. J.: The high-resolution global aviation emissions inventory based on ADS-B (GAIA) for 2019–2021, *Atmospheric Chemistry and Physics*, 24, 725–744, <https://doi.org/10.5194/acp-24-725-2024>, 2024.
- Terrenoire, E., Hauglustaine, D. A., Gasser T., and Penanhoat, O.: The contribution of carbon dioxide emissions from the aviation sector to future climate change, *Environ. Res. Lett.*, 14, 084019, <https://doi.org/10.1088/1748-9326/ab3086>, 2019.
- Vassberg, J., Dehaan M. A., Rivers M., Wahls R. A., Development of a Common Research Model for Applied CFD Validation Studies, 26th AIAA Applied Aerodynamics Conference, <https://doi.org/10.2514/6.2008-6919>, 2008.
- Vidot, J., Roger, J. C., & Lavanant, L. (2015). Improvement of cloud retrievals from MSG/SEVIRI using OCA in SAFNWC context. *Atmospheric Chemistry and Physics*, 15(9), 4495–4508. <https://doi.org/10.5194/acp-15-4495-2015>
- Wang, X., Wolf, K., Boucher, O., & Bellouin, N. (2024). Radiative effect of two contrail cirrus outbreaks over Western Europe estimated using geostationary satellite observations and radiative transfer calculations. *Geophysical Research Letters*, 51(7), e2024GL108452. <https://doi.org/10.1029/2024GL108452>
- Watts, P. D., Bennartz, R., Fell, F., & Bührke, F. (2011). Optimal retrieval of cloud microphysical properties from MSG SEVIRI. *Atmospheric Chemistry and Physics*, 11(11), 5331–5345. DOI: 10.5194/acp-11-5331-2011
- Wolf, K., Bellouin, N., and Boucher, O.: Long-term upper-troposphere climatology of potential contrail occurrence over the Paris area derived from radiosonde observations, *Atmos. Chem. Phys.*, 23, 287–309, <https://doi.org/10.5194/acp-23-287-2023>, 2023.
- Wolf, K., Bellouin, N., and Boucher, O., Sensitivity of cirrus and contrail radiative effect on cloud microphysical and environmental parameters. *Atmospheric Chemistry and Physics*, 23(21) : 14003–14037, November 2023. ISSN 1680-7324. <https://doi.org/10.5194/acp-23-14003-2023>, 2023.

Yang, H., S. Dobbie, G. G. Mace, A. Ross, and M. Quante, 2012: GEWEX Cloud System Study (GCSS) cirrus cloud working group: Development of an observation-based case study for model evaluation. *Geosci. Model Dev.*, 5, 829–843, <https://doi.org/10.5194/gmd-5-829-2012>.